Open Access Dissertations

Fall 2014

Microwave chemical sensing using overmoded T-line designs and impact of real-time digitizer in the system

Yu-Ting Huang
Purdue University

Follow this and additional works at: https://docs.lib.purdue.edu/open_access_dissertations

Part of the Electromagnetics and Photonics Commons

PURDUE UNIVERSITY
GRADUATE SCHOOL
Thesis/Dissertation Acceptance

This is to certify that the thesis/dissertation prepared

By Yu-Ting Huang

Entitled
Microwave Chemical Sensing Using Overmoded T-line Designs and Impact of Real-time Digitizer in the System

For the degree of   Doctor of Philosophy

Is approved by the final examining committee:

WILLIAM J. CHAPPELL

DAVID B. JANES

STEVEN T. SHIPMAN

ZHENG OUYANG

To the best of my knowledge and as understood by the student in the Thesis/Dissertation Agreement, Publication Delay, and Certification/Disclaimer (Graduate School Form 32), this thesis/dissertation adheres to the provisions of Purdue University's "Policy on Integrity in Research" and the use of copyrighted material.

WILLIAM J. CHAPPELL

Approved by Major Professor(s): _____

Approved by: Michael R. Melloch   10/01/2014

Head of the Department Graduate Program   Date

MICROWAVE CHEMICAL SENSING USING OVERMODED T-LINE DESIGNS

AND IMPACT OF REAL-TIME DIGITIZER IN THE SYSTEM

A Dissertation

Submitted to the Faculty

of

Purdue University

by

Yu-Ting Huang

In Partial Fulfillment of the

Requirements for the Degree

of

Doctor of Philosophy

May 2015

Purdue University

West Lafayette, Indiana

To Pei-Yun, Alexander, and Mijen

ACKNOWLEDGMENTS

TABLE OF CONTENTS

LIST OF TABLES

LIST OF FIGURES

Figure   Page

ABBREVIATIONS

ABSF   absorptive bandstop filter

AWG   arbitrary waveform generator

CP   chirped pulse

FID   free induction decay

FTMW   Fourier transform microwave

LEVC   large electrical volume coaxial cable

OMC   overmoded coaxial cable

PDRO   phase-locked dielectric resonator oscillator

Q   quality factor

Q_u unloaded quality factor

RT   room temperature

SNR   signal-to-noise ratio

STAR   simultaneous transmit and receive

TWT   traveling wave tube

ABSTRACT

Huang, Yu-Ting Ph.D., Purdue University, May 2015. Microwave Chemical Sensing Using Overmoded T-line Designs and Impact of Real-time Digitizer in the System. Major Professor: William J. Chappell.

Microwave spectrometers have unique advantages in the ability to determine high resolution features that are specific to a given chemical. Very sharp lines which correspond to quantum states of the chemical allow for unique identification of the chemical. Recent advances have shown the possibility of room temperature microwave spectroscopy analysis in which the data is collected in a short amount of time using broadband chirp pulse Fourier transform microwave (CP-FTMW) spectroscopy. In this study, we explore the design of reduced size spectrometers focusing on the reduction as well as expansion of operation frequency of the microwave analysis cell, where the chemical is analyzed at room temperature. Through optimization of the features of the test cell, it is shown that a much smaller analysis cell can be utilized. In combination with the established trends of real-time digitizer, we demonstrated successful chemical detection with relatively low excitation power. A simultaneous transmit and receive mechanism is subsequently demonstrated and shows the potential for a future compact microwave chemical sensing device with an increased detection speed and low power consumption.

1. INTRODUCTION

Microwave spectroscopy is the study of the rotational transition spectra of gas-phase molecules [1]– [3]. Because of the advantage of high spectral resolution in determining rotational transitions, scientists found the application of microwave spectroscopy beneficial in studying and identifying compounds in interstellar medium [4]– [8]. Since then, microwave spectroscopy has been one of the most useful and efficient tools in chemical identification because it is highly sensitive to molecular structure [9]. This technique can distinguish isomers, which are chemicals that share the same molecular formula but have different arrangements of atoms. In particular, microwave spectroscopy can readily differentiate geometric isomers (or cis-trans isomers) that have dissimilar arrangements of functional groups about a double bond. Detection of geometric isomers are quite challenging in this regard because they cannot be differentiated using techniques such as mass spectrometry (MS) and will take up to several minutes using gas chromatograpy-mass spectrometry (GC-MS) [10], [11]. Since modifications in molecular geometry can give rise to varying physical and chemical properties, the shape sensitivity of microwave spectroscopy is a significant benefit for chemical sensing because it enhances detection specificity and reduces false detection rate [11].

1.1 Historical Review

The field of microwave spectroscopy originated during World War II as a useful tool in determining molecule structures for physical chemists. Afterward, Dicke *et al.* proposed the free induction decay (FID) time-domain measurement, which is also known as Fourier transform microwave (FTMW) spectroscopy [12]. In the 1980s, Belle and Flygare incorporated a Fabry-Perot resonator and a pulsed molecular beam in

their FTMW spectrometer [13]– [17], and some modifications to the cavity resonator design were also introduced [18]. In 2008, a major advance in broadband measurement was introduced with a chirped pulse Fourier transform microwave (CP-FTMW) spectrometer [20]. Most of the FTMW work incorporated a pulsed molecular beam in the system and utilized supersonic expansion to cool the molecules down to the ~1 K range; such a cooling effect will trap the molecules in lower rotational states since molecule population follows a Boltzmann distribution [18], [19]. Recently, Shipman designed a room temperature chirped pulse Fourier transform microwave (RT-CP-FTMW) spectrometer using a WRD750 double ridge waveguide [21], [22]

1.2   Microwave Spectroscopy Fundamentals

In the field of microwave spectroscopy, the key parameter of rotational spectra is the moment of inertia, I, which is defined as the mass of each atom multiplied by the square of its perpendicular distance to the rotational axis through the center of mass of the molecule; i.e. $I = \Sigma m_i r_i^2$, where m_i is the mass of each atom and r_i is the perpendicular distance to the axis of rotation, and a physical picture is show in Fig. 1.1 as an example [23]. In general, the rotational states can be described in terms of moment of inertia about three perpendicular axes. Transitions between these rotational states can be caused by the application of external electromagnetic radiation. These fields interact with the molecule's permanent dipole moment caused by the charge separation within the molecule.

When the molecule is exposed to an external electromagnetic field, the electric field will impart a torque to the molecule and induce the rotational state transitions. A semi-classical picture of the interaction between external fiend and molecule is shown in Fig 1.2. The rotational states and their transitions can be predicted by quantum physics, and therefore microwave spectroscopy has been a useful tool in determining molecular structure.
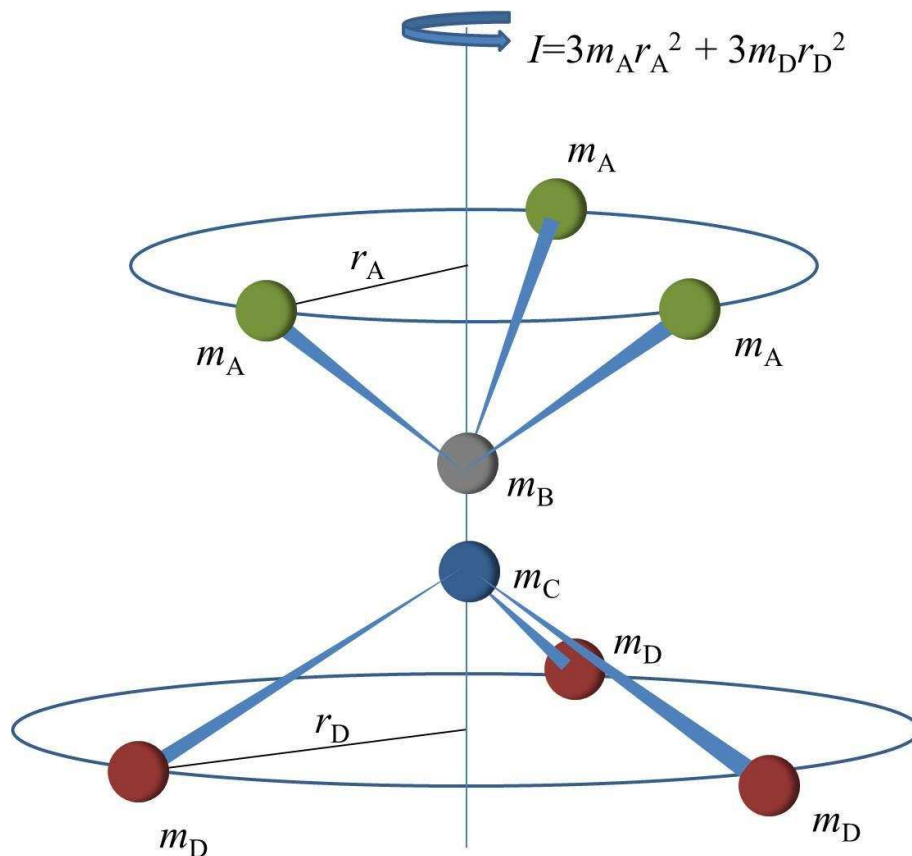
Fig. 1.1. Definition of moment of inertia, I, of a molecule. In this example, the center of mass lies on the axis passing through atoms B and C, and r_A and r_D are the perpendicular distances from atoms A and D to the axis of rotation.

A simple absorptive-type microwave spectrometer requires (1) a frequency source, (2) a probe channel (waveguide or resonator), and (3) a detector. Early spectrometers utilized the direct induced absorption mechanism to acquire the spectra. A continuous-wave (CW) microwave source is passed through a probe channel, and the output power is related to the channel length L, channel and gas absorption coefficients α_c and α_{gas}, and input power P_i, i.e. $P_o = P_i e^{-(\alpha_c + \alpha_{gas})L}$ [2], [24], [25]. The sample in the probe channel will have strong absorption coefficients at frequencies that correspond to its rotational transition frequencies, and hence the output signal will exhibit transmission dips at the corresponding frequencies. Therefore, a long
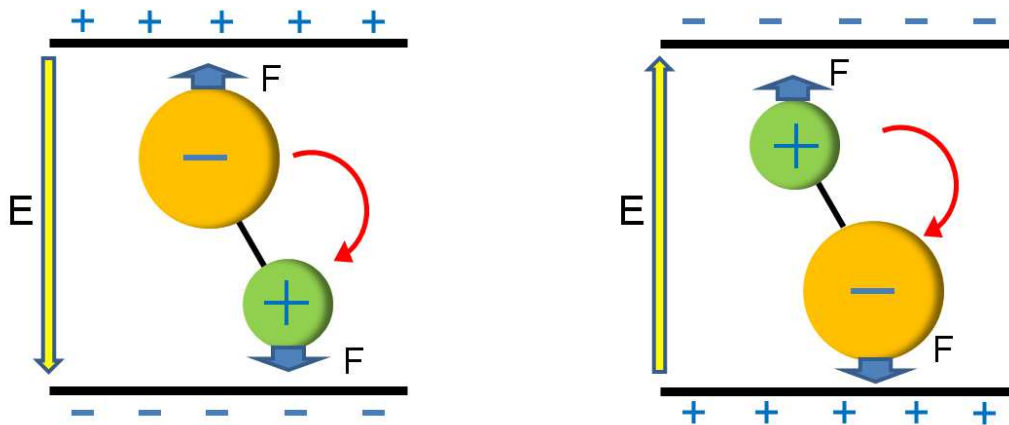
Fig. 1.2. A parallel plate capacitor is used to simulate the external field. When the alternating frequency of the external electric field equals to the rotation frequency, the molecule will absorb energy from the external field.

waveguide (usually several meters long) or a high-Q resonator (which has an effective length of $L_{eff} = \frac{Q\lambda}{2\pi}$) is required for direct absorption detection, and waveguide spectrometers utilizing Stark effect were also introduced to improve their sensitivity [26]– [28]. Physically, a waveguide spectrometer that is several meters long is not favorable as a chemical sensor. Moreover, although a high-Q resonator significantly reduces the size of a spectrometer, performing a wideband measurement with such a resonator is extremely time-consuming because one would require a stepper motor to fine-tune the cavity resonance frequency to sweep through the desired bandwidth.

FID is the other detection scheme that is widely used in microwave spectroscopy. While direct absorption detection exploits the frequency-dependent energy differences observed by probing a sample with a microwave energy sweep and is suitable for samples having higher dipole moments, FID detection measures the weak high-Q re-emission, Fig. 1.3 of molecular signals after the samples are excited by a microwave energy sweep. Therefore, for samples with weaker absorption coefficients, FID detection works better due to its higher dynamic range because it detects signals in the absence of the excitation energy sweep [12].
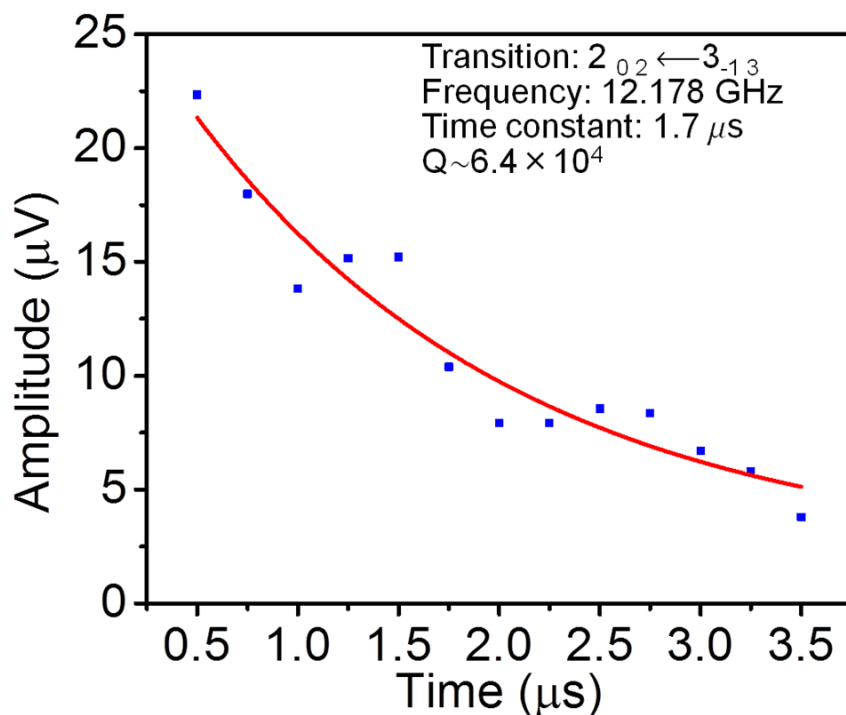
Fig. 1.3. The $2_{0\ 2} \leftarrow 3_{-1\ 3}$ transition as an example of a molecule's high-Q ring down. With a time constant of 1.7 μs and frequency of 12.178 GHz, Q is 64,000.

In FID detection, we detect the time-domain re-emission of the gaseous samples and then apply a Fourier transform to obtain the frequency-domain rotational spectrum. Two limiting factors to the spectral quality are the number of molecules and collisional broadening effects. The latter is the dominant factor in FTMW because when molecules suffer from collisions, they lose not only their re-emission energy but also their phase coherence. The ring-down time of molecules decreases significantly after collision; along with the loss in phase coherence, the spectral line intensity and resolution are reduced. Both collisions among molecules and collisions between molecules and the sidewalls of the waveguide contribute to collisional broadening.

1.3   Room-temperature Spectroscopy

It has been a trend for physical chemists to include a cooling mechanism for low-temperature spectroscopy. Strong spectral lines are measured in the low-temperature regime, and lower number of lines (number of transitions) are observed because molecule population follows a Boltzmann distribution and molecules populated near low rotational states. On the contrary, room-temperature spectrum is usually more complex because of the increased variety of transitions. This will add benefits to the application of using microwave spectroscopy as chemical sensor because spectral lines provides fingerprint information of a chemical under detection. A comparison of low-temperature and room-temperature is shown in Fig. 1.4.
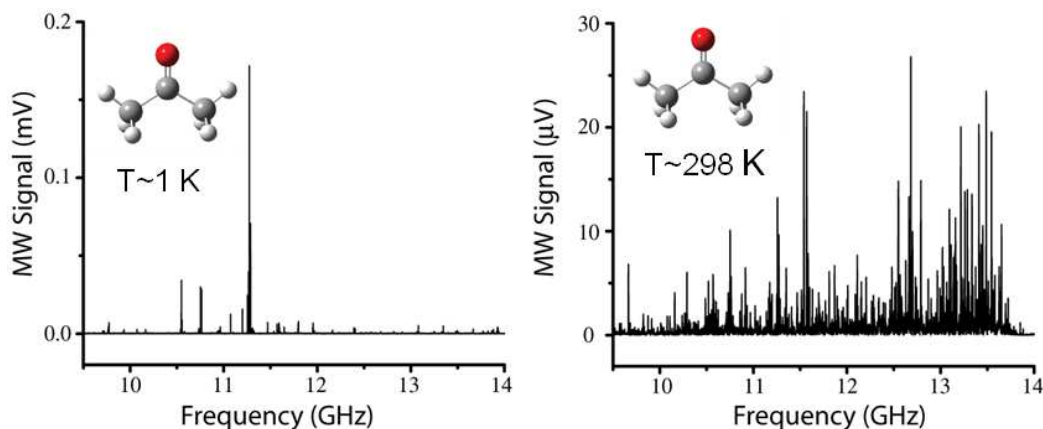
Fig. 1.4. Comparison of acetone spectrum at low-temperature $\sim$1 K and room-temperature spectrum (courtesy of Prof. Shipman). As shown in the figure, acetone has a more complex spectrum at room-temperature than at low-temperature.

1.4   High-frequency Spectroscopy

In addition to the complexity in spectrum at room-temperature, spectral line intensities are stronger in the high frequency region, as shown in Fig. 1.5. Therefore, at room-temperature it is preferable to operate a spectrometer/sensor in the

high frequency region where the waveguide/transmission line dimensions are reduced. However, the first challenge a microwave engineer will encounter is a more serious collisional broadening in FID detection that results from the reduction of the physical dimensions of a waveguide/transmission line. Solutions to mitigate the collisional broadening effect are given in Chapter 3.
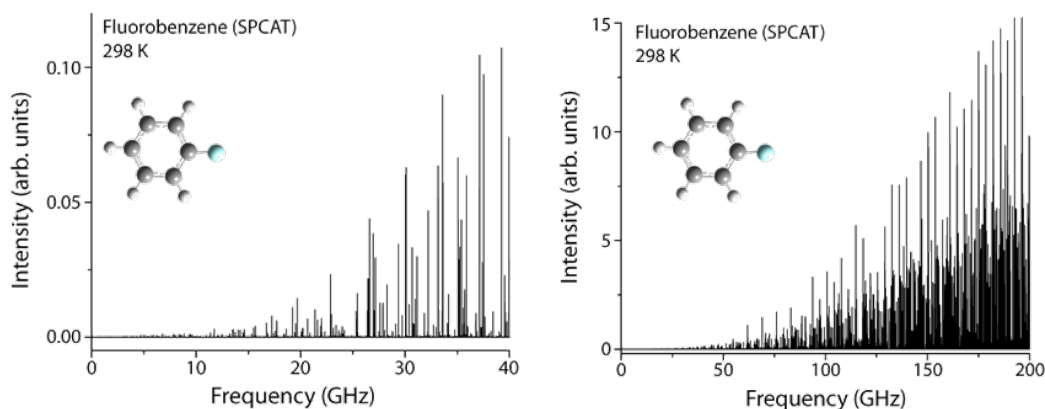
Fig. 1.5. As shown in the figure, fluorobezene has stronger spectral lines at high frequencies (courtesy of Prof. Shipman).

1.5   Future Trends of Microwave Spectrometers

With a review of the history and the fundamentals of microwave spectroscopy, we believe it is feasible to develop a compact microwave spectrometer operating at room-temperature and in a high frequency regime with high sensitivity. We also foresee that at high frequencies the available power to excite chemical species will be limited. Therefore, it is preferable to utilize a closed analysis cell such that the excitation energy from the power source and the re-emission signal from the molecules are guided without radiation loss. In addition, with low excitation power, instead of probing many rotational resonances across a wide bandwidth, the available power should be focused on certain strong resonances of a target chemical. Using such a chemical sensing strategy, we can reduce the total detection time of multiple resonances by simultaneously excite and receive resonances at multiple different frequencies.

In this work we propose compact analysis cell designs that demonstrate practical solutions to overmode a waveguide/transmission line to reduce the wall collision effect. We also propose overmoded coaxial cable (OMC) and large electrical volume coaxial cable (LEVC) transmission line designs to expand the operation bandwidth towards lower frequencies, which can be useful in detection of heavy or biological molecules [29]– [34]. The proposed designs lead to practical means for changing the physical dimensions of a transmission line while maintaining good impedance matching. Impact by the wall collisions between the molecules and walls of the analysis cells are also reduced. These design techniques can be useful for future high-frequency spectrometer design where the physical dimensions of an analysis cell will reduce significantly causing severer wall collision effect.

We also demonstrated spectral line acquisition using low excitation power, which is critical for chemical detection using a compact spectrometer with limited power. Molecular signal decay in the LEVC and OMC spectrometers are also characterized. Results found in this decay characterization are applied in the prediction of signal strength of different start detection time and excitation power. Details of these discussions will be shown in Chapter 3 and Chapter 4. In Chapter 4, by using low input power, we eventually achieved detection with zero delay after the excitation pulse ends. Finally, simultaneous transmit and receive is demonstrated by cascading an absorptive bandstop filter before the LNA and is demonstrated in Chapter 5.

2. ROOM-TEMPERATURE CHIRPED PULSE FOURIER TRANSFORM MICROWAVE SPECTROSCOPY

A room-temperature chirped pulse FTMW (RT-CP-FTMW) spectrometer consists of three major components: (a) excitation pulse generation, (b) a microwave/probe channel, and (c) free induction decay (FID) detection [20]. The schematic of the system is shown in Fig. 2.1, and each part will be discussed in detail.
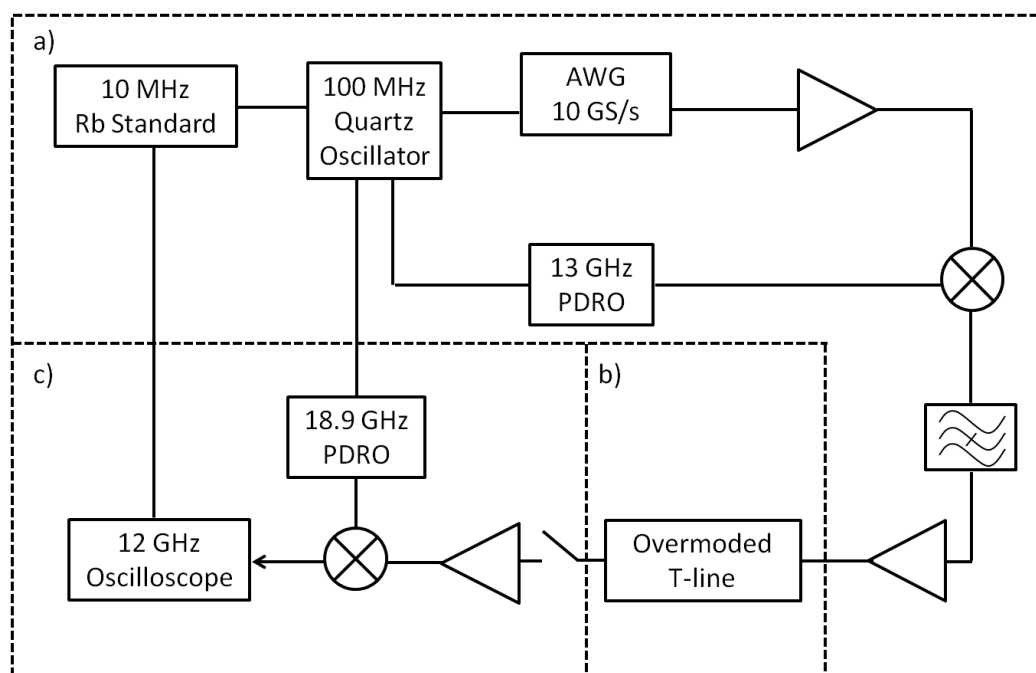
Fig. 2.1. Schematics for experimental setup. The spectrometer consists of a) excitation pulse generation, b) probe channel, and c) FID detection.

2.1   Excitation Pulse Generation

To achieve a broadband measurement, a chirped excitation pulse is used to probe multiple rotational transitions of a chemical in a single microwave energy sweep. The microwave circuit used for chirped pulse generation is shown in Fig. 2.2. An excitation pulse of the desired bandwidth is generated by an arbitrary waveform generator (Tektronix AWG 7101) at 10 GS/s sampling rate. The output of the waveform generator is then mixed with a 13 GHz phase-locked dielectric resonator oscillator (PDRO) and upconverted to a higher frequency range where rotational transitions of interest are. It is worthwhile to mention that all the frequency sources, waveform generators, and PDROs, are phase locked with a quartz oscillator using a rubidium frequency standard (Stanford Research Systems SF725) as the frequency reference, so the system is phase stabilized. This allows us to coherently average the FID signal to increase the signal to noise ratio.
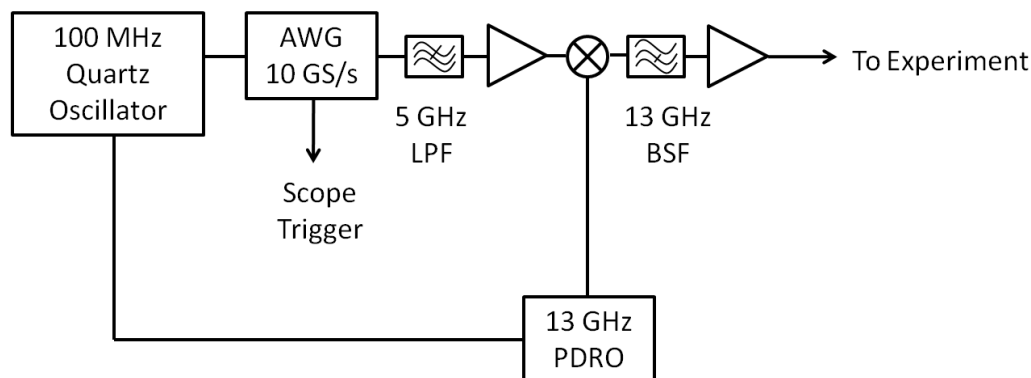
Fig. 2.2. The microwave circuit used for chirped pulse generation.

As an example, to generate a 9.907 GHz to 10.007 GHz chirped pulse, we program the arbitrary waveform generator to output a frequency sweep from 2993 MHz to 3093 MHz. A 5 GHz low pass filter (Lorch Microwave 10LP-5000-S) is used to filter out the spurious tones from the waveform generator. Then a solid-state amplifier (Minicircuit ZX-60-6013+) is used to preamplify the signal filtered by the low-pass filter. The pulse is then mixed with the 13 GHz PDRO to produce the desired 9.907

GHz to 10.007 GHz chirped pulse. Finally, we use a 13 GHz notch filter (Lorch Microwave 6BR6-13000/100-S) to remove the residual signal of the 13 GHz PDRO.

The final stage of pulse generation is power amplification. In order to maintain the power spectral density, a solid-state amplifier (Microwave Power L0818-32-T358) is only used for narrow-band chirped pulses. The time-domain figure of the 100 MHz chirped pulse and its spectrum are shown in Fig. 2.3. In addition, because FID signals decay reciprocally with pressure , the excitation pulse has to be shorter than the molecule dephasing time. In our experiments, we measure the FID at 10 mTorr, and the excitation pulse duration is optimized to 1 μs.

Alternatively, a traveling wave tube (TWT) amplifier (AR 200T8G18A) is used in combination with a step attenuator such that the output power is 30 W. This output power supports enough power spectral density and is used for a broadband chirp from 9.9 GHz to 12.3 GHz.

The lower power measurements are made to show that a low power system can be used to look for targeted molecules. By focusing the sweep time and the frequency extent, a much lower power solid state system can be used. This represents the power anticipated with low cost signal sources at these frequencies. For wider band, more generic testing the higher power TWT system was employed. This was reduced to levels that could be reached by aggressive solid state solutions at this frequency range. The resulting rotational spectra of both broadband and narrow-band excitation pulses will be discussed in the next chapter.

2.2   Analysis Cell

The analysis cell is pumped down to the sub-mTorr level, and then the sample is fed into the analysis cell. When the power amplifier is broadcasting power, the termination of the transmission line is an open circuit. Hence, two isolators are used at the input and output of the transmission line to mitigate the standing wave effect

in the waveguide, providing excitation uniformity in the sample space as well as to protect the power amplifier from being damaged by the reflection.

2.3 FID Detection

Following the chirped pulse excitation, the molecular FID detection is accomplished by a low noise amplifier (LNA), a down conversion circuit, and a digital storage oscilloscope.

We have used an LNA that has a 45 dB gain and 1.5 dB noise figure (Miteq AMF-6F-06001800-15-10P) to amplify the emission of molecular signals; a PIN diode limiter (Advanced Control Components ACLM-4619FC361K) and a solid-state switch (ATM PNR S1517D) precede the LNA to protect the LNA and the oscilloscope from the intense excitation pulse. The solid-state switch and power amplifier are triggered by TTL logic lines to provide synchronized timing control.

The digital storage oscilloscope has an operating range from DC to 12 GHz (Tektronix TDS6124C, 8 bit resolution), and therefore the molecular emission signal is downconverted by mixing with an 18.9 GHz PDRO. The recorded molecular FID after the 9.907 GHz to 10.007 GHz chirped pulse is shown in Fig. 2.4. This is an example of the time-domain re-emission signal of methanol recorded by our overmoded waveguide design rotational spectrometer.
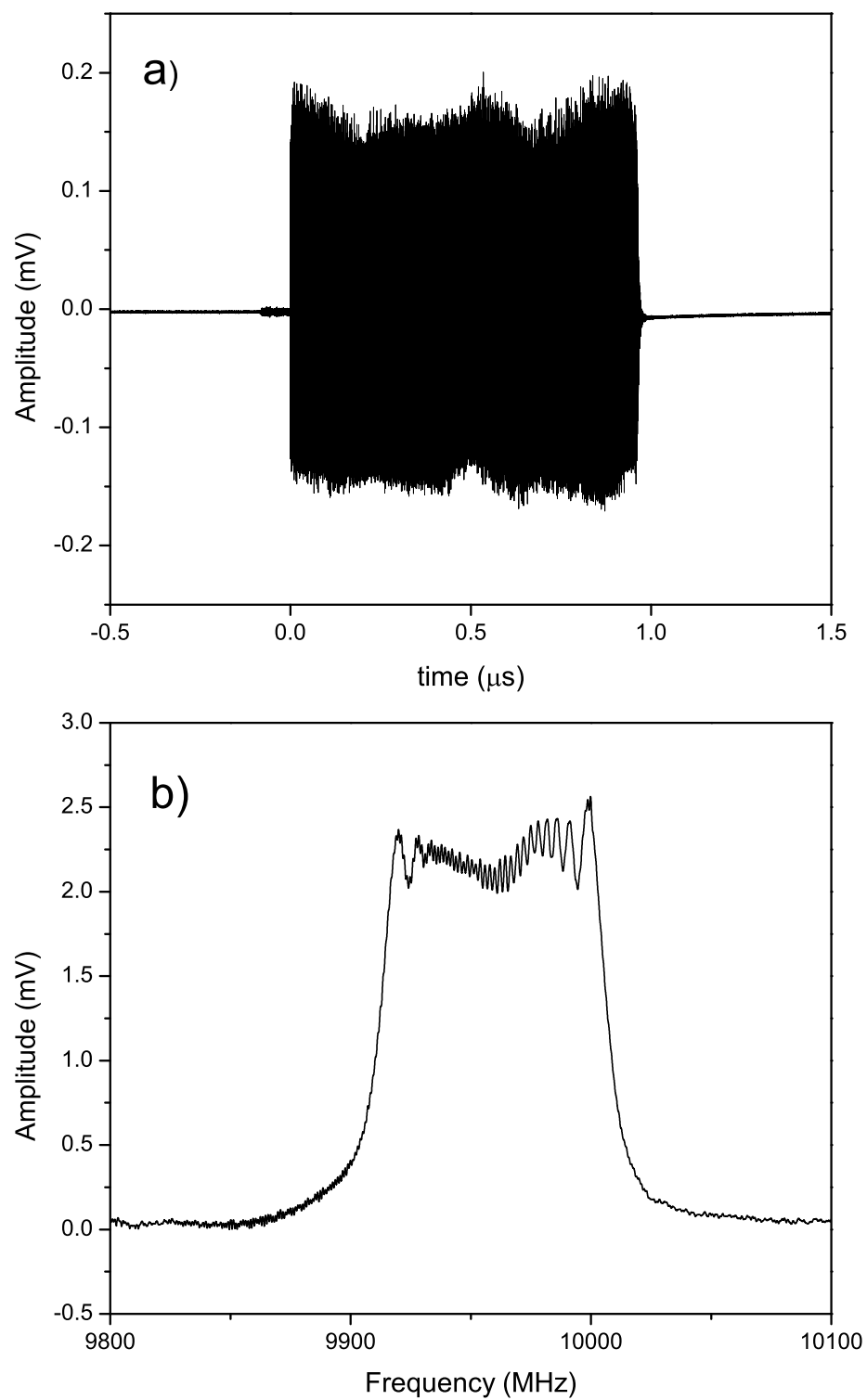
Fig. 2.3. a) Time-domain waveform of the 100 MHz excitation chirped pulse centered at 9.957 GHz. b) Spectrum of the 100 MHz chirped pulse centered at 9.957 GHz.
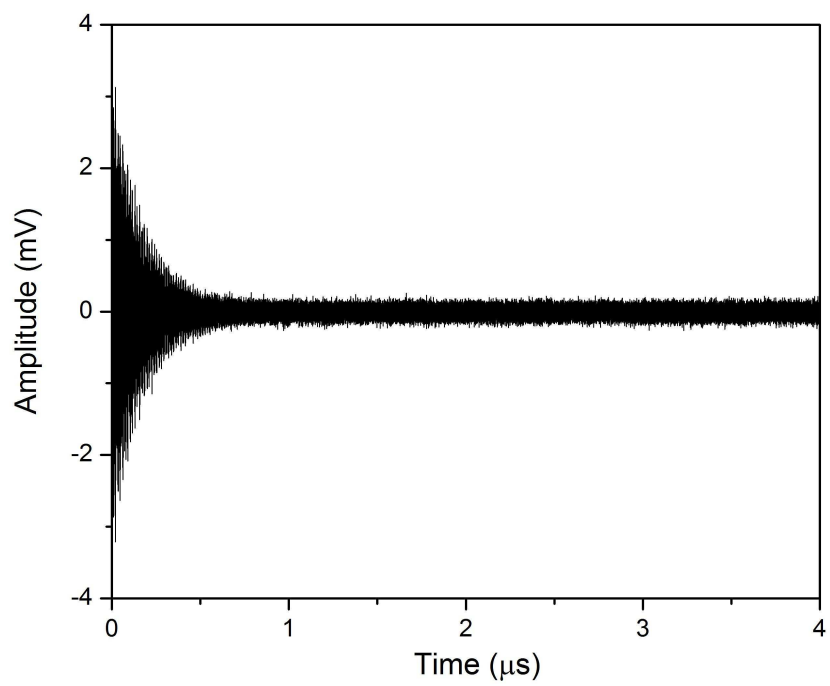
Fig. 2.4. Detected molecular FID after the 9.907 MHz to 10.007 MHz chirped pulse.

3. COMPACT ANALYSIS CELL DESIGNS

The analysis cell described in [20] utilized a pair of horn antenna to excite molecules and receive their FID signals in the vacuum chamber. Both the excitation wave and the re-emission signal propagate in free space, and the path loss ca be as large as 10.5 dB. With an input power of 1 W, only 0.09 W of power is delivered to interact with the molecules, and the electric field strength is 321 V/m in the interaction region. On contrary to an open-spaced analysis cell, in a waveguide the excitation wave can be guided to interact with molecules without radiation loss. With the same input power of 1 W, a 20 mm × 20 mm square waveguide will have an electric field strength of 2004 V/m. A larger electric field strength is preferred because the FID signal strength is proportional to the electric field [35], [36].

We focus our efforts on compact size and low power spectrometer design, and in this chapter we focus our study in closed-form analysis cell designs because they have the advantage of having high electric field strength to interact with molecules. Three analysis cell designs will be discussed in this chapter. They are non-standard waveguide and coaxial transmission line designs that are optimized to our current experiment setup as discussed in Chapter 2 and allows for a more compact-size room-temperature microwave spectroscopy system. The first design is an overmoded waveguide design, and it has a resonance-free frequency range from 8 GHz to 18 GHz. However, the available coaxial cable to waveguide adapter limits the usable frequency range. Therefore, in order to expand the operation frequency bandwidth of the analysis cell, we propose an overmoded coaxial (OMC) cable design and demonstrate a smooth impedance matching by using a spatial window function to change the outer conductor dimension of a coaxial cable. Finally, in the last design we propose a large electrical volume coaxial (LEVC) transmission line which shows an improvement in signal-to-noise ratio (SNR) over the overmoded coaxial cable.

Practical ways of changing the transmission line dimensions without creating strong unwanted resonances is very important for CP-FTMW spectrometer because one will have to wait until those resonances fade away to collect the FID signal if resonances exist. Expanded operation frequencies in OMC and LEVC are also important because they have the potential to be used to detect large/heavy molecule [34]. These designs will be addressed in details in this chapter.

A molecule dynamics model, which takes into account wall collision, self collision, and pressure dependence, that predicts signal decay in coaxial structures is also depicted in this chapter. Results of this model will be applied in Chapter 4 to predict signal strength of early start-detection time.

3.1   Overmoded Waveguide

In [21] a new RT-CP-FTMW spectrometer has been successfully demonstrated using a common WRD750 waveguide and shows good potential for use as a chemical sensor. However, the electric field is mostly concentrated within the small ridge area of the system. This region is only 4.39 mm × 3.45 mm in cross section, and hence a relatively long (8–10 m) waveguide would be required to compensate for the lack of sample space in the reduced cross section. In this section, we describe a compact RT-CP-FTMW spectrometer using an overmoded waveguide as the probe channel and demonstrate the successful measurements of methanol (CH_3OH) spectra at room temperature. The ability to conduct room-temperature measurements is an advancement toward the development of a robust microwave spectrometer chemical sensor. Compared to the non-overmoded waveguide design, our overmoded waveguide reduces the length of the probe channel while enclosing approximately the same number of molecules.

3.1.1 Design

To further inhibit collisional broadening effects and advance towards a more compact spectrometer, we developed an overmoded waveguide spectrometer. The initial design originates from a standard WR90 waveguide, which has cross-sectional dimensions of 22.86 mm × 10.16 mm, because methanol has several rotational transition frequencies in the working range of the WR90 waveguide. The width of the waveguide is kept constant while the height is increased to twice the initial height so that the final dimensions of the overmoded waveguide are 22.86 mm × 20.82 mm. Because the width is kept constant the fundamental mode, TE_{10}, will not couple to higher order TE_{n0} modes, n being an odd number, in the desired frequency range. A 6-section Chebyshev multistep transformer is used as a transformer to match the WR90 waveguide to the overmoded waveguide, where the reflection coefficient of each section is defined as

$$
\begin{aligned}
\Gamma(\theta) =& 2e^{-jN\theta}[\Gamma_0 \cos(N\theta) + \Gamma_1 \cos(N-2)\theta + ... \\
& + \Gamma_n \cos(N-2n)\theta + ...] \\
=& \frac{Z_L - Z_0}{Z_L + Z_0} \frac{1}{T_N(\sec \theta_m)} e^{-jN\theta} T_N(\sec \theta_m \cos \theta),
\end{aligned}
\tag{3.1}
$$

where

$$
\theta_m = (2 - \frac{\Delta f}{f_0} \frac{\pi}{4}),
\tag{3.2}
$$

$$
\theta = \beta \ell,
\tag{3.3}
$$

$$
\Gamma_n = \Gamma_{N-n}.
\tag{3.4}
$$

The last term in the brackets is $\Gamma_{N/2}$ if N is even and $\Gamma_{(N-1)/2} \cos \theta$ if N is odd, f_0 is the center frequency, β is the wavenumber, ℓ is the length of each step, and $T_N(\sec \theta_m \cos \theta)$ is the N-th order Chebyshev polynomial [37]. At f_0=13 GHz and maximum Γ=0.03 in the passband, we have our initial step length of 6.68 mm, and the initial characteristic impedance of each section is listed in Table 3.1. In the final design for fabrication, we have optimized the step length to 7 mm with MICIAN [38],

and the height and final characteristic impedance of each section are also listed in Table 3.1. Afterward, the stepped transformer was modified such that the transition was piecewise smooth, and the final dimensions of the overmoded waveguide cross-section are 22.86 mm × 19.61 mm, and the transition of the stepped transformer is shown in Fig. 3.1.
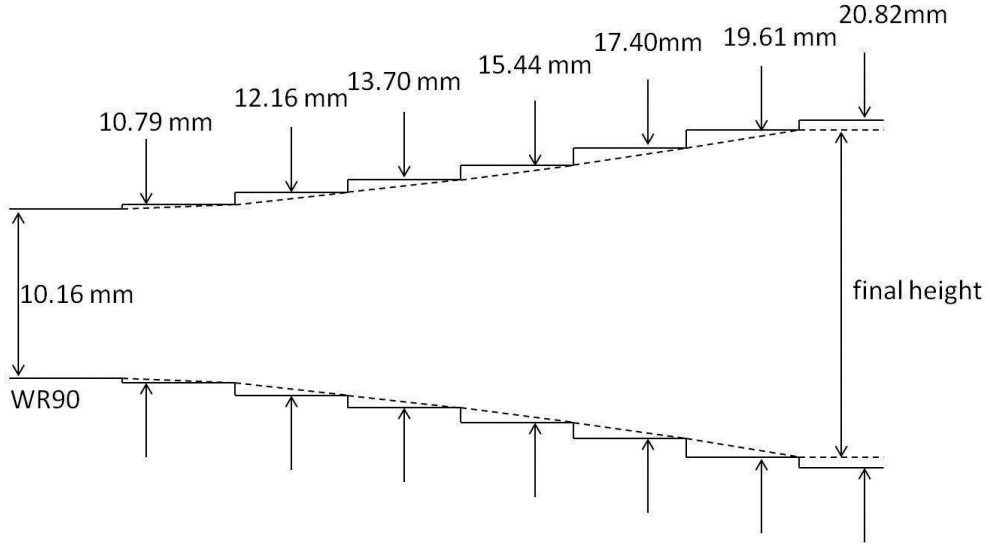
Fig. 3.1. WR90 to overmoded waveguide transition. Solid line is the design of the stepped transformer, and dashed line is the piecewise smooth model for fabrication.

However, increasing the height also increases the coupling between the TE_{10} mode and the TE_{12} and TM_{12} modes due to their field similarities in the waveguide cross-section. This coupling effect will generate unwanted resonances, and therefore S_{21} will show multiple dips.

In order to eliminate the strong coupling between the TE_{10} and TM_{12} modes and resolve the resonance in the waveguide, we have included two bifurcations in the two tapered sections to improve the field uniformity in the overmoded waveguide. With the 500 μm thick, 3 cm long bifurcations, the two coupling sections work as a power divider and combiner [39]. The input coupling section excites the overmoded waveg-

Table 3.1.

Design parameters of stepped impedance transformer

Step	Initial Impedance (Ω)	Final Impedance (Ω)	Height (mm)
1	414.1	411.9	10.79
2	453.3	464.1	12.16
3	511.9	522.9	13.70
4	585.0	589.4	15.44
5	660.0	664.1	17.40
6	723.0	748.5	19.61

uide with two simultaneous TE_{10} modes, and the output coupling section recombines the overmoded TE_{10} mode from two identical TE_{10} modes.

In addition to a reduction of wall collisions through the utilization of an overmoded waveguide, and because of the increased volume/wall surface area ratio, the attenuation factor of the waveguide is reduced to 0.008 Np/m (three-fold smaller than WRD750), which implies an improvement of the noise level and hence an improvement in sensitivity. Moreover, the increased cross-section also allows the length of the waveguide to be reduced to 22 cm while still containing 65% of the volume contained in the ridge region of a 10 m WRD750 waveguide. These benefits of the presented overmoded waveguide spectrometer prove to be advancements toward field-deployable microwave sensors.

The HFSS model of the design is shown in Fig. 3.2. The tapered coupling sections make a smooth transition from the standard WR90 waveguide to the overmoded waveguide from 8 GHz to 16 GHz, as shown in Fig. 3.3. Two commercial coaxial to rectangular waveguide adapters (HP X281A), which have the frequency range from 8.2 GHz to 12.4 GHz that includes five previously observed transitions [40], were used in order to measure the waveguide. The measured and simulation results including

these waveguide adapters are shown in Fig. 3.4. We also anticipate a tradeoff in absorption area and power: we need a higher input power in the overmoded waveguide to generate the same electrical field strength as in the WRD750 waveguide. The simulation results are shown in Fig. 3.5, and the required power for the overmoded waveguide is approximately nine-fold greater than that of WRD750.
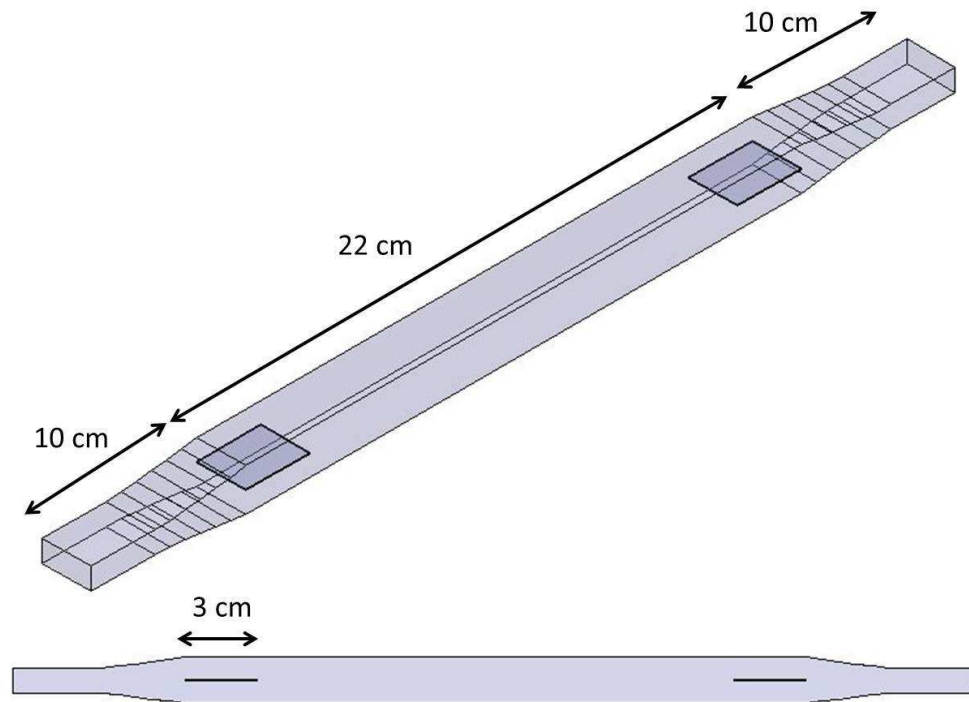
Fig. 3.2. HFSS model of the overmoded waveguide design. The input and output coupler to the WR90 waveguide is 10 cm long, and the overmoded waveguide is 22 cm long.

3.1.2 Fabrication

The overmoded waveguide spectrometer, shown in Fig. 3.6, consists of two tapered waveguide sections that function as input/output transitions (10 cm) from the WR90 waveguide to the overmoded waveguide (22 cm). Because of fabrication limitations, the overmoded waveguide had to be divided into two halves. In order to limit effects
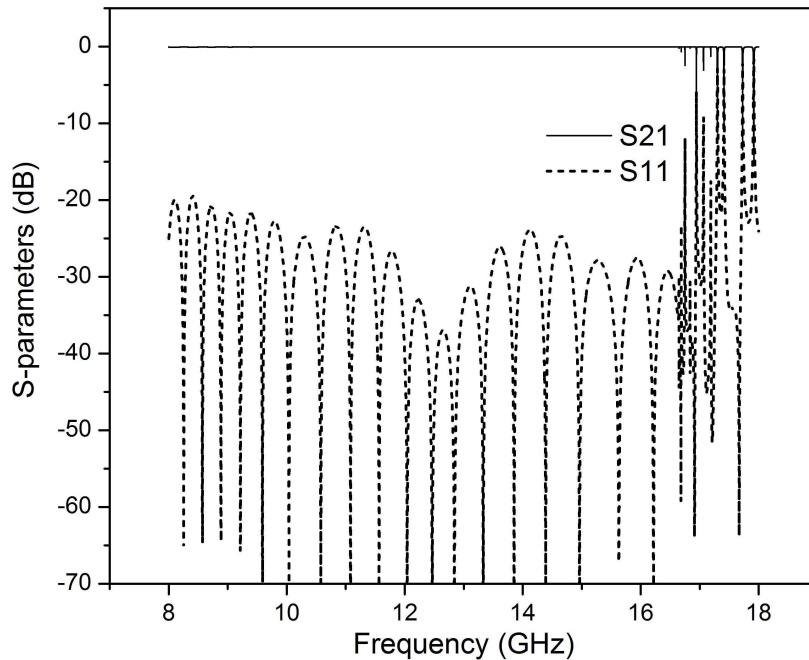
Fig. 3.3. Simulation result of the waveguide design shown in Fig. 3.2. This results shows that S_{21} is resonance free between 8 GHz to 18 GHz.

of dividing the waveguide, we chose to divide it along the E-plane where the surface current flows longitudinally along the seam. The current on the other two sidewalls does not encounter any discontinuity. Therefore, dividing the waveguide along the E-plane has the least impact on waveguide performance. The long edges of one of these pieces were grooved and sealed with two pieces of Viton O-ring strips. The input and output flanges of the overmoded waveguide were also grooved and fit with O-rings to seal the flanges with 150 μm thick mica windows. On the sidewalls of the waveguide, there are three orifices of 1 mm diameter for pumping, gas inlet, and a vacuum gauge. The overmoded waveguide can hold a vacuum of 0.01 mTorr based on a leak test with helium.
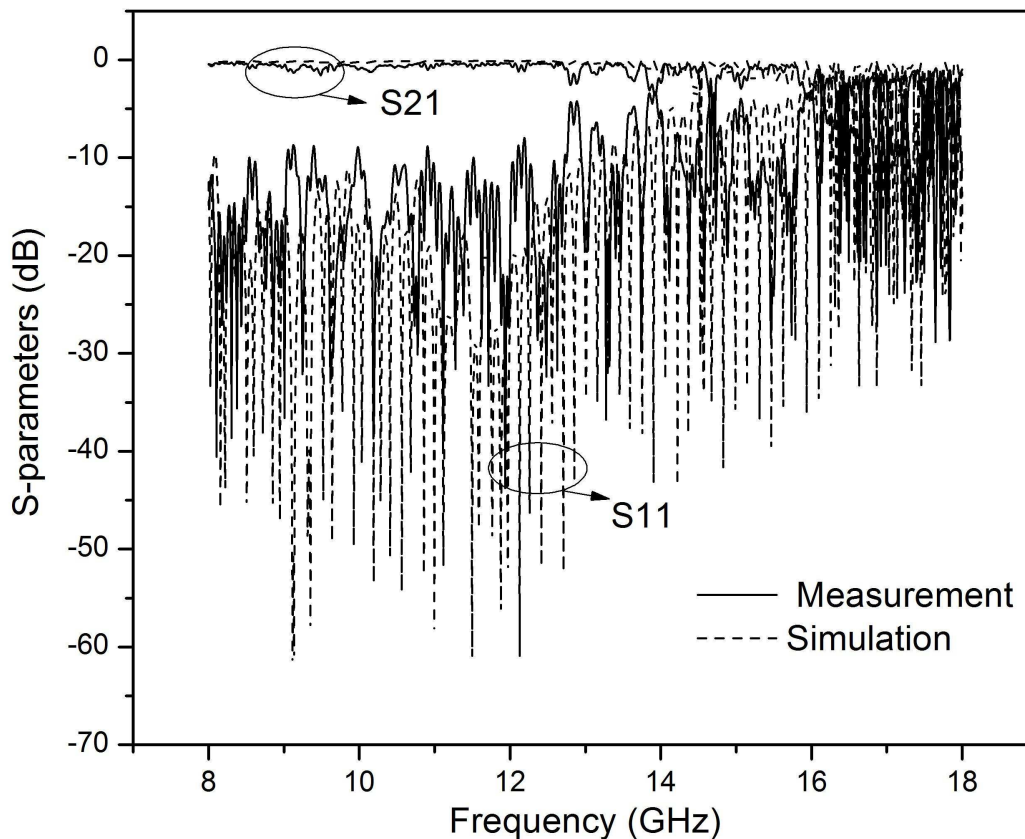
Fig. 3.4. Measured and simulated S-parameters of overmoded waveguide spectrometer. The operation frequency range is limited by the waveguide adapter (HP X281A), and resonances start to occur at above 12.4 GHz.

3.1.3 Results

The molecular FID was recorded 1 μs after the chirped pulse excites the sample. We used a 30 W output power from the TWT amplifier and we acquired a 2.4 GHz wideband spectrum with a single wideband chirped pulse. We have only targeted the frequency range from 9.9 GHz to 12.3 GHz because methanol has a relatively intense spectrum in this range. With the higher excitation power, we were able to identify five rotational transitions at 9936.1 MHz, 9978.6 MHz, 10058.1 MHz, 12178.5 MHz, and 12229.3 MHz with a single chirped pulse. The broadband spectra is shown in Fig. 3.7, and the measured and calculated rotational transitions are listed
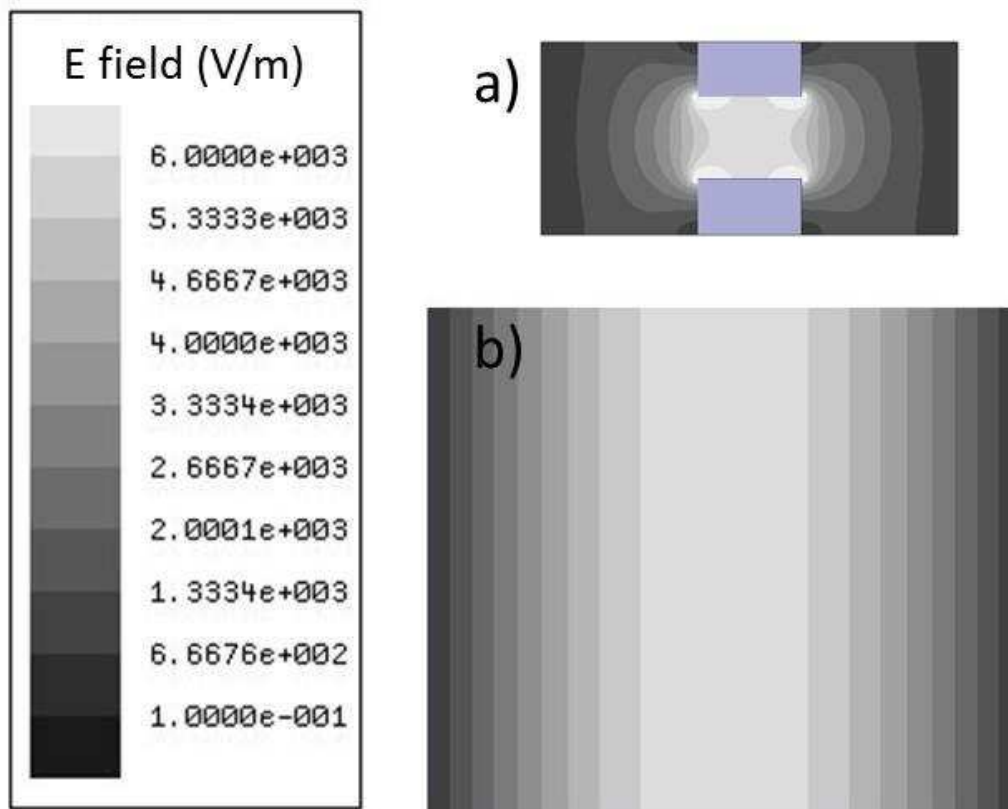
Fig. 3.5. Electric field strength of a) WRD750 waveguide at 1 W input, and b) overmoded waveguide at 9 W input.

in Table 3.2. It is noteworthy to mention that the measured frequency at 12229.3 MHz, which corresponds to the $16_{5\ 12} \leftarrow 17_{4\ 13}$ transition, cannot be measured by low temperature spectrometer because the molecule population follows a Boltzmann distribution, and the rotational quantum number $J' = 16$ and $J'' = 17$ are relatively high energy states for low temperature, namely 1 K, spectroscopy. A comparison of observable rotational transitions at room-temperature and low-temperature are shown in Fig. 3.8.

Compact integration of the waveguide with the source would require a simple amplifier. A commercial 3 W solid-state amplifier is used for two separate frequency ranges in which the methanol transition frequencies are localized: 9.907 GHz to 10.007 GHz and 12.144 GHz to 12.544 GHz. With the 100 MHz chirped from 9.907 to 10.007
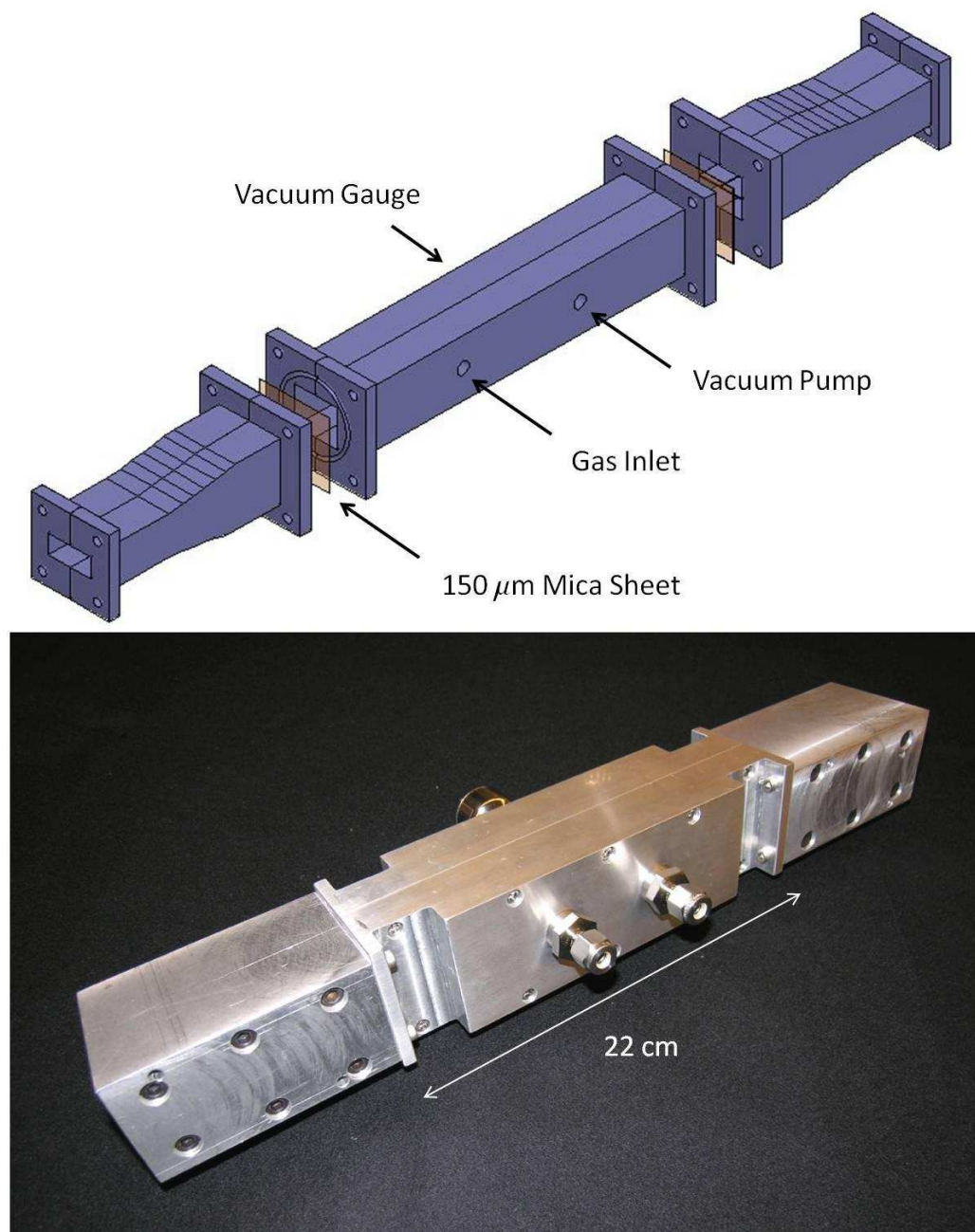
Fig. 3.6. Fabrication model of the overmoded waveguide spectrometer. The middle section of the design is sealed with two mica windows and works as the analysis cell for chemical sensing.

GHz, we have probed the rotational transitions at 9936.1 MHz and 9978.6 MHz. In addition, rotational transitions at 12178.5 MHz, 12229.3 MHz, and 12511.2 MHz were
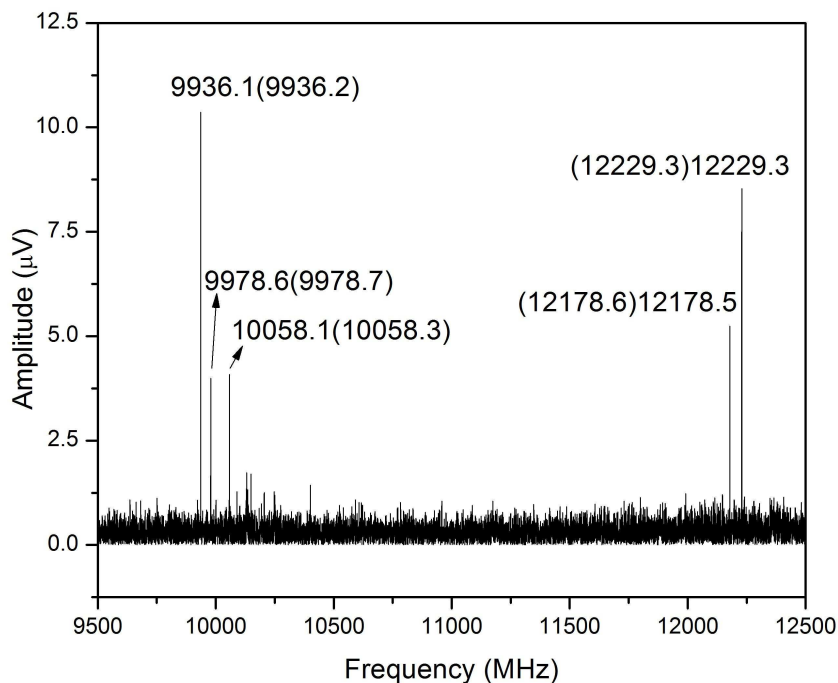
Fig. 3.7. Broadband excitation using a 30 W amplifier with a chirped pulse at the center frequency of 11.1 GHz and 2.4 GHz bandwidth with 10,000 averages. Five rotational transitions were measured using this broadband chirped pulse. Among these transitions, the frequency at 12229.3 MHz corresponds to the $16_{5\ 12} \leftarrow 17_{4\ 13}$ transition. This transition relates to high rotational quantum numbers, $J' = 16$ and $J'' = 17$, and cannot be observed with low temperature, namely 1 K, CP-FTMW spectrometer because molecules mostly occupy lower rotational states at low temperature. Theoretical calculated frequencies are shown in parentheses.

also identified by the 400 MHz chirped pulse from 12.144 GHz to 12.544 GHz. The acquired spectra by using the 3 W solid-state amplifier are show in Figs. 3.9 and 3.10. We show that we can also acquire spectrum with the concatenated waveguide with a tradeoff of power and sweep range.

The design of the overmoded waveguide provides a good transition to match the impedance of a standard WR90 waveguide to an overmoded waveguide and preserve
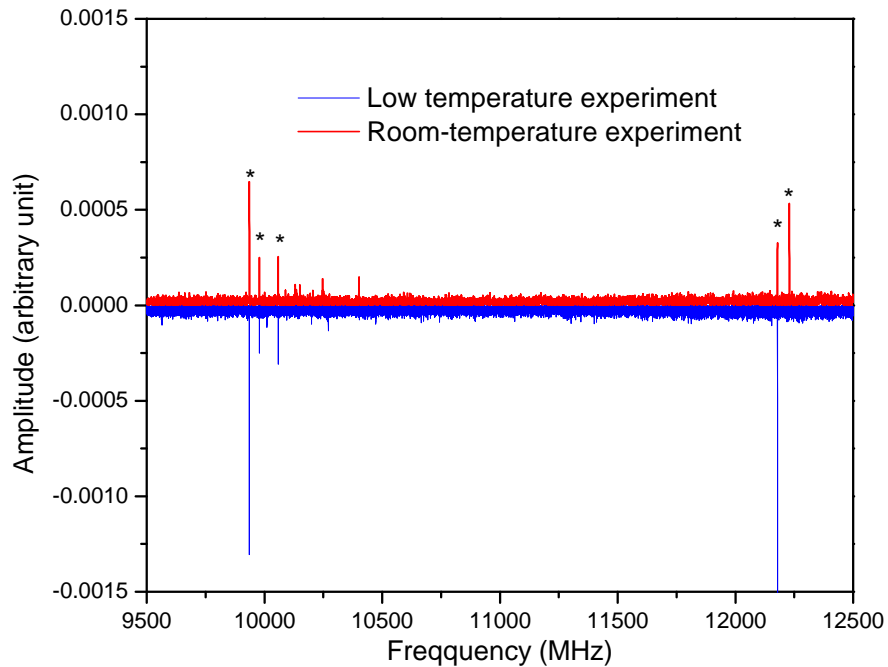
Fig. 3.8. A comparison of acquired methanol spectrum at room-temperature and low temperature. Methanol transitions are marked with asterisks. The positive amplitude spectrum is the room-temperature spectrum acquired by the overmoded weaveguide design, and the negative amplitude spectrum is acquired by the pulsed CP-FTMW spectroscopy technique, which cools down the molecule to 1 K by utilizing supersonic expansion [20]. This figure shows that the 12.229 GHZ spectral line is missing in the low temperature experiment.

the frequency range. Furthermore, the 22-cm-long overmoded waveguide contains enough chemical sample to allow for chemical detection, even though the effective volume is only 68% of a 10-meter-long WRD750 waveguide. In all, we have greatly reduced the waveguide from 10 m to 22 cm and probed 6 transitions in total, and the measured spectra shows very high accuracy, as shown in Table 3.2.

Table 3.2.
Measured and calculated rotational frequencies of the spectral lines measured with overmoded waveguide. Calculation uncertainties are included in the parenthesis.

Transition $J'_{Ka'Kc'} \leftarrow J''_{Ka''Kc''}$	Measured Frequency (MHz)	Calculated Frequency (Unc.) (MHz) [40]
$9_{-1\ 9} \leftarrow 8_{-2\ 7}$	9936.139	9936.203(0.014)
$4_{3\ 2} \leftarrow 5_{2\ 3}$	9978.635	9978.703(0.015)
$4_{3\ 1} \leftarrow 5_{2\ 4}$	10058.095	10058.281(0.015)
$2_{0\ 2} \leftarrow 3_{-1\ 3}$	12178.535	12178.561(0.015)
$16_{5\ 12} \leftarrow 17_{4\ 13}$	12229.308	12229.335(0.030)
$5_{1\ 4} \leftarrow 5_{1\ 5}$	12511.177	12511.228(0.012)
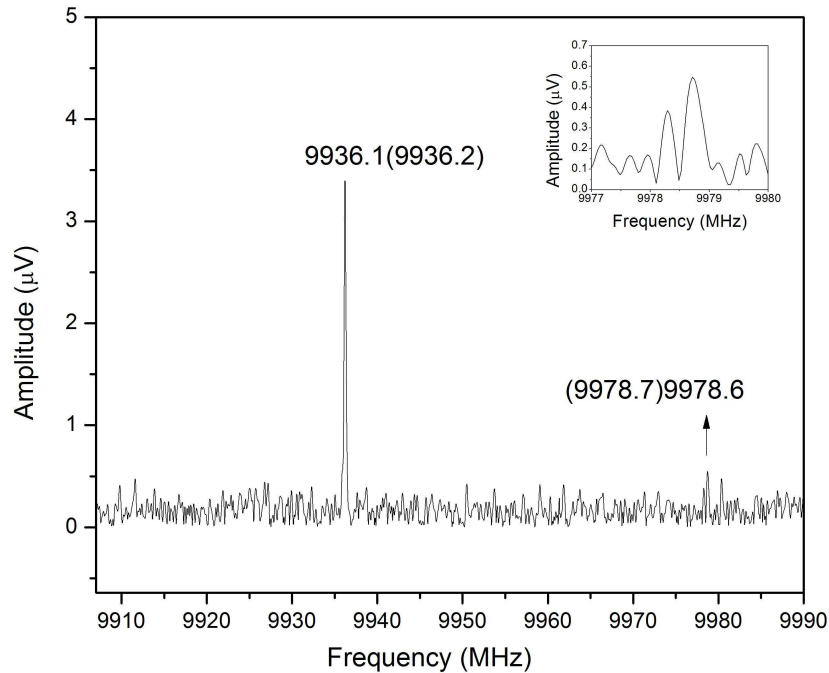
Fig. 3.9. Measured methanol spectrum using a 3 W solid-state amplifier with a chirped pulse at the center frequency of 9.957 GHz and 100 MHz bandwidth. Theoretical calculated frequencies are shown in parentheses.

3.2 Overmoded Coaxial Cable

A room-temperature chirped pulse Fourier transform microwave spectrometer is demonstrated by using a WRD750 double ridge waveguide and by the overmoded waveguide design introduced in the previous section. In the WRD750 double ridge waveguide, the operation frequency range, 7.5 GHz to 18 GHz, is limited by the waveguide cutoff frequency, and the effective sensing area is confined within the small region between the two ridges. A new overmoded waveguide design for microwave chemical sensing is demonstrated in the previous section, and the commercial available coaxial to waveguide adapters limit its operation frequency range. In order to overcome the frequency limits set by the waveguide based spectrometer designs, this
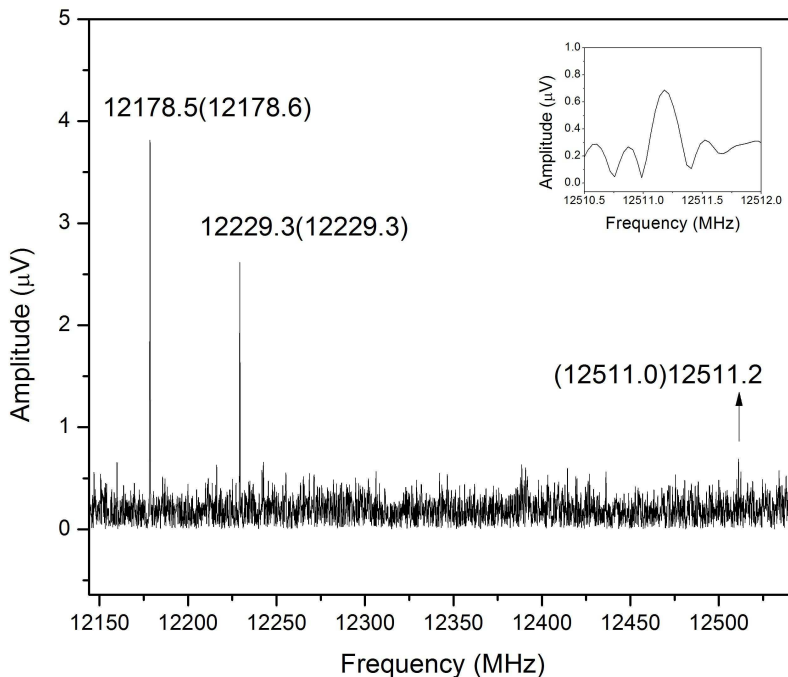
Fig. 3.10. Measured methanol spectrum using a 3 W solid-state amplifier with a chirped pulse at the center frequency of 12.344 GHz and 400 MHz bandwidth. Theoretical calculated frequencies are shown in parentheses.

section shows a new overmoded coaxial cable spectrometer design utilizing a Hamming function tapered transmission line method that provides smooth tapering to increase the spectrometer's bandwidth by 43%. The successful spectrum measurements in this section proves the application of using the overmoded coaxial cable as a chemical sensor.

3.2.1 Design

For the purpose of microwave chemical sensing using a cable, we propose an overmoded coaxial cable (OMC) design in which the radius of the coaxial cable changes

gradually in order to create more volume and to reduce wall collision effect. Typically, a coaxial cable transfers electromagnetic waves using TEM mode in general. However, coaxial TM_{mn} and TE_{mn} modes also exist and can be excited above their cutoff frequencies. Among these waveguide modes, the TM_{01} is very strongly coupled to the TEM mode because their electric field distributions are similar, as shown Fig. 3.11. When the TEM mode couples to the TM_{01} mode, the S_{21} starts to have resonance dips, and therefore the cutoff frequency of the TM_{01} mode sets the upper frequency limit of the overmoded coaxial cable.
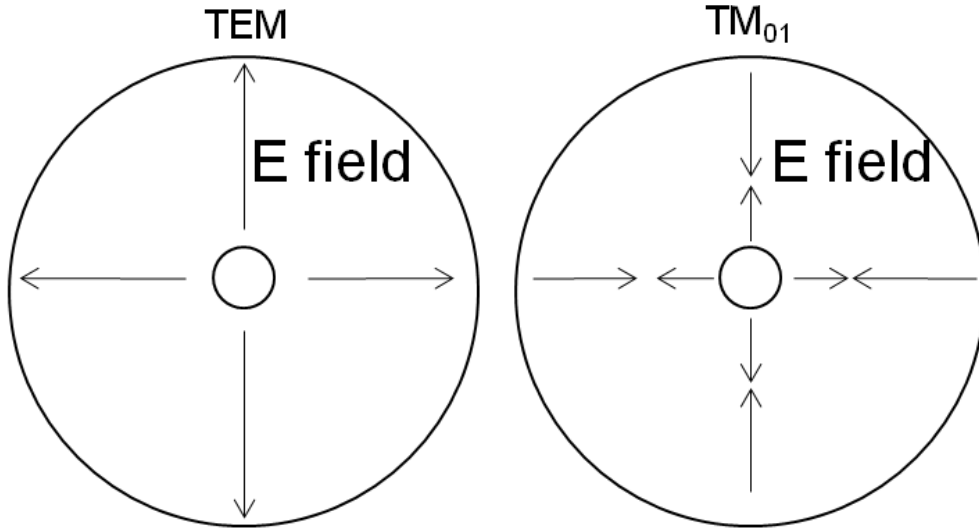
Fig. 3.11. E-field distribution of TEM and TM_{01} modes in a coaxial cable.

Cutoff frequencies of the TM_{0n} modes in a coaxial cable can be solved for numerically by using the transcendental equation

$$J_0(k_c b)Y_0(k_c a) = J_0(k_c a)Y_0(k_c b) \tag{3.5}$$

where $J_0(x)$ and $Y_0(x)$ are Bessel functions of the first and second kind, a and b are the inner and outer radius of the coaxial cable, and k_c is the cutoff wavenumber of the TM_{0n} mode. Details of the derivation of Eq. (3.5) are given in Appendix A.

With a center conductor radius of 0.5 mm and the outer conductor radius of 8 mm, the cutoff frequency of the TM_{01} mode is 18.9 GHz, which is optimized in frequency

in our current experiment setup. Plot of the numerical solution is shown in Fig. 3.12. k_c of the TM_{01} mode is 395.1 m^{-1}.
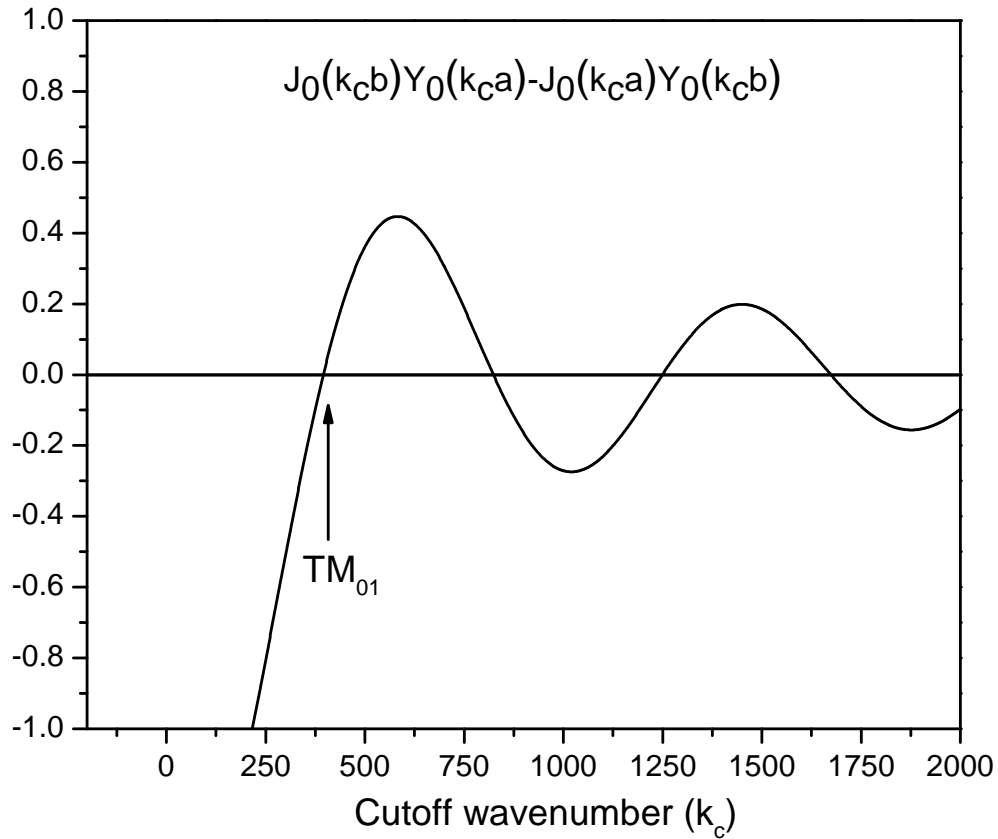
Fig. 3.12. Plot of numerical solutions of Eq. (3.5) with $a = 0.5$ mm and $b = 8$ mm. Each intersection of the curve with the x-axis indicates a solution of the transcendental function, and the solution of TM_{01} is marked with an arrow.

In order to have a smooth impedance transition for the overmoded coaxial cable to match a 2.4 mm connector, a smooth taper profile needs to be applied. Exponential taper is a very general way to taper a transmission line; however, Hamming window function taper provides a more compact taper length [41]. Fig. 3.13 compares the reflection of Hamming function taper and exponential taper versus electrical length of of a transmission line, and the taper profiles are shown in Fig. 3.14. The applied Hamming tapered transmission line method defines the functions
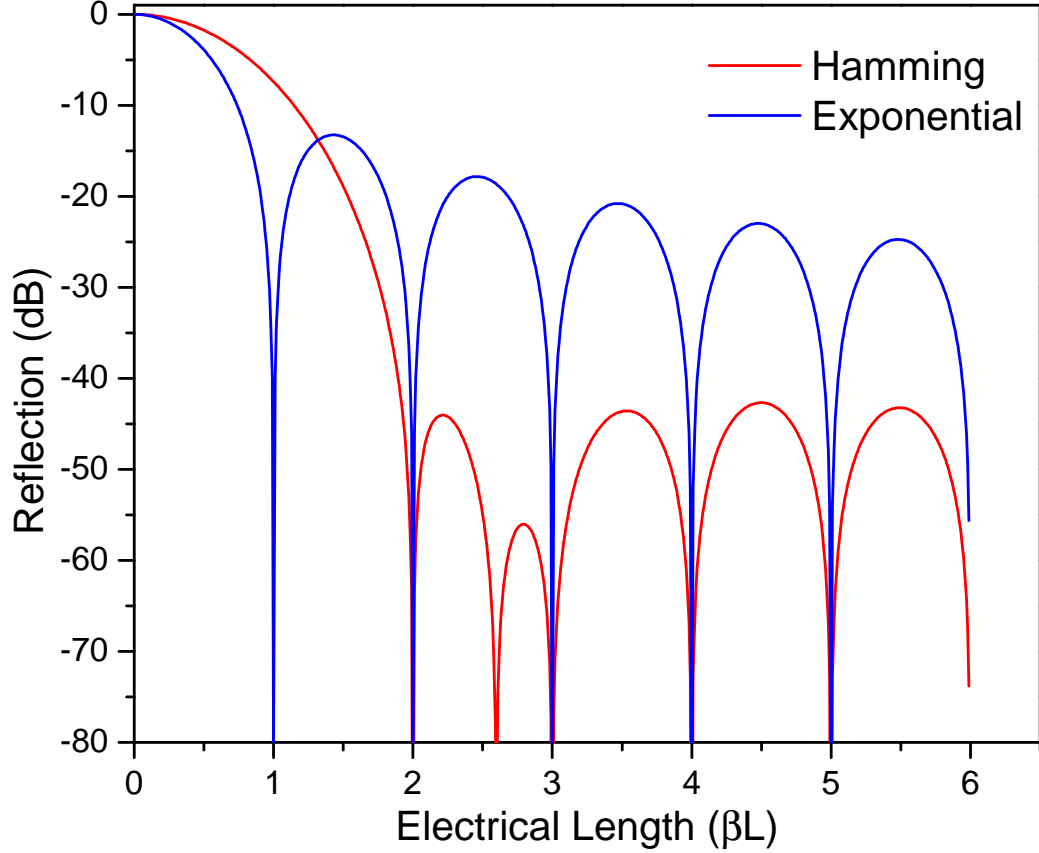
Fig. 3.13. Comparison of Hamming window function taper and exponential taper. As shown in the figure, Hamming function taper provides a more compact taper length to achieve the same return loss.

$$A(x) = 0.54\frac{x - L/2}{L} + 0.46\frac{\sin(2\pi\frac{x-L/2}{L})}{2\pi} + 0.27 \qquad (3.6)$$

$$\tilde{z}_0(x) = \tilde{z}_L^{A(x)/0.54} \qquad (3.7)$$

where $\tilde{z}_0(x)$ is the normalized characteristic impedance along the taper of the coaxial cable, $\tilde{z}_L$ is the normalized characteristic impedance of the overmoded coaxial cable, and L is the taper length. The final design is shown in Fig. 3.16, and measured and simulated S-parameters are shown in Fig. 3.15. The return loss falls below -10 dB from 3 GHz to 18 GHz.
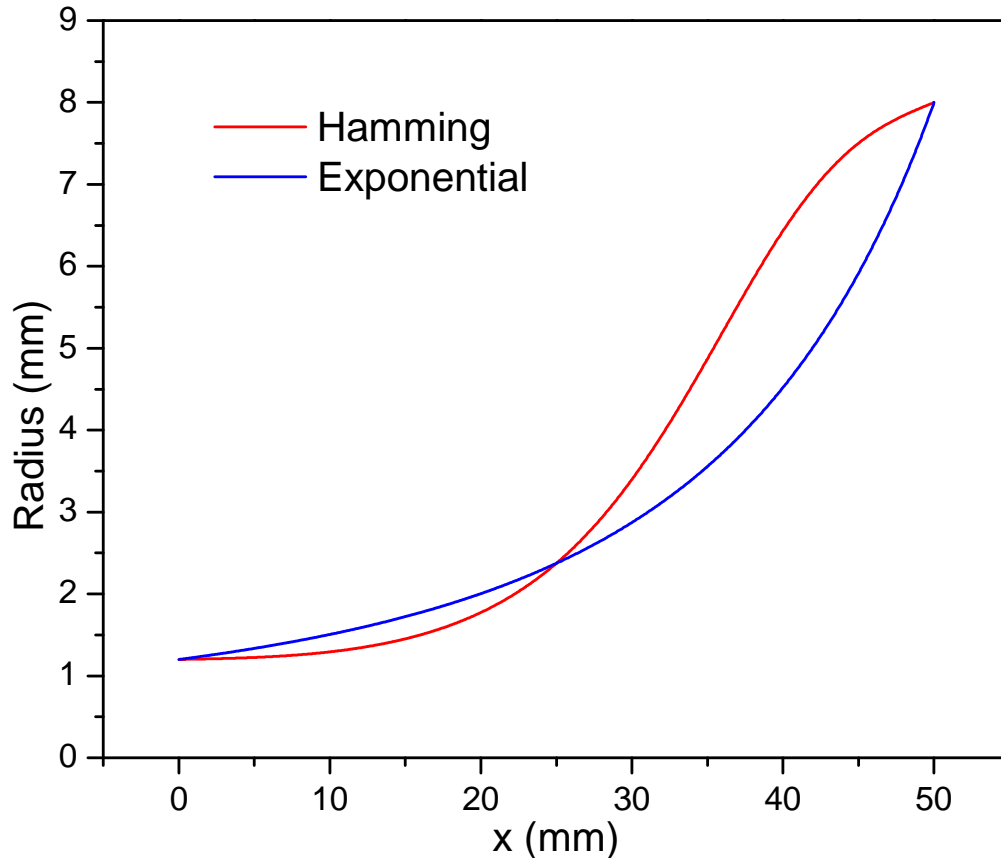
Fig. 3.14. Comparison of Hamming window function and exponential taper profiles.

3.2.2 Fabrication

The outer conductor of the overmoded coaxial cable is divided along the longitudinal direction, Fig. 3.18(a), which is parallel to the flow of surface current for the TEM mode. This produces the least effect on the electrical performance and makes fabrication practical. The center pin is supported by two pieces of Evonik Rohacell dielectric, shown in Fig. 3.18(b) that has a permitivity $\epsilon \sim 1$ so that the characteristic impedance can be matched with the 2.4 mm connector. In order to make the overmoded coaxial cable porous to the chemical to be sensed, we designed 6 circular orifices of 2 mm diameter along the coaxial cable.

The overmoded coaxial cable is set in a 32 cm long nipple, and the vacuum gauge, pump, chemical inlet, and electrical feedthroughs are connected with the ISO standard
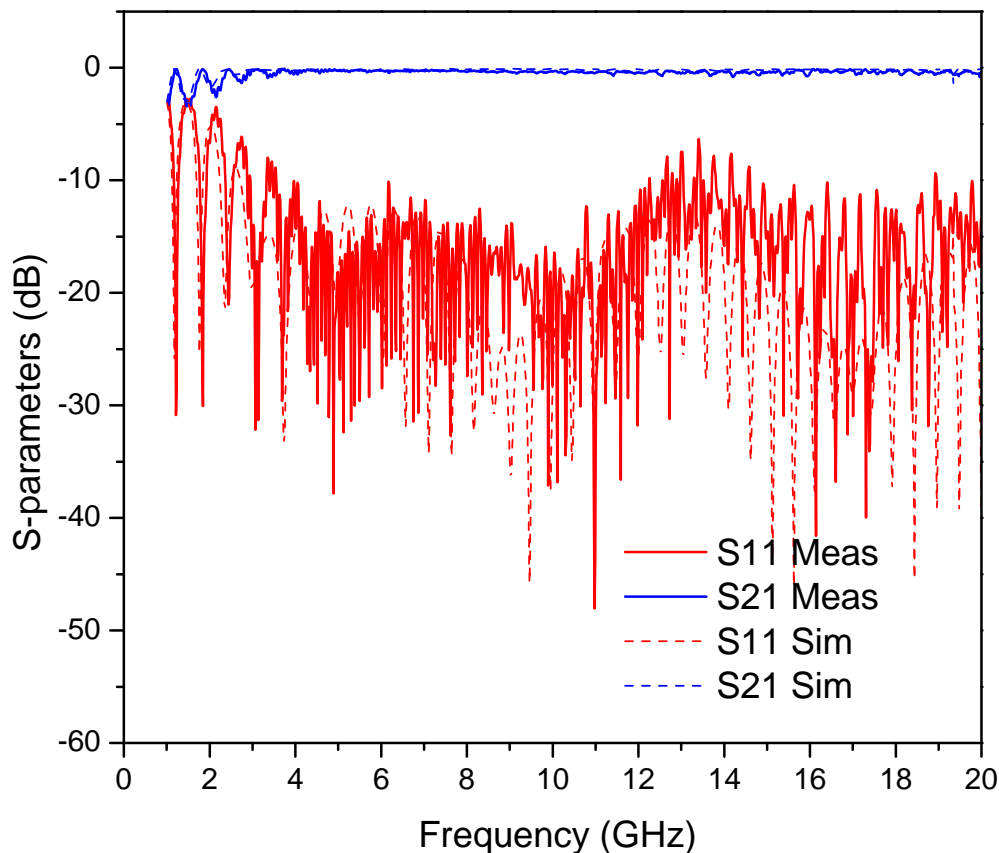
Fig. 3.15. Measured and simulated S-parameters of the overmoded coaxial cable. The measured and simulated S_{21} are in very good agreement and are almost indistinguishable in the figure. The measured S_{11} is slightly degraded due to fabrication error and two small pieces of dielectric (Evonik Rohacell) at both ends of the cable to support the center conductor.

Klein Flange system, as shown in Fig. 3.17, that offers quick and easy connection and reaches a vacuum of 7.5 mTorr in a very short amount of time.

3.2.3 Results

Three methanol rotational transition frequencies were observed by using two chirped pulses in our overmoded coaxial cable spectrometer. The bandwidth of the two chirped pulses were limited to 100 MHz and 400 MHz because the 3 W solid-state

$$D(x) = \exp\left[\ln 2.4 \left(\frac{\ln 16}{\ln 2.4} \right)^{A(x)/0.54} \right]$$
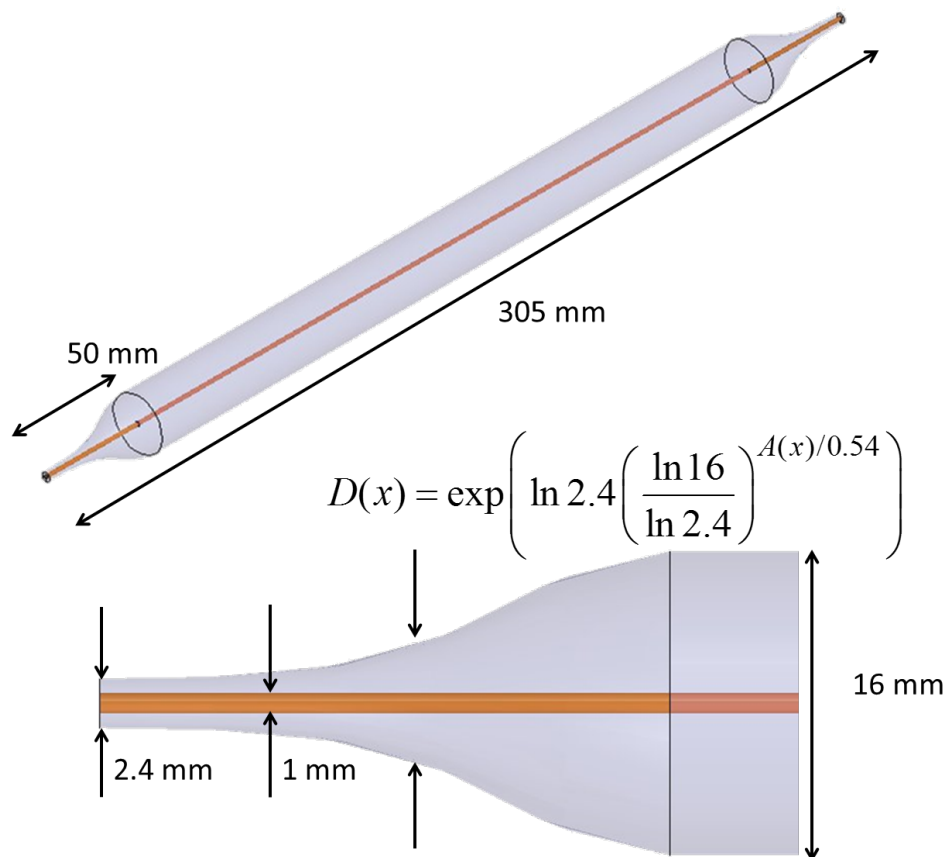
Fig. 3.16. Fabricated overmoded coaxial cable. Close view of the taper and diameter $D(x)$ of the overmoded coaxial cable along the longitudinal direction (x-direction) are also shown.

amplifier could not provide enough power spectral density for wideband chirped pulse to excite the molecules. After amplification by the 3 W solid-state power amplifier, the 9907 MHz to 10007 MHz chirped pulse successfully probed the $9_{-1\ 9} \leftarrow 8_{-2\ 7}$ transition with a 0.0006% error, shown in Fig. 3.19. The other chirped pulse that spans from 12144 MHz to 12544 MHz probed the $2_{0\ 2} \leftarrow 3_{-1\ 3}$ transition with a 0.0014% error and the $16_{5\ 12} \leftarrow 17_{4\ 13}$ transition with a 0.0015% error, shown in Fig. 3.20. These three observed rotational transition frequencies show very high accuracy with respect to their associated calculated frequencies [40].
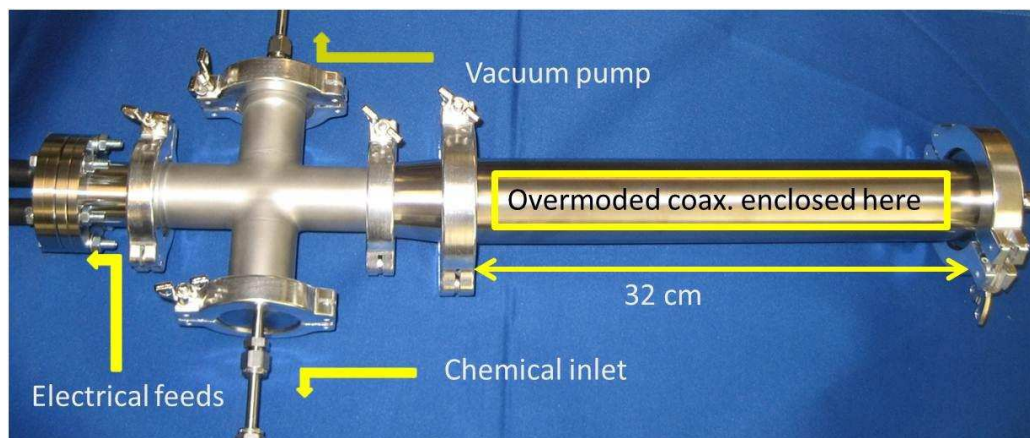
Fig. 3.17. The overmoded coaxial cable is enclosed in the 32 cm long nipple that is connected to a 4-way cross. The electrical feeds, vacuum pump, and chemical inlet are connected to this 4-way cross with with KF flanges that provide quick and easy connection.

In order to achieve a broadband spectrum, a 30 W excitation power is used. Because we upconvert the chirped pulse created by the AWG by mixing with a 13 GHz local oscillator, two chirped pulses, 9.9 GHz to 12.3 GHz and 13.7 GHz to 16.1 GHz are generated simultaneously. With this more aggressive excitation power, we probed 4 spectrums in the 9.9 GHz to 12.3 GHz and from 13.1 GHz to 16.5 GHz. Overall, eight rotational transitions are observed using the overmoded coaxial cable. Among the measured transitions, the $25_{4\ 22} \leftarrow 24_{5\ 19}$, $20_{-1\ 19} \leftarrow 21_{-2\ 19}$, $25_{4\ 21} \leftarrow 24_{5\ 20}$, and $16_{-2\ 15} \leftarrow 15_{-3\ 13}$ are not measured in the low-temperature spectroscopy, while the $25_{4\ 22} \leftarrow 24_{5\ 19}$, $20_{-1\ 19} \leftarrow 21_{-2\ 19}$, and $25_{4\ 21} \leftarrow 24_{5\ 20}$ are newly observed transitions [40]. Table 3.3 shows all measured spectral lines using the overmoded coaxial cable.

3.3 Large Electrical Volume Coaxial Cable

A smooth transition applied to the outer conductor of a coaxial transmission line is introduced in the previous section and the application of such transmission line in microwave chemical sensing is demonstrated. In order to further improve

Table 3.3.
Measured and calculated (with uncertainty) rotational frequencies of
the spectral lines measured with overmoded coaxial cable.

Transition $J'_{Ka'Kc'} \leftarrow J''_{Ka''Kc''}$	Measured Frequency (MHz)	Calculated Frequency (Unc.) (MHz) [40]
$9_{-1\ 9} \leftarrow 8_{-2\ 7}$	9936.139	9936.203(0.014)
$4_{3\ 2} \leftarrow 5_{2\ 3}$	9978.635	9978.703(0.015)
$2_{0\ 2} \leftarrow 3_{-1\ 3}$	12178.535	12178.561(0.015)
$16_{5\ 12} \leftarrow 17_{4\ 13}$	12229.308	12229.335(0.030)
$25_{4\ 22} \leftarrow 24_{5\ 19}$	15214.083	15214.619(0.160)
$20_{-1\ 19} \leftarrow 21_{-2\ 19}$	15303.576	15304.866(0.630)
$25_{4\ 21} \leftarrow 24_{5\ 20}$	15642.398	15642.781(0.163)
$16_{-2\ 15} \leftarrow 15_{-3\ 13}$	16395.573	16395.861(0.026)
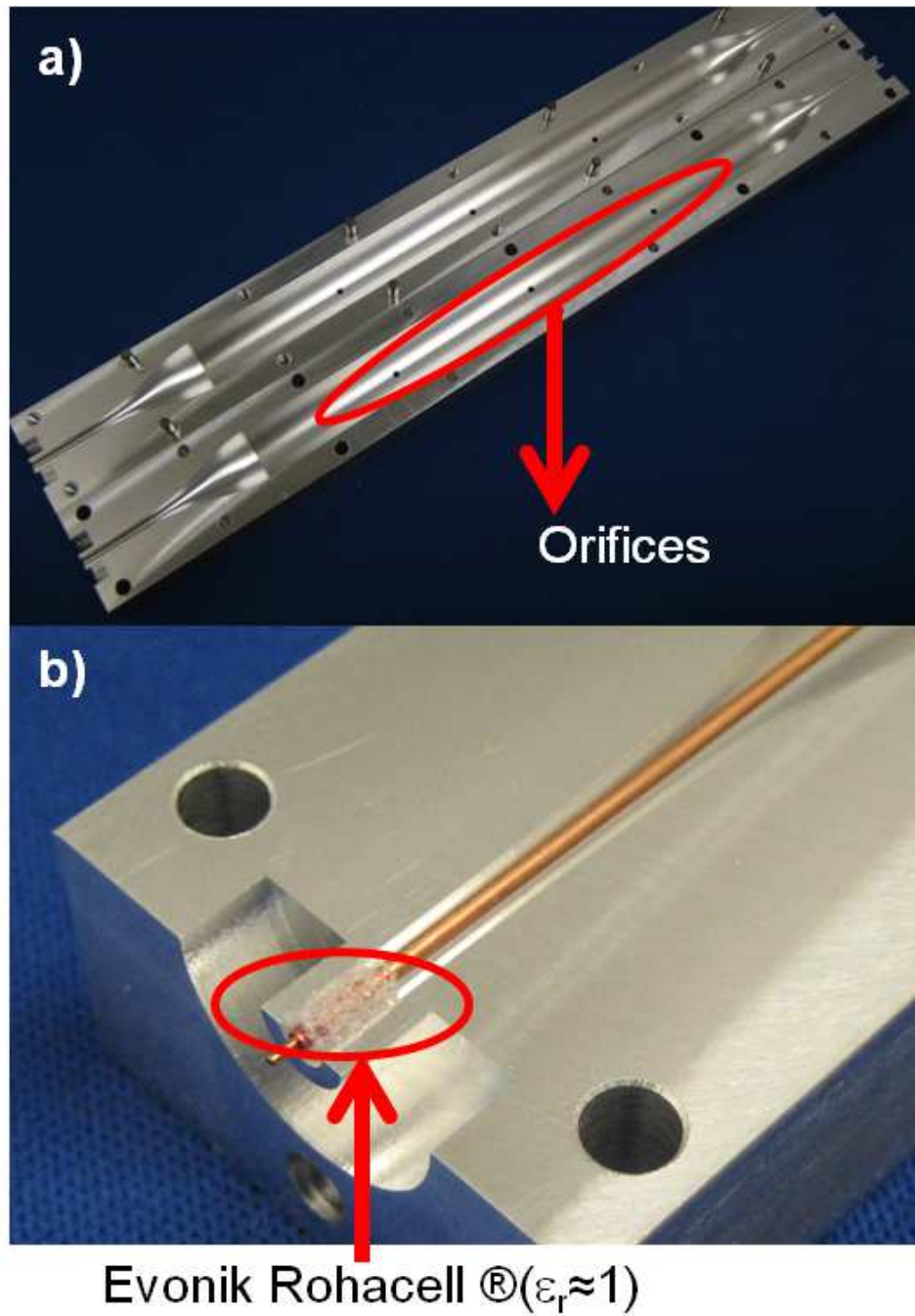
Fig. 3.18. (a) Fabrication model of the overmoded coaxial cable. Three orifices are shown in each half of the outer conductor. (b) The center conductor is supported by Evonik Rohacell dielectric.
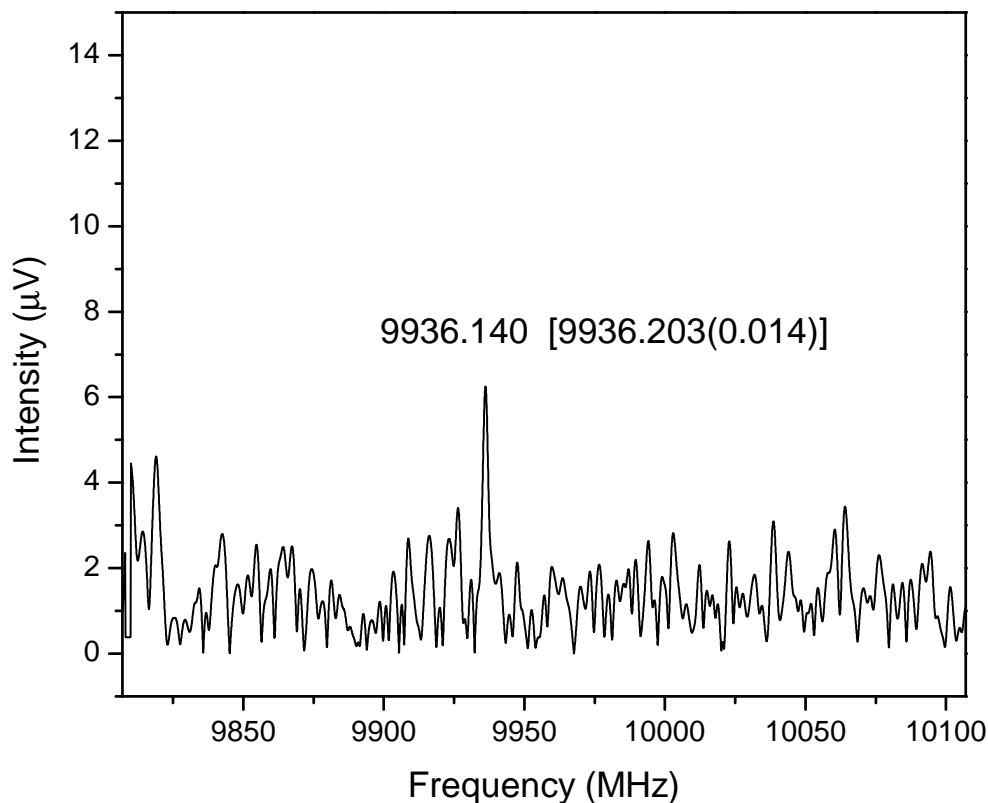
Fig. 3.19. Narrowband spectrum measured with the 3 W solid-state power amplifier and the 9907 MHz to 10007 MHz chirped pulse. Measured frequency of the $9_{-1\ 9} \leftarrow 8_{-2\ 7}$ transition is shown in the figure. Calculated frequency with uncertainty is shown in the bracket.

the performance of a microwave spectrometer for chemical sensing, we seek solutions for more rapid detection, higher resolution spectrums, and stronger molecular signals that help the chemical detection specificity. Specifically, the microwave design focuses on the ability to excite a large number of molecules and allowing them to ring for an extended time to increase the total signal measured. As few averages as possible are required to have near real time collection in the field.

In this section, we introduce a new large electrical volume coax (LEVC) design whose outer conductor and inner conductor profiles are both tapered to further increase the total volume of a coaxial line at a fixed length, and a smooth transition to
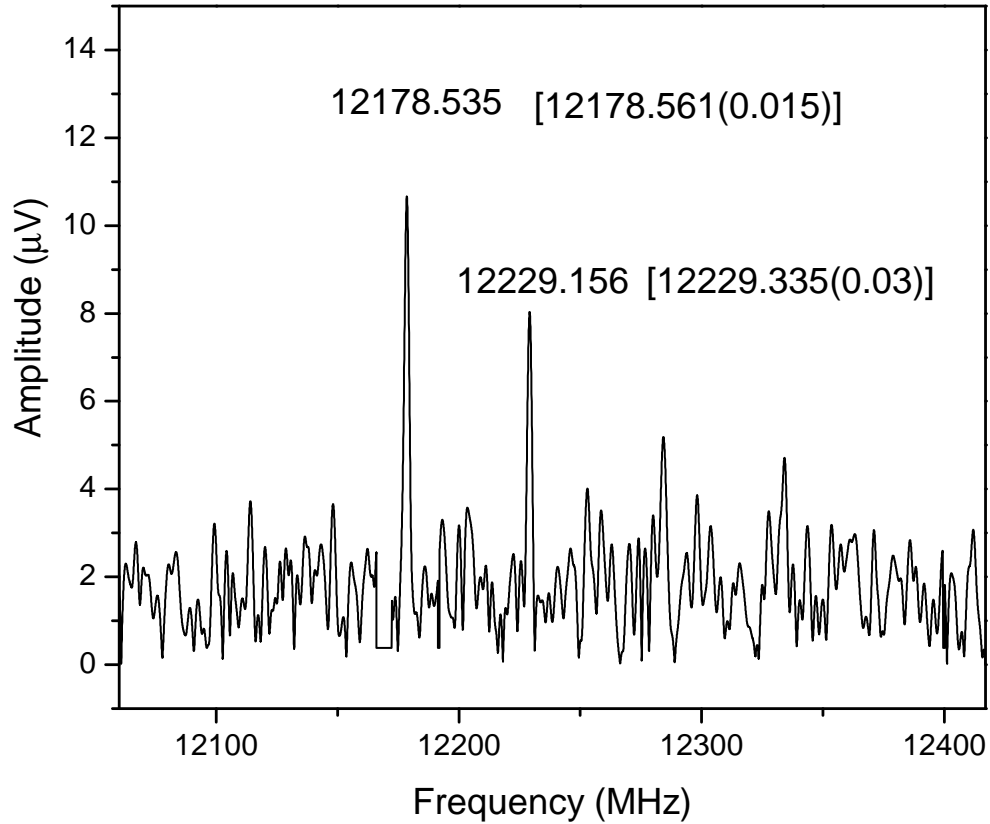
Fig. 3.20. Narrowband spectrum measured with the 3 W solid-state power amplifier and the 12144 MHz to 12544 MHz chirped pulse. Measured frequencies of the $2_{0\ 2} \leftarrow 3_{-1\ 3}$ and $16_{5\ 12} \leftarrow 17_{4\ 13}$ transitions are shown in the figure. Calculated frequencies with uncertainties are shown in brackets.

match coaxial transmission lines of different characteristic impedances were demonstrated. An comparison of cross-section area of this large electrical volume coaxial cable to the overmoded coaxial cable is shown in Fig. 3.23.

3.3.1 Design

We increase the dimensions of a coaxial transmission line to maximize the cross-section area, and hence volume at a fixed length, to use the transmission line as the analysis cell. In order to provide a smooth transition to the dimension change
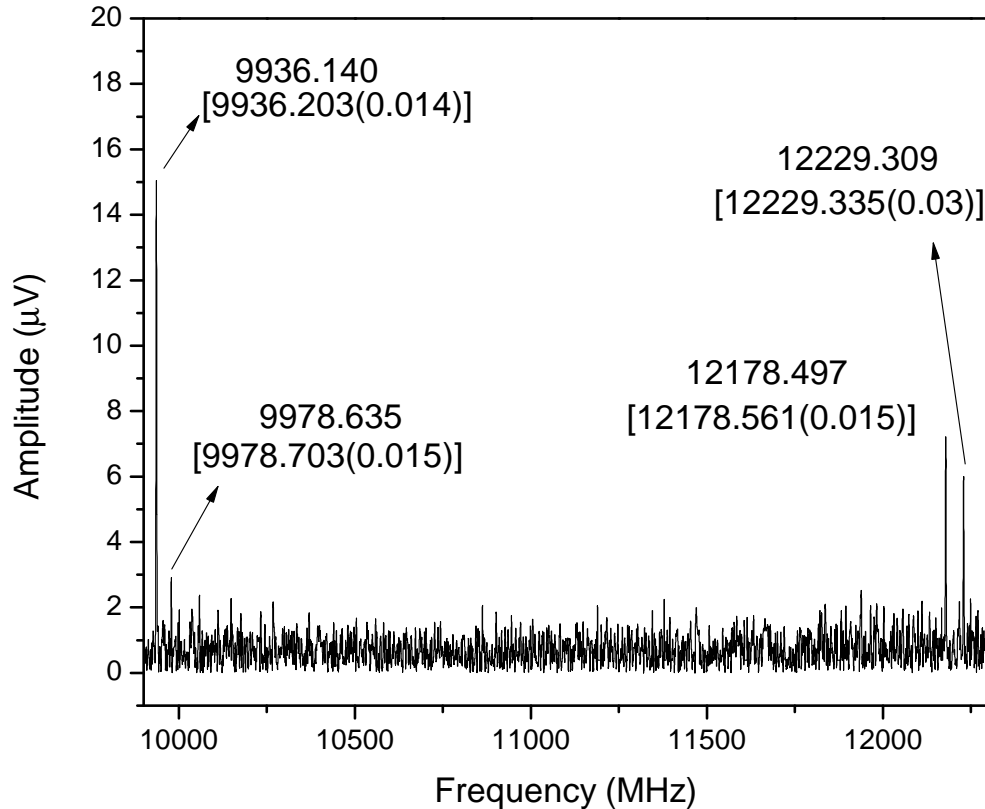
Fig. 3.21. Broadband spectrum acquired by the 9900 MHz to 12300 MHz chirped pulse. Four rotational transitions, $9_{-1\ 9} \leftarrow 8_{-2\ 7}$, $4_{3\ 2} \leftarrow 5_{2\ 3}$, $2_{0\ 2} \leftarrow 3_{-1\ 3}$, and $16_{5\ 12} \leftarrow 17_{4\ 13}$, are measured as shown in the figure. Their corresponding calculated frequencies and uncertainties are shown in the brackets.

in the inner and outer conductor, we applied the normalized impedance function described in Eq. (3.7) to define the characteristic impedance along the longitudinal direction, x-direction, of the transmission line, where $\tilde{z}_L$ is the normalized characteristic impedance of the coax at the final dimensions. In this equation, $A(x)$ is the window function as defined in Eq. (3.6), where L is the taper length. Therefore, along with the characteristic impedance of a coaxial cable defined in Eq. (3.8), the radius of the inner and outer conductor is defined in Eq. (3.9) and Eq. (3.10), where arb in Eq. (3.9) is an arbitrary number no greater than 0.5. The final outer conductor radius is 2.5 cm, and the final inner conductor radius is 1.74 cm, as shown in Fig. 3.28(a).
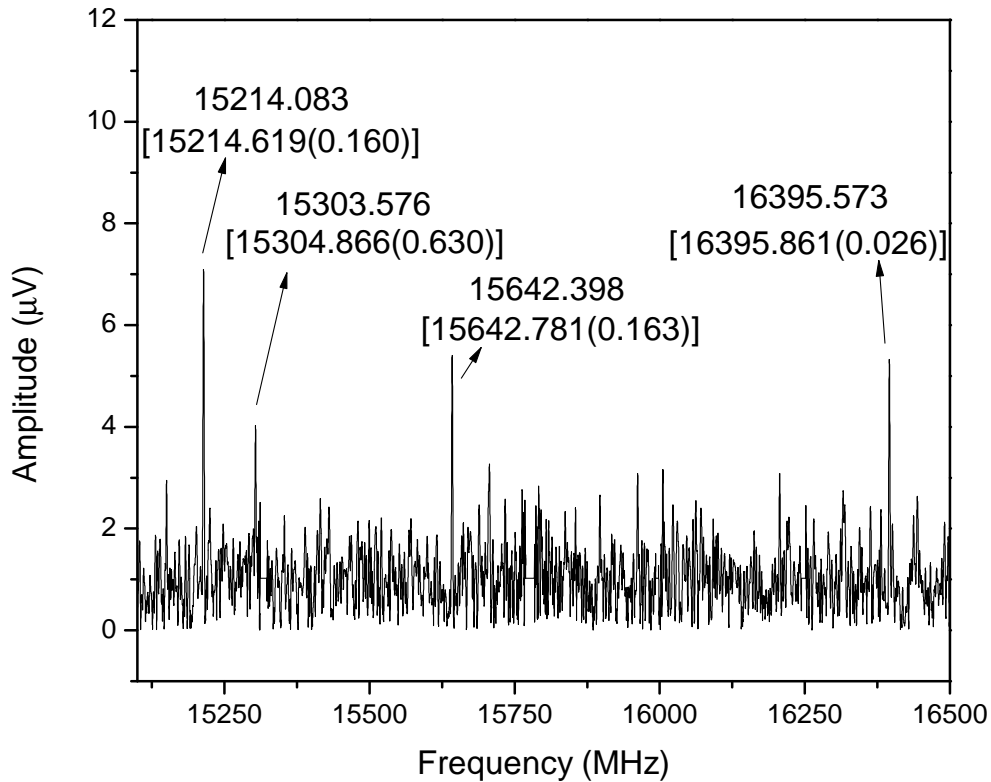
Fig. 3.22. Broadband spectrum acquired by 13700 MHz to 16100 MHz chirped pulse. Four rotational transitions, $25_{4\ 22} \leftarrow 24_{5\ 19}$, $20_{-1\ 19} \leftarrow 21_{-2\ 19}$, $25_{4\ 21} \leftarrow 24_{5\ 20}$, and $16_{-2\ 15} \leftarrow 15_{-3\ 13}$, are measured as shown in the figure. Their corresponding calculated frequencies and uncertainties are shown in the brackets.

These dimensions are chosen according to Eq. (3.5) such that coupling between the TEM mode and the TM_{01} mode is avoided, and a resonance-free passband to 17.5 GHz can be expected [42].

$$Z_0 = \frac{1}{2\pi}\sqrt{\frac{\mu}{\varepsilon}}\ln\frac{a}{b}$$

$a =$ inner conductor radius

$b =$ outer conductor radius

(3.8)
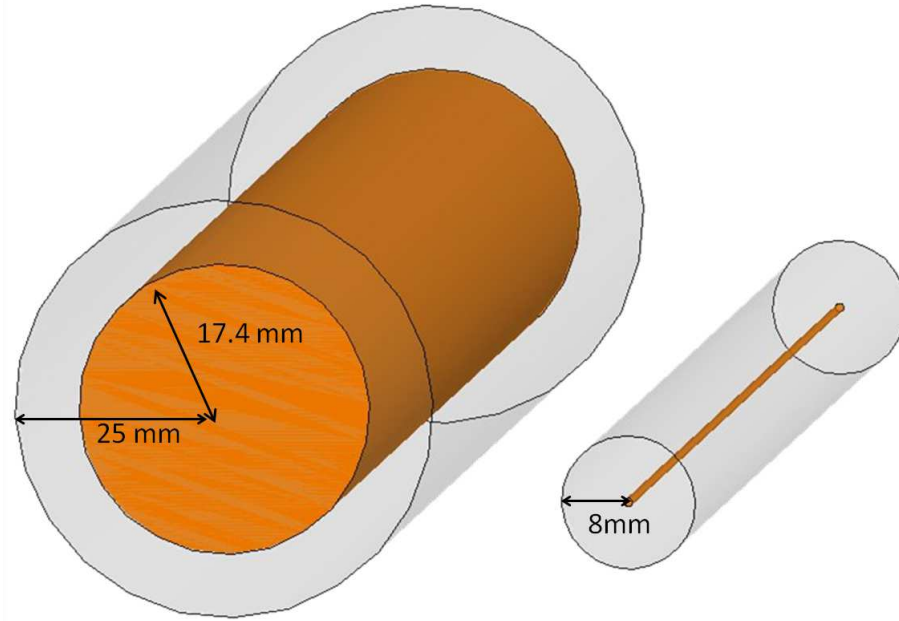
Fig. 3.23. Cross section of the large electrical volume coax and the 8 mm overmoded coax are shown side-by-side for cross-section area comparison.

$$a(x) = \text{arb} \cdot \text{Exp}\left(\ln\frac{0.5}{\text{arb}} \left(\frac{\ln\frac{17.4}{\text{arb}}}{\ln\frac{0.5}{\text{arb}}} \right)^{\frac{A(x)}{0.54}} \right) \tag{3.9}$$

$$b(x) = 0.5 \cdot \text{Exp}\left(\ln\frac{1.2}{0.5} \left(\frac{\ln\frac{25}{0.5}}{\ln\frac{1.2}{0.5}} \right)^{\frac{A(x)}{0.54}} \right) \tag{3.10}$$

$$\text{arb} > 0.5 \tag{3.11}$$

In practice, the center conductor needs to be supported in the air-filled coax, and therefore dielectric supports must be included in the design to support the weight of the center conductor. The dielectric supports need to be designed and positioned carefully because they will enhance coupling between TEM mode and TE_{m1} mode, which, in our case is the strong coupling between TEM mode and TE_{41} mode.

The S-parameter simulation of a design with 4 dielectric supports is shown in Fig. 3.24 as an example to demonstrate strong resonances caused by the strong cou-

pling between the TEM mode and the TE_{41} mode, and Fig. 3.25 shows the simulated S-parameters of an ideal air-filled large electrical volume coaxial cable as a comparison. In Fig. 3.24, the 4 dielectric supports line up with common electric fields as in the TEM mode, as shown in Fig. 3.26(a) and Fig. 3.26(b). The strong coupling between the TEM mode and the TE_{41} mode can be eliminated when we have dielectric supports line up with both common and differential electric fields, shown in Fig. 3.26(c). Therefore, in our final design, we chose to use 8 dielectric supports for the center conductor. Measured and simulated S-parameters are shown in Fig. 3.27.
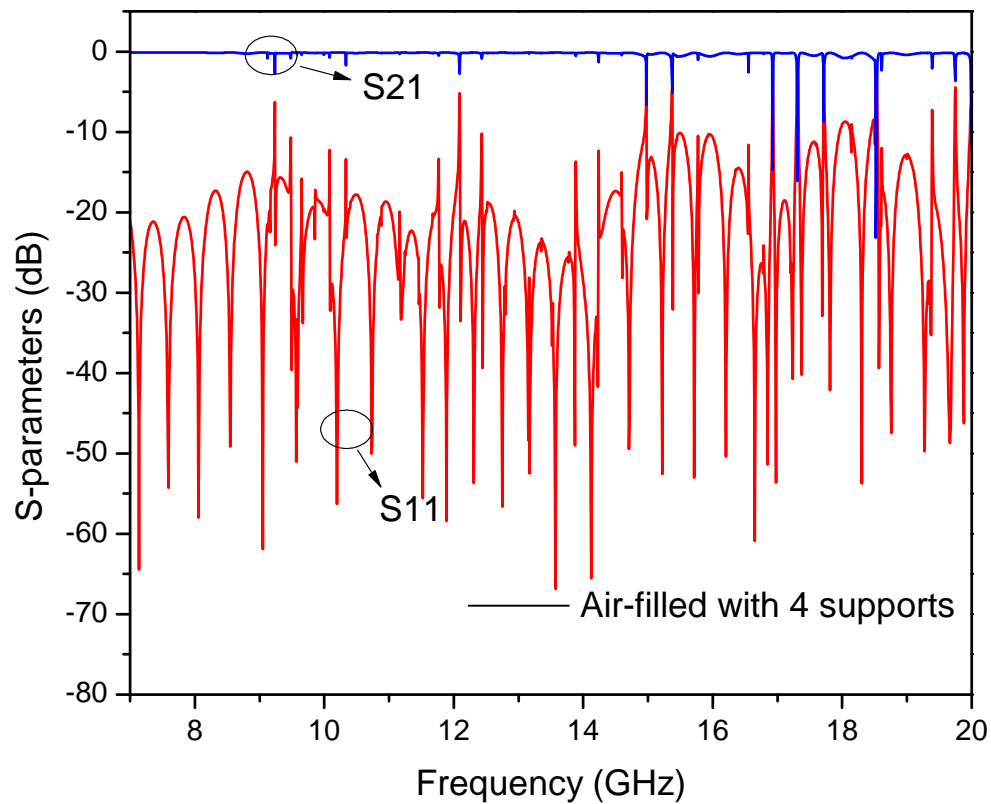
Fig. 3.24. Simulated S-parameters of the large electrical volume transmission line with 4 equally spaced dielectric supports as an demonstration of a wrong design. Resonances are generated by the coupling between TEM and TE_{41} modes.
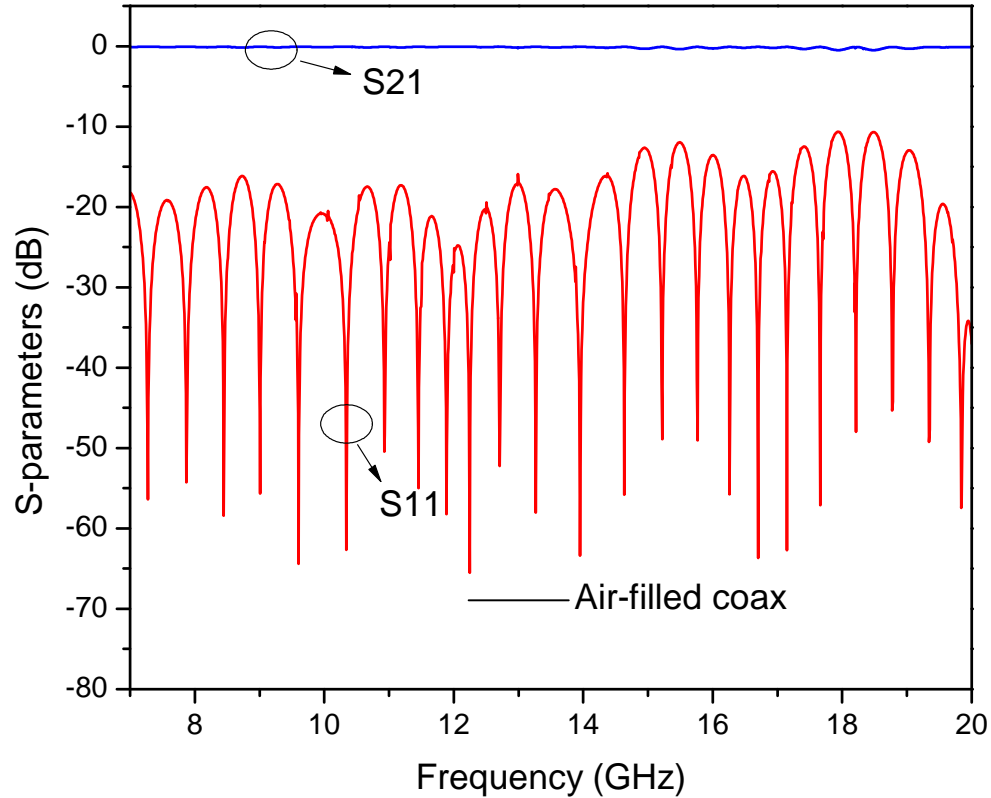
Fig. 3.25. Simulated S-parameters of the large electrical volume transmission line without dielectric supports.

3.3.2 Fabrication

Fabrication of the outer conductor is done by dividing the outer conductor in two halves along the longitudinal direction for a minimum effect in electrical performance as well as for ease of machining. The tapered inner conductor is fabricated by CNC lathing. Finally, the Delrin® posts, center conductor, and outer conductor are assembled to form one piece of large electrical volume coax.

The final design of the large electrical volume coaxial transmission line has 8 equally spaced dielectric supports at each end, as shown in Fig. 3.28(b), and the final length of the coax is 34.8 cm as shown in Fig. 3.28(c). Finally, measured and
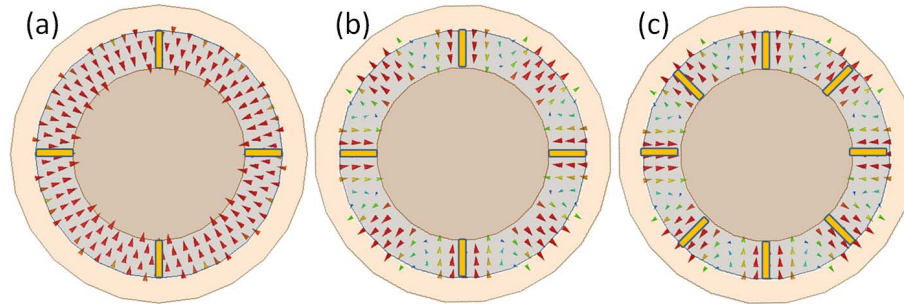
Fig. 3.26. Electric fields in the coax with dielectric supports. (a) TEM mode with 4 supports. (b) TE_{41} mode with 4 supports. (c) TE_{41} mode with 8 supports. In (b) the 4 evenly spaced dielectric supports align with common electric fields of the TE_{41} mode and cause resonances. In (c) with 8 evenly spaced dielectric supports, both common and differential electric field will align with the dielectric supports, and the total coupling between the TEM mode and TE_{41} mode can be eliminated.

simulated S-parameters of the final design with 8 dielectric supports are shown in Fig. 3.27.

3.3.3 Results

With the increase of total number of molecules in the large electrical volume coaxial transmission line, we have a stronger chemical signal. Therefore, by using the 1 μs excitation between 12.1 GHz to 12.5 GHz, the 12.178 GHz spectral line starts to become noticeable after 100 averages, as shown in the inset of Fig. 3.29. After 1,000 averages two clear spectral lines are found, and the signal-to-noise ratio of the 12.178 GHz spectral line becomes 22.6 dB after 1,000 averages.

3.4 Spectral Line Decay Study of Large Electrical Volume Transmission-line

We observed that signals in coaxial transmission line spectrometers tend to decay faster, and the signal in OMC decays faster than that in the LEVC. In order to
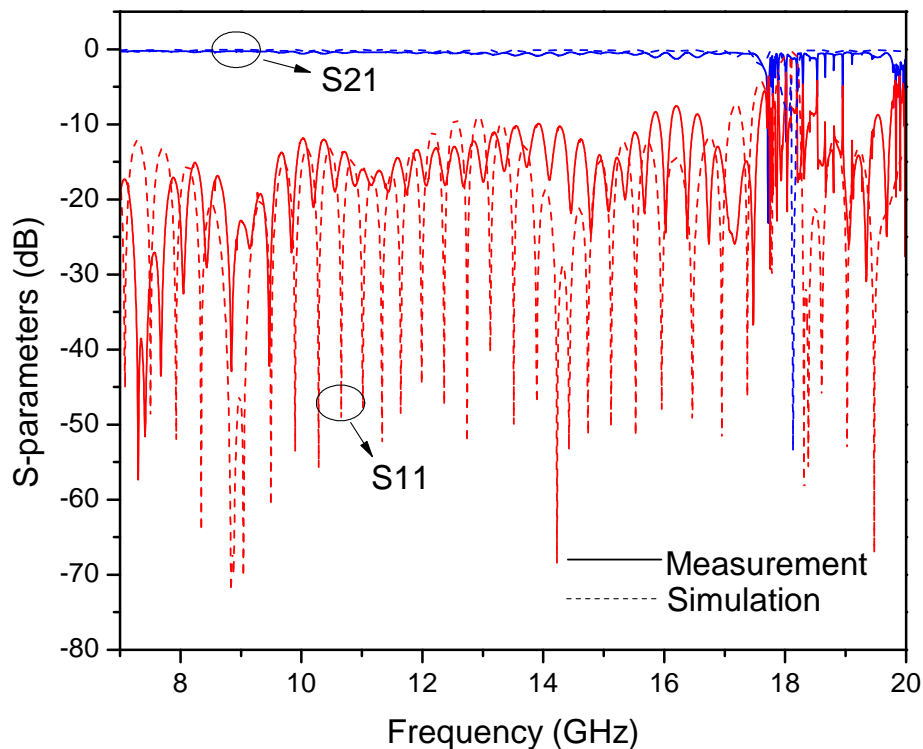
Fig. 3.27. Measured and simulated S-parameters of the LEVC transmission line. With the correct design of 8 equally spaced dielectric supports in the final design, S_{21} is smooth and resonance free in the passband up to 17.5 GHz.

study the dependance of decay of molecular signals to transmission line geometry and pressure, we performed a short-time Fourier transform to the the recorded FID, and the spectrogram of the signal at 17.7 mTorr is shown in Fig. 3.30 to show how methanol resonances decay with time. A molecule dynamics model that we have developed in order to predict signal decay in coaxial transmission line structures will be introduced, and subsequent measured and simulated results will be discussed in detail in this section.
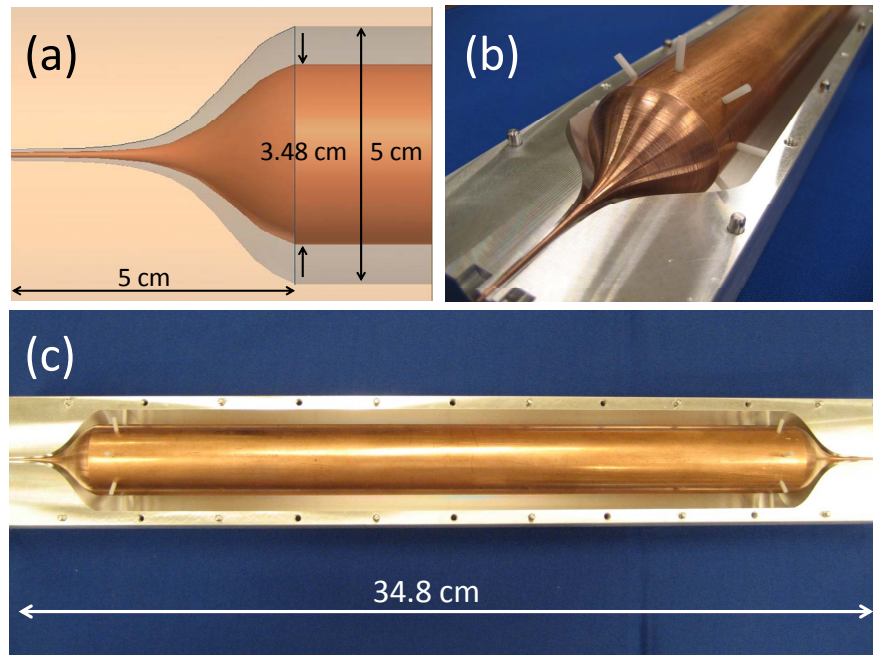
Fig. 3.28. (a) Side-view of the large electrical volume coaxial transmission line design. This figures shows the taper length of 5 cm, and the final dimensions of the outer and inner conductor radius are 2.5 cm and 1.74 cm. (b) Close-up view of the fabricated large electrical volume transmission line. This picture also shows 8 equally spacing dielectric supports which are designed to support the center conductor. (c) Assembly of the center conductor and half of the outer conductor, and the total length is 34.8 cm.

3.4.1   Molecule Dynamics Model

Re-emission signal level is the result of the amount of power that the ensemble dipole moment of molecules couples to the fundamental mode of the coaxial transmission line. This can be illustrated as shown in Fig. 3.31. In Fig. 3.31(a), at $t = 0$ the molecule highlighted with the black circle is polarized by the local electric field $E_{local}(r)$ and has a dipole moment of $dp = \alpha E_{local}(r)$. Therefore, at $t = 0$ the total power that couples to the coaxial fundamental mode can be found by integrating the power from all molecules, as described in Eq. (3.12), where σ, a, and b are the number
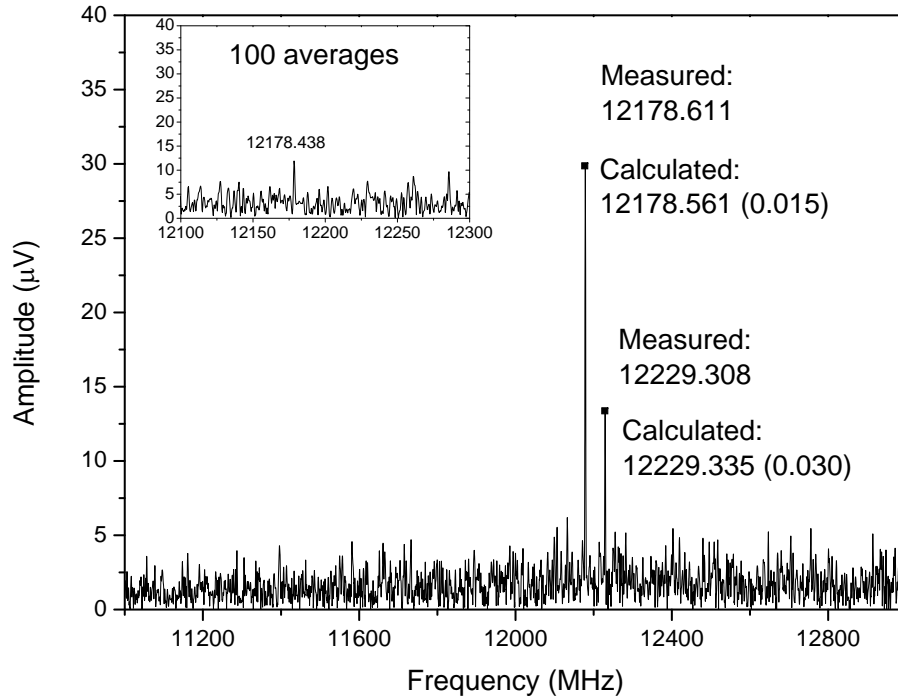
Fig. 3.29. Methanol spectrum of the $2_{0\ 2} \leftarrow 3_{-1\ 3}$ and $16_{5\ 12} \leftarrow 17_{4\ 13}$ transitions which are at 12.178 GHz and 12.229 GHz. This spectrogram is obtained by applying short-time Fourier transform to the 1,000-averaged spectrum. Inset shows the methanol spectrum after 100 averages. Measured and calculated frequencies are shown in the figure, and the calculation uncertainties are shown in parenthese [40].

density, inner radius, and outer radius respectively. In Fig. 3.31(b), at a later time when $t = t'$ the molecule highlighted with the black circle travels to a new location r' where its dipole moment dp is misaligned with the local electric field $E_{local}(r')$. Hence, power coupling from this molecule to the coaxial transmission line is reduced due to the misalignment angle $\theta(t')$ and the weaker local electric field strength. The total power coupled from molecules to the coaxial transmission line can then described by Eq. (3.13).
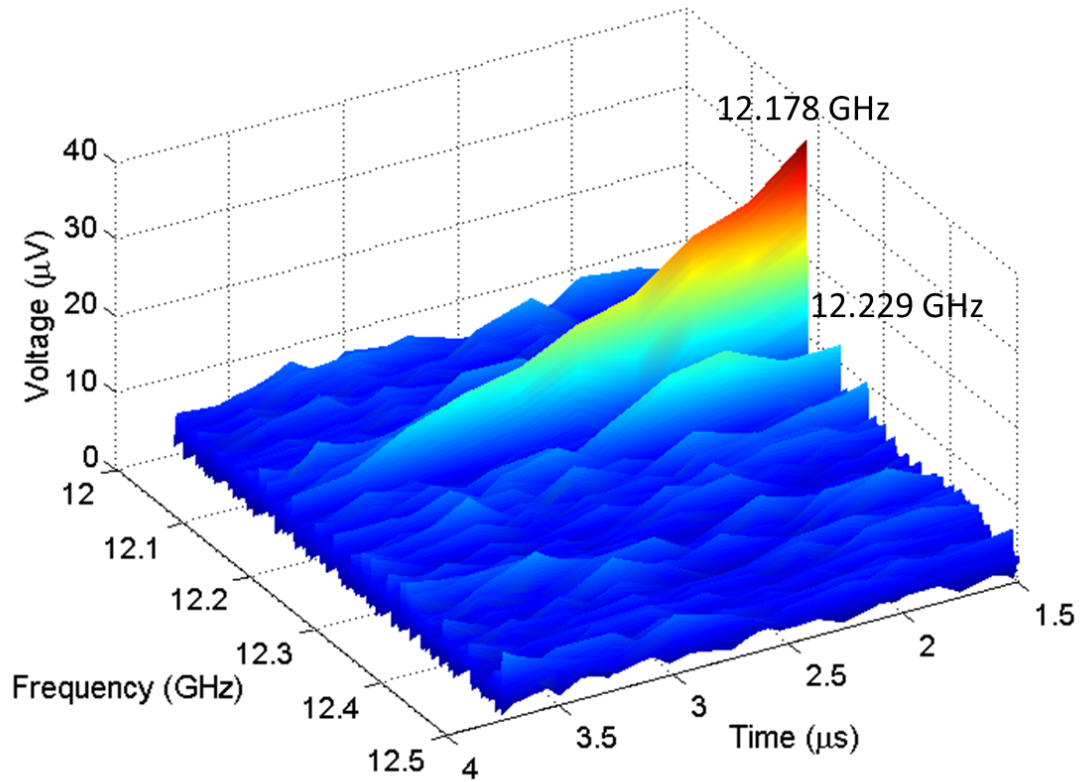
Fig. 3.30. Spectrogram of the $2_{0\ 2} \leftarrow 3_{-1\ 3}$ and $16_{5\ 12} \leftarrow 17_{4\ 13}$ transitions which are at 12.178 GHz and 12.229 GHz. This spectrogram is obtained by applying short-time Fourier transform to the 1,000-averaged spectrum.

$$U\left(t=0\right) \propto \int_a^b \int_0^{2\pi} \left(\frac{V_0}{\ln b/a}\frac{1}{r} \cdot \alpha \frac{V_0}{\ln b/a}\frac{1}{r} \right)^2 \sigma \cdot r dr d\theta \tag{3.12}$$

$$U\left(t'\right) \propto \int_a^b \int_0^{2\pi} \left(\frac{V_0}{\ln b/a}\frac{1}{r'} \cdot \alpha \frac{V_0}{\ln b/a}\frac{1}{r} \cos\theta\left(t'\right) \right)^2 \sigma \cdot r dr d\theta \tag{3.13}$$

$$\theta\left(t'\right) = \cos^{-1} \frac{r'}{\sqrt{\left(r + v_r t'\right)^2 + \left(v_\theta t'\right)^2}} \tag{3.14}$$

Furthermore, in order to account for the wall-collision effect, we have divided the cross-section of the coaxial transmission line into 3 sections with time-varying boundaries S_1 and S_2, as shown in Fig. 3.32. Molecules in each region in Fig. 3.32 move in random directions: half of the molecules have a radial velocity of $v_r > 0$ and half of the molecules have a radial velocity of $v_r < 0$ in each section. In section I molecules with $v_r < 0$ will collide with the center conductor wall and result in loss of energy and coherency, and therefore we only consider molecules with $v_r > 0$ in region I. Likewise, we only consider molecules with $v_r < 0$ in region III because molecules with $v_r > 0$ will collide with the outer conductor wall. On the contrary, molecules with $v_r > 0$ and $v_r < 0$ in region II could travel without wall collisions, and hence all molecules in region II are considered.

With the wall-collision consideration and Eqs. (3.12) and (3.13), the normalized geometry-dependent power decay of re-emission signals in two different coaxial transmission line structures is shown in Fig. 3.33(a). However, signal also decays exponentially with its polarization dephasing time T_2 [36]. Fig. 3.33(b) shows the signal decay in coaxial structures with the exponential decay term, $\text{Exp}\,(-2t/T_2)$, included with $T_2 = 0.9\ \mu s$ as an example.

3.4.2 Results

In the molecular dynamics model, because methanol has a mass of 32 a.m.u., methanol molecules have root-mean-square velocity of $v_{rms} = 445$ m/s at room-temperature, and therefore the rms value of the radial speed is $v_r = 257$ m/s at room-temperature. In addition, with least-square fitting, we have found that the T_2 is ~ 0.12 times the mean collision time, where the mean collision time is pressure dependent and can be calculated using kinetic theory [43], [44].

The normalized power decay of the 12.178 GHz spectral line in the large electrical volume coax is shown in Fig. 3.34. This figure shows the measured normalized power decay at 3 different pressure conditions, and the solid-lines are the predicted

normalized power decay. Power decay in the overmoded coaxial transmission line is also studied, as shown in Fig. 3.35. Measured data and predicted decay curves are in good agreement in both coaxial transmission line designs.

3.5   Conclusion

Microwave spectroscopy has the potential for use as a chemical sensor because its kHz resolution accuracy allows for precision determination of shape/structure and therefore tracking back to chemical specificity. The significant advances in the introduction of FTMW and CP-FTMW spectroscopy add benefits to the detection sensitivity and the capability of broadband measurement within a short period of time. In addition, the complexity of the instrumentation at the microwave frequencies is continually being reduced by advances in circuit technology. In this chapter, we further demonstrated microwave chemical sensing at room temperature using an overmoded waveguide and expanded the operational bandwidth with an overmoded coaxial cable and a large electrical volume coaxial cable. These designs performs high accuracy measurement, only requires a relatively small amount of excitation power, and are compact microwave spectrometer designs that proves the future possibility of a portable microwave chemical sensor design. The capability of conducting overmoded transmission line room-temperature measurements also simplifies the spectrometer design because the cooling mechanism, e.g. pulse valve for supersonic expansion, is excluded, and the vacuum pump requirement is also relaxed.

In the designs of coaxial cable spectrometers, we demonstrated a method to provide smooth transitions in changing coaxial transmission line dimensions, and the first OMC and LEVC transmission line design and its application in microwave chemical sensing is introduced in this chapter. Mode coupling issues between the TEM mode and the TM_{01} mode can be avoided with correct design, and we also show a way to practically support the center conductor and eliminate the coupling between the TEM and the TE_{41} modes to achieve a wideband operation.

With this new LEVC transmission line microwave spectrometer and a 1 μs chirped pulse between 12.1 GHz to 12.5 GHz, we observed two methanol spectral lines at 12.178 GHz and 12.229 GHz, which correspond to the $2_{0\ 2} \leftarrow 3_{-1\ 3}$ and $16_{5\ 12} \leftarrow 17_{4\ 13}$ transitions, respectively. The capability of detecting the 12.229 GHz spectral line is exclusive in RT-CP-FTMW spectroscopy because it is related to the higher rotational state transition, $16_{5\ 12} \leftarrow 17_{4\ 13}$, which can not be resolved in low-temperature spectroscopy. Fast detection is also achieved when the 12.178 GHz spectral line becomes prominent after taking 100 averages, and finally in the 1,000-averaged spectrum the 12.178 GHz line has an 8 dB improvement in SNR compared to the overmoded coaxial transmission line spectrometer with the same number of averages.

The molecule dynamics model is in very good agreement with the measurement from the LEVC transmission line spectrometer as well as from the OMC transmission line spectrometer. The molecule dynamics model also predicts that a much lower spectrum decay rate in the LEVC transmission line spectrometer can be achieved in the future if we use enough molecules to operate at a lower pressure, as shown in Fig 3.35, and larger inner conductor and outer conductor radii are preferable for slower signal decay. Furthermore, this model also predicts that at 5 mTorr molecules could travel $\sim$1 mm within the dephasing T_2 time without wall collision. A coaxial transmission line spectrometer with an inner and outer conductor distance of 1 mm that could operate at $\sim$150 GHz without mode coupling issues can be expected in the future. Utilization of high frequency operation will have the benefit of strong spectral lines because molecular re-emission strength is proportional to frequency [35], and hence an even faster detection can be achieved in the future.
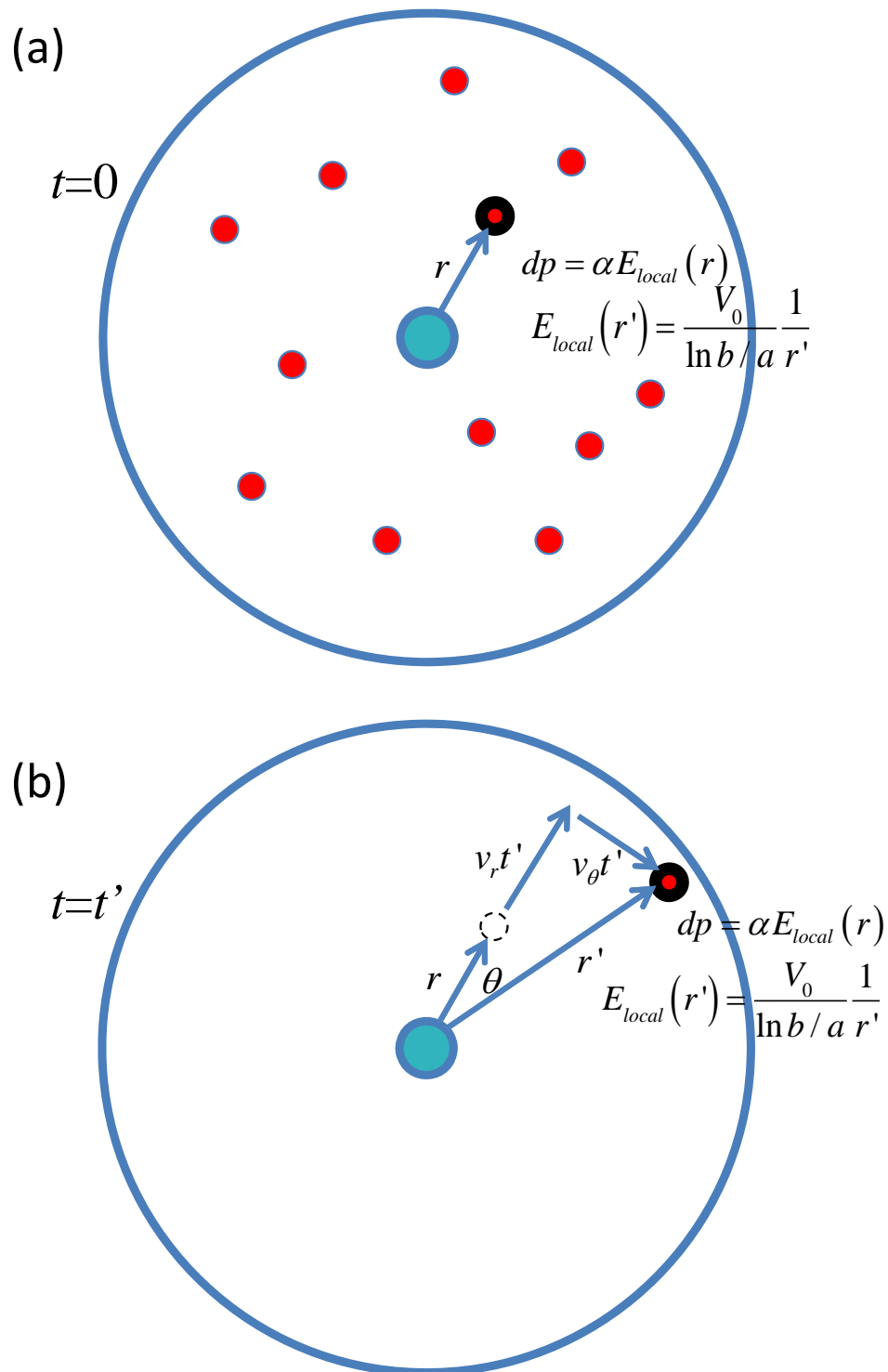
Fig. 3.31. (a) Molecules with random distribution at $t = 0$ are shown. The molecule highlighted with the black circle is polarized by the local electric field $E_{local}(r)$. (b) At $t = t'$ the highlighted molecule travels to the new location r' with a radial displacement $v_r t'$ and lateral displacement $v_\theta t'$. Energy coupling from this molecule to the coax changes because of the polarization mismatch and local field change.
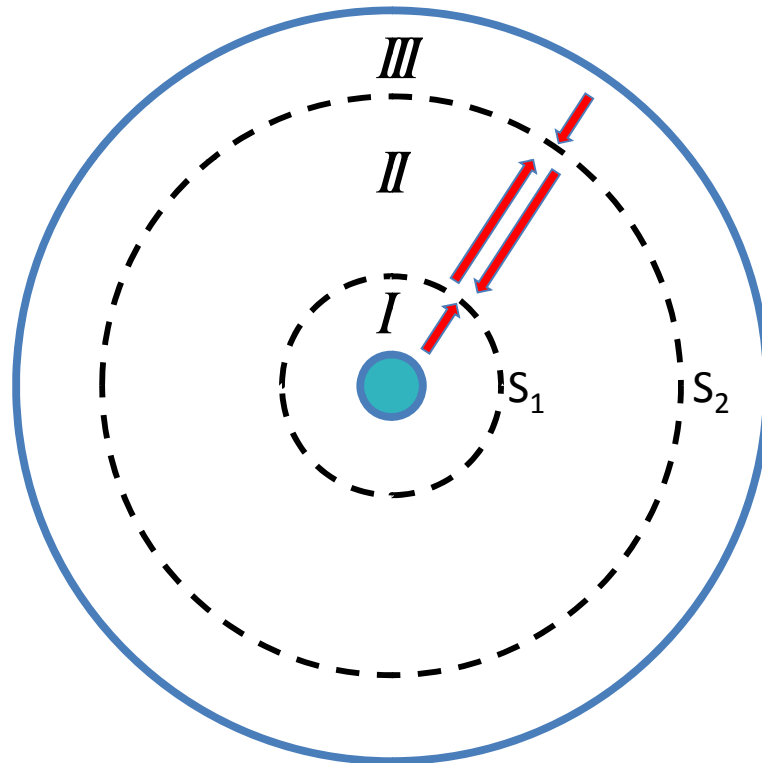
Fig. 3.32. Cross section of the coaxial transmission line is divided into three sections in order to calculate the detectable power using the molecule dynamics model. In region *I*, molecules with $v_r > 0$ are considered, in region *II* molecules with both $v_r > 0$ and $v_r < 0$ are considered, and in region *III* molecules with $v_r < 0$ are considered. The two boundaries S_1 and S_2 are set by $a + v_r t$ and $b - v_r t$ respectively, where a and b are the inner and outer radius, and v_r is the radial velocity.
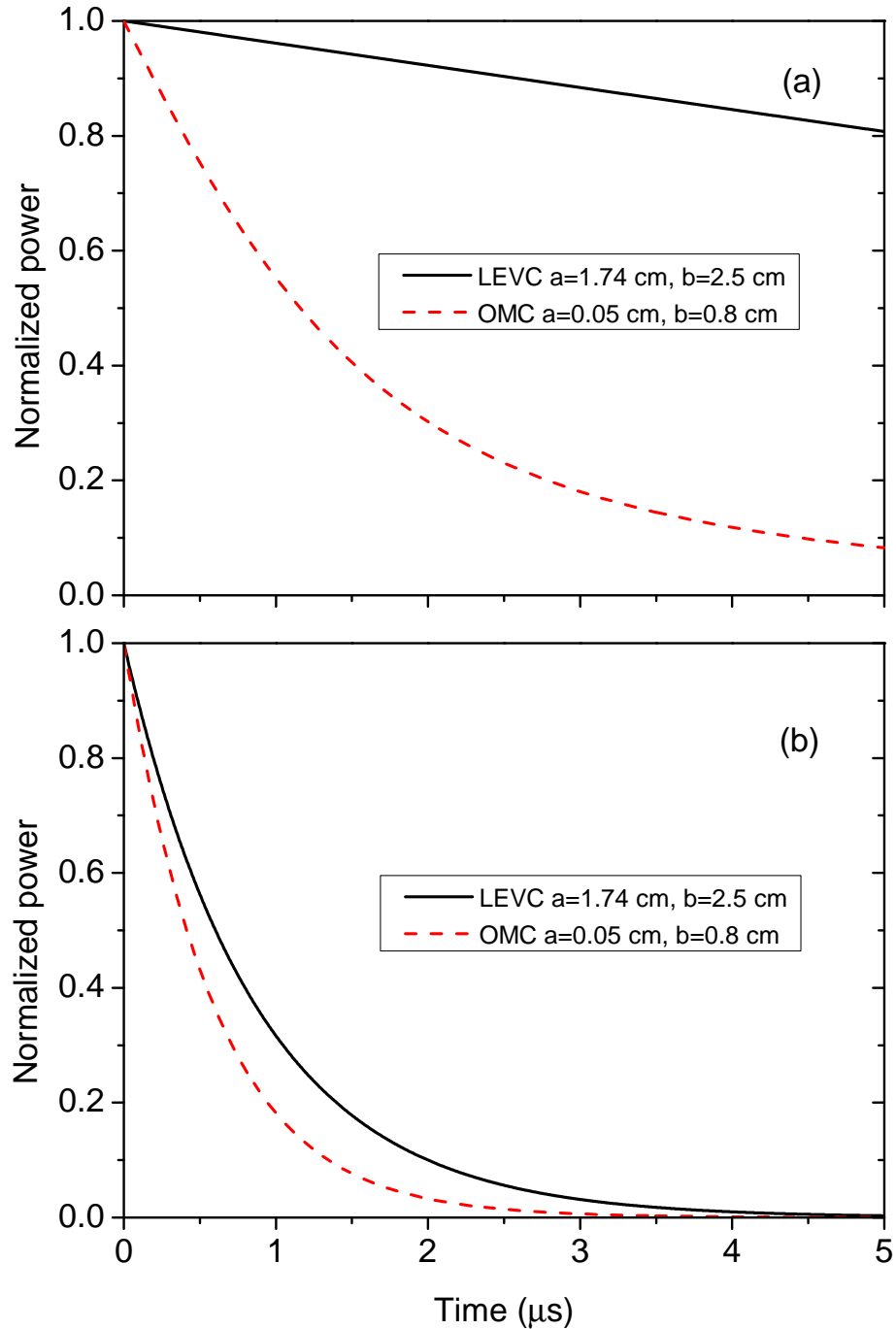
Fig. 3.33. (a) Geometry-dependent signal decay in two coaxial transmission lines. The large electrical volume coax has a radius of 1.74 cm in inner conductor and 2.5 cm in outer conductor, and the overmoded coax has a radius of 0.05 cm in inner conductor and 0.8 cm in outer conductor. It can be seen in this figure that without the pressure-dependent T_2 exponential decay, the large electrical volume coaxial transmission line exhibits a slower signal decay rate. (b) Signal decay when a polarization dephasing time $T_2 = 0.9 \ \mu s$ is accounted for in Eq. (3.13). It can be seen in this figure the pressure-dependent exponential decay dominates the spectrum decay behavior.
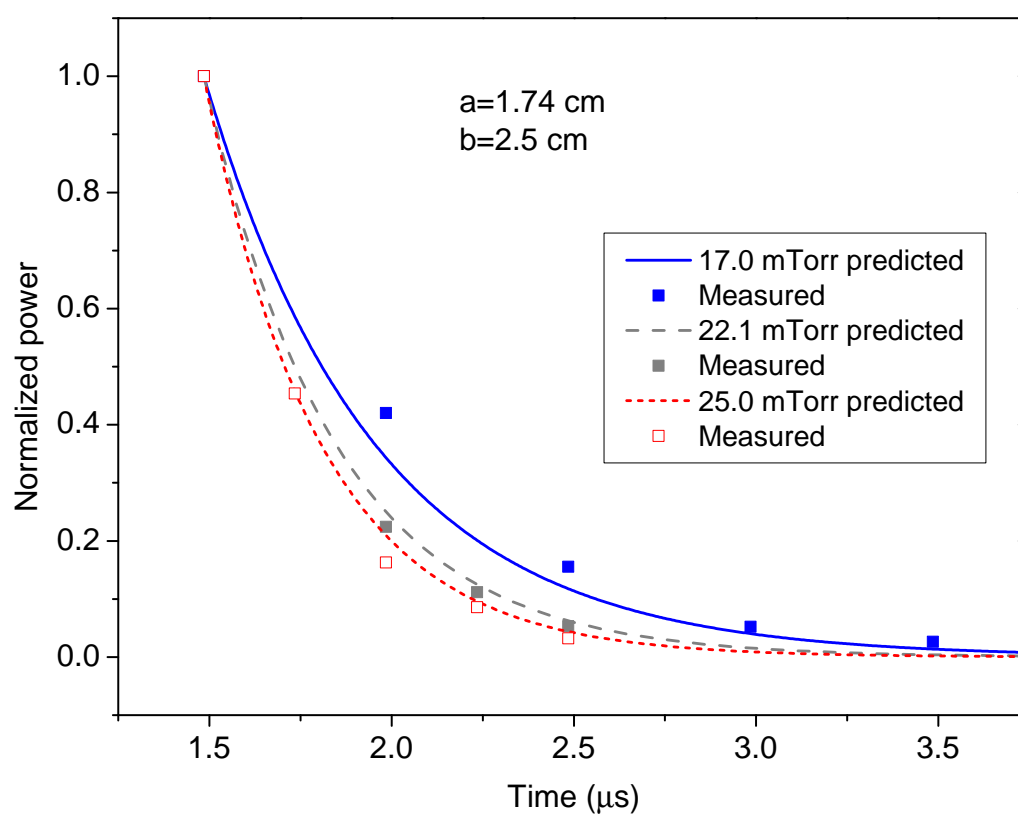
Fig. 3.34. Measured and predicted pressure-dependent signal decay of the 12.178 GHz spectral line in the large electrical volume coaxial cable that has outer conductor radius of 2.5 cm and inner conductor radius of 1.74 cm. Signal decays faster as pressure increases because self-collision among molecules are more frequent.
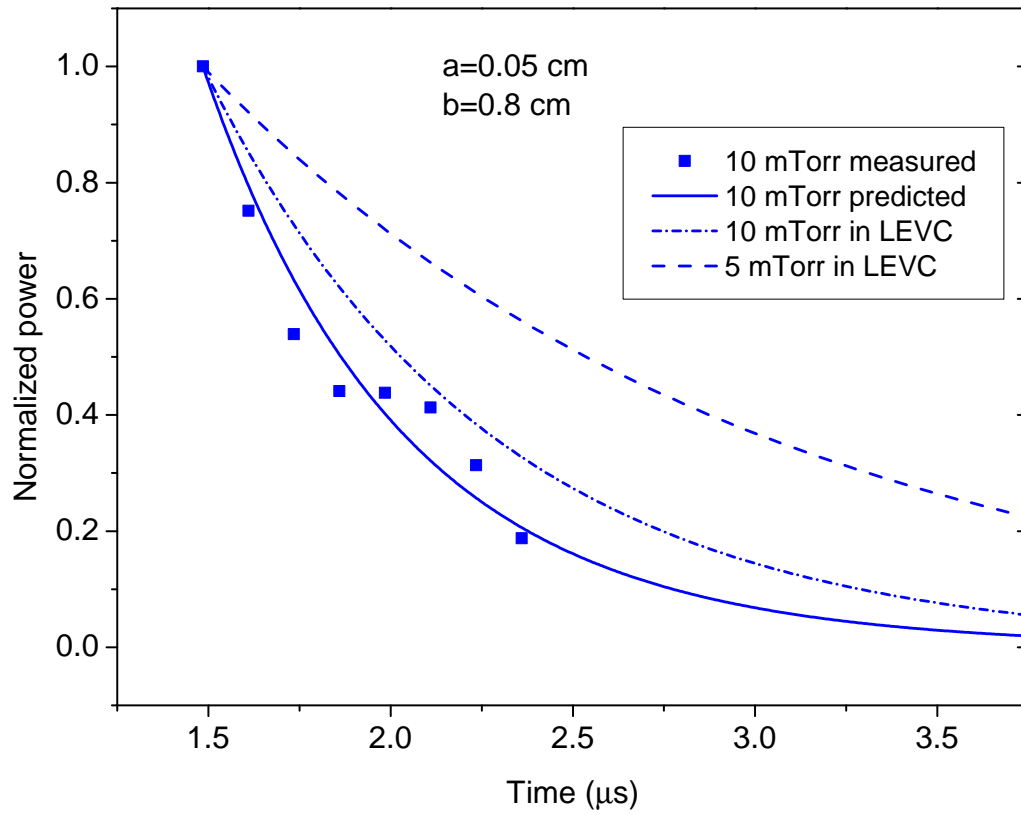
Fig. 3.35. Measured and predicted pressure-dependent signal decay of the 12.178 GHz spectral line in the overmoded coaxial cable that has outer conductor radius of 0.8 cm and inner conductor radius of 0.05 cm at 10 mTorr. Prediction of the spectral line decay in the LEVC at 10 mTorr is also shown in the figure for comparison. It can be seen in the figure that the LEVC shows a slower decay rate than the OMC, and the difference becomes more significant when the LEVC is operated at 5 mTorr.

4. ADVANCED DIGITIZATION AND LOW POWER EXCITATION

We have demonstrated compact transmission line designs in Chapter 3 that can be integrated as a compact spectrometer. In this chapter, we will pursue a spectrometer system with low input power using the LEVC and exploit the advantage of fast coherent averaging of the new digitizer, Guzik ADC6131.

This new digitizer has a sample rate of 40 Gs/s sampling and an analog bandwidth of 13 GHz. In the core of the digitizer are four FPGAs, and the Guzik ADC6131 can be programmed to perform onboard digital signal processing such as signal averaging and FFT with up to 10 Gs/s processing speed. At the full sampling speed, we are able to perform 1 million averages of a 10 μs signal segment in 20 seconds. Two advantages using this fast digitizer are (1) with the same input power and start detection time, SNR increases as number of averages increases (2) the input power can be reduced to achieve a desired SNR that serves as detection threshold.

We will also show in this chapter that with a fixed number of averages SNR will decrease as the input power decreases. In addition, in the experiment setup shown in previous chapters we waited 1 μs after the excitation pulse ends and before we started to record the FID, and therefore we lose significant signal strength during the 1 μs wait because molecular signals decay exponentially. In order to compensate loss of SNR with low input power, we also pursue early start detection time. More details will be given in the following sections.

The schematic of the system that we use in this chapter is shown in Fig. 4.1. An excitation pulse is generated by an arbitrary waveform generator (Tektronix AWG 7101). The output waveform of the arbitrary waveform generator is then upconverted to a higher frequency band by using a frequency multiplier. The excitation pulse is then amplified and sent into the analysis cell to excite the enclosed chemical species.

In the receiver circuit, we use an LNA (Miteq AMF-6F-06001800-15-10P) to amplify the weak molecular signal, and a PIN diode limiter (Advanced Control Components ACLM-4619FC361K) and a solid-state switch (ATM PNR S1517D) are used to protect the LNA. The whole system is synchronized with a 10 MHz rubidium frequency standard (Stanford Research Systems SF725). The solid-state switch power amplifier are controlled by a timing unit (Stanford Research Systems DG535), and the Guzik digitizer is triggered by one of the arbitrary waveform generator's output channel.
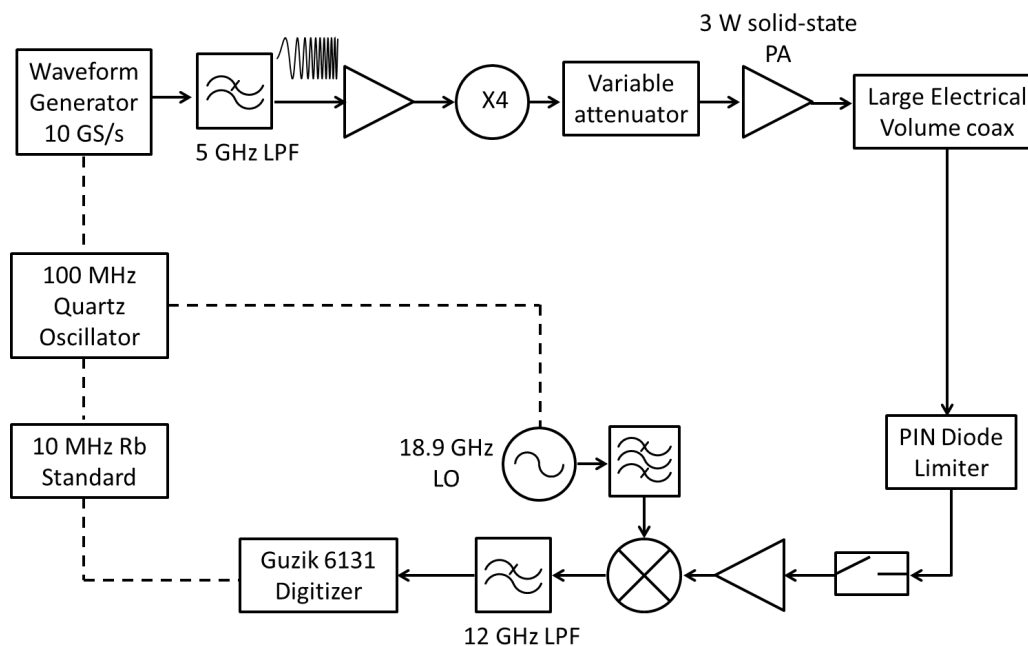
Fig. 4.1. Schematic for the experiment setup using the new Guzik 6131 real-time digitizer. The LEVC is used as analysis cell in this chapter.

4.1 Increase of Signal to Noise Ratio

In the receiver of our microwave spectrometer system, we have used the coherent averaging technique to recover the molecular signal embedded in noise. Coherent averaging requires the system to be synchronized such that every collected data set

has the same phase. The waveform of the embedded signal will then average to its true amplitude value, and the uncorrelated noise will average towards zero [45]. With N number of averages, the coherent SNR gain is $\sqrt{N}$ and is $10 \text{Log} N$ dB.

4.2 Reduced Excitation Power Requirement

In this section we try to characterize our current system with low excitation power. Because the $16_{5\ 12} \leftarrow 17_{4\ 13}$ transition (12.229 GHz) exhibits very strong signal and the excitation power will be reduced to as low as -13 dBm, we use a 1 μs excitation between 12.228 GHz and 12.230 GHz to focus the spectral power density to excite this transition only. Number of averages is set to 1 million, and the pressure condition is set at 20 mTorr to eliminate all other variables.

The re-emission signal strength following a chirped pulse excitation has the form [35], [46]

$$V \propto \omega \mu^2 E_{pulse} \Delta N_0 \left(\frac{\pi}{\alpha}\right)^{1/2} \tag{4.1}$$

where

$$
\begin{aligned}
&\mu = \text{transition dipole moment,} \\
&E_{pulse} = \text{electric field strength} \propto \sqrt{\text{input power}}, \\
&\Delta N_0 = \text{population difference,} \\
&\alpha = \text{sweep rate.}
\end{aligned}
\tag{4.2}
$$

Fig. 4.2 shows the measured amplitude of the $16_{5\ 12} \leftarrow 17_{4\ 13}$ transition (12.229 GHz). As we can see from the figure, for square-root of input power less than 7.08 mW$^{1/2}$ (17 dBm input), signal strength is linearly proportional to the electric field strength. With 1 million coherent averages, noise amplitude standard deviation (σ_{rms}) is 0.2 μV in the vicinity of 12.229 GHz spectral line, and Fig. 4.3 shows the SNR versus input power. In the linear region, results in Figs. 4.2 and 4.3 are consistent with Eq. (4.1).

Figs. 4.2 and 4.3 also indicate that saturation occurs when input power is greater than 17 dBm. Therefore, for input power greater than 17 dBm the spectrometer should be designed to probe a wider bandwidth or execute a faster frequency sweep in order to utilize the power spectral density efficiently.
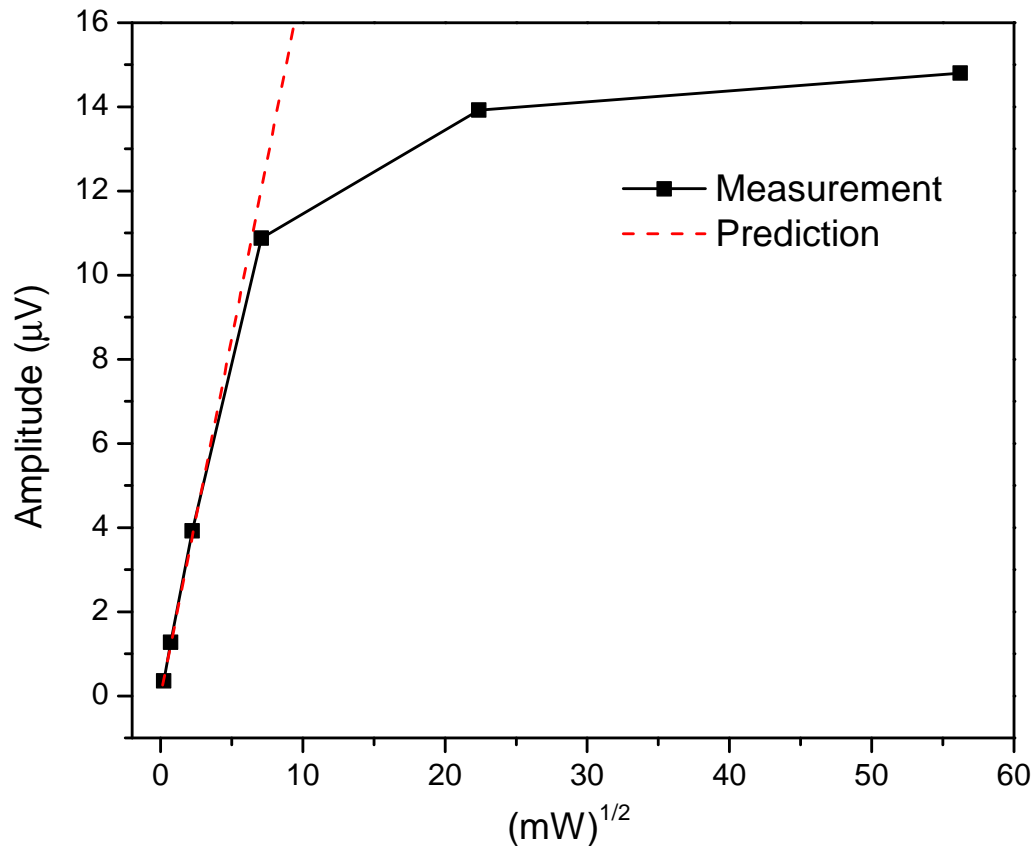
Fig. 4.2. Measured and predicted 12.229 GHz signal strength versus (input power)$^{1/2}$. This figure shows that before square-root of input power reaches the saturation point, 7.08 mW$^{1/2}$, the measured signal strength is linearly proportional to the square-root of input power, as predicted in Eq. (4.1).

4.3 Early Detection Time with Low Power Excitation

In the previous chapter, we have characterized molecular signal decay feature in the large electrical volume coaxial transmission line. Dephasing time, T_2 is found
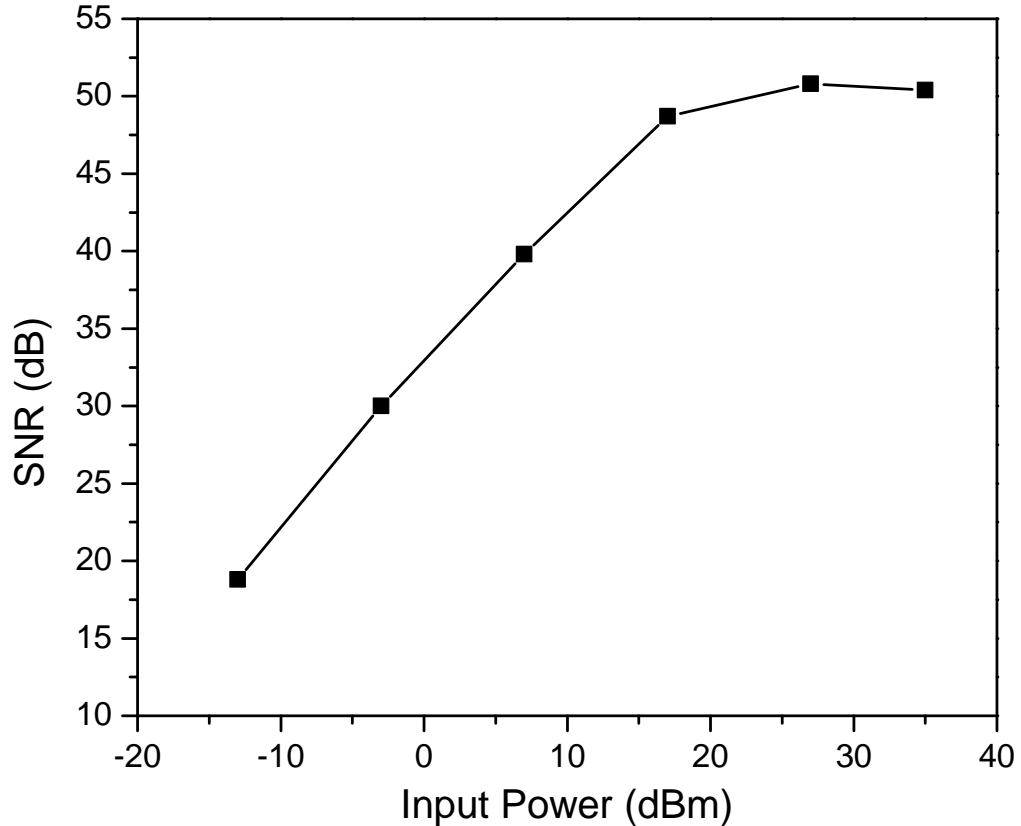
Fig. 4.3. Measured SNR (dB scale) of the 12.229 GHz signal under various input power. Before the input power reaches 17 dBm, the measured SNR versus input power follows a straight line with a slope equal to unity. This result shows that SNR increase linearly as input power increases and is consistent with Eq. (4.1).

approximately equal to 0.12 times mean collision time, and this exponential decay factor will dominates the signal decay feature at an operation pressure of 20 mTorr. In this section, we will derive an approximate analytical form of signal strength by using Fourier series and by assuming the molecular signal resembles a damped sinusoidal wave.

A periodic function can be represented by a Fourier series [47]

$$f(t) = a_0 + \sum_{n=1}^{\infty} a_n \cos(n\omega_0 t) + \sum_{n=1}^{\infty} b_n \sin(n\omega_0 t), \qquad (4.3)$$

where ω_0 is the fundamental frequency, a_0 is the amplitude of the DC component, a_n and b_n are the Fourier coefficients that represents the amplitude of the corresponding sine and cosine waves. The Fourier coefficients can be found by using

$$a_0 = \frac{1}{T} \int_{t_0}^{t_0+T} f(t)\, dt, \tag{4.4}$$

$$a_k = \frac{2}{T} \int_{t_0}^{t_0+T} f(t) \cos(k\omega_0 t)\, dt, \tag{4.5}$$

$$b_k = \frac{2}{T} \int_{t_0}^{t_0+T} f(t) \sin(k\omega_0 t)\, dt. \tag{4.6}$$

When the periodic function has an damped profile dominated by an exponential profile, it is represented as

$$e^{-t/\tau} f(t) = a_0' + \sum_{n=1}^{\infty} a_n' \cos(n\omega_0 t) + \sum_{n=1}^{\infty} b_n' \sin(n\omega_0 t), \tag{4.7}$$

where τ is the decay time-constant of the damped profile. We can then define the Fourier coefficients as

$$a_0' = \frac{1}{T} \int_{t_0}^{t_0+T} e^{-t/\tau} f(t)\, dt, \tag{4.8}$$

$$a_n' = \frac{2}{T} \int_{t_0}^{t_0+T} e^{-t/\tau} f(t) \cos(k\omega_0 t)\, dt, \tag{4.9}$$

$$b_n' = \frac{2}{T} \int_{t_0}^{t_0+T} e^{-t/\tau} f(t) \sin(k\omega_0 t)\, dt. \tag{4.10}$$

If $f(t)$ is a k-th harmonic of the fundamental frequency, $f(t) = \cos(k\omega_0 t)$, then

$$\begin{aligned} a_k' &= \frac{2}{T} \int_{t_0}^{t_0+T} e^{-t/\tau} \cos(k\omega_0 t) \cos(k\omega_0 t)\, dt \\ &= \frac{2}{T} \int_{t_0}^{t_0+T} e^{-t/\tau} \frac{1 + \cos(2k\omega_0 t)}{2} dt \\ &\approx \frac{1}{T} \int_{t_0}^{t_0+T} e^{-t/\tau} dt \quad \left(\text{assuming } \tau \gg \frac{k\omega_0}{2\pi} \right), \end{aligned} \tag{4.11}$$

$$\begin{aligned} b_k' &= \frac{1}{T} \int_{t_0}^{t_0+T} e^{-t/\tau} \cos(k\omega_0 t) \sin(k\omega_0 t)\, dt \\ &\approx 0 \quad \left(\text{assuming } \tau \gg \frac{k\omega_0}{2\pi} \right). \end{aligned} \tag{4.12}$$

We can then use the k-th harmonic to represent the molecular resonance and predict the signal strength from the above equations without loss of generality: the molecular resonance we are working on are between 8 GHz to 18 GHz and has a period on the order of 0.1 ns whereas the time-constant of the damped profile is on the order of several hundred μs (τ is therefore several thousand times of molecular resonance period). Eq. (4.11) also implies that the Fourier coefficient is the time-averaged amplitude of the damped profile. Therefore, this is a very useful expression because it can be used to predict spectral component of a spectrum.

From Eq. (4.11) the signal strength of a damped sinusoidal waveform can by expressed as

$$
\begin{aligned}
X &= A\left(t_1\right) \frac{1}{T} \int_{t_1}^{t_1+T} \exp\left(\frac{-(t-t_1)}{\tau}\right) dt \\
&= A_0 e^{-t_1/\tau} \frac{\tau}{T}\left(1 - e^{-T/\tau}\right)
\end{aligned}
\tag{4.13}
$$

where

$$
\begin{aligned}
A_0 &= \text{initial amplitude after excitation} \propto \sqrt{\text{input power}} \\
t_1 &= \text{start detection time} \\
\tau &= \text{decay time}-\text{constant} \propto \frac{1}{\text{pressure}} \\
T &= \text{recorded (gated) data length.}
\end{aligned}
\tag{4.14}
$$

Eq. (4.13) provides the basis so that we can predict signal strength at different start detection time and gate length without finding the exact number of A_0. For example, under the same pressure condition and excitation power, the spectral line amplitude at different start detection time t_1 and t_2 satisfies the following equation

$$
\frac{X_2}{X_1} = \frac{A_0 e^{-t_2/\tau}}{A_0 e^{-t_1/\tau}}.
\tag{4.15}
$$

We can also predict the signal strength at different input power, and it will satisfy the following equation

$$
\frac{X_2}{X_1} = \frac{A_{02} e^{-t/\tau}}{A_{01} e^{-t/\tau}} = \frac{\sqrt{P_2}}{\sqrt{P_1}},
\tag{4.16}
$$

where P_1 and P_2 are different input power.

Fig. 4.4 shows the predicted signal strength of the methanol $16_{5\ 12} \leftarrow 17_{4\ 13}$ transition by using Eq. (4.15). We use the measured signal strength at 17 dBm and 1 μs start detection time as reference point to predict the signal strength at different start detection times. This figure also shows signal strength of different input power predicted by Eq. (4.16). The measured spectrum using -3 dBm input at zero start detection time is shown in Fig. 4.5 as an example of the acquired spectrum and spectral line amplitude.
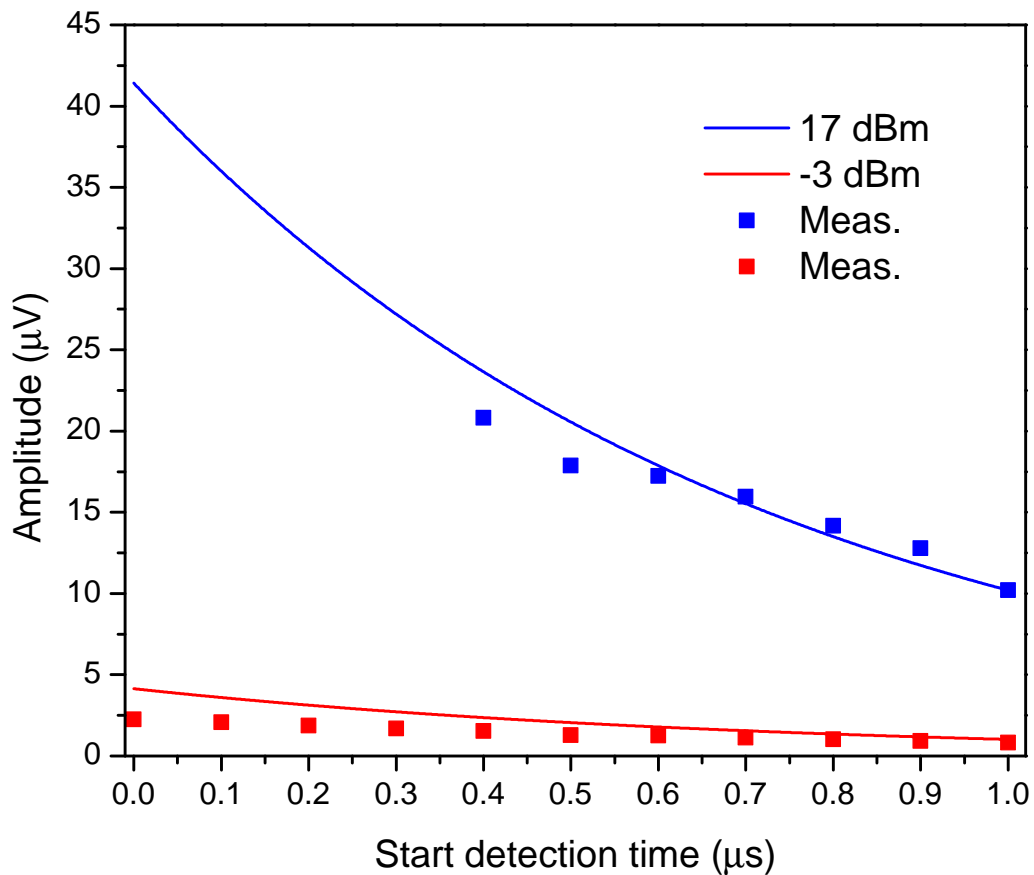
Fig. 4.4. Measured and predicted signal strength versus start detection time after input pulse ends. This figure shows to sets of data: 17 dBm input and -3 dBm input. For the same input power, Eq. (4.15) to predict the signal strength versus different start time. For different input power, Eq. (4.16) is used to predict the signal strength versus different start time.
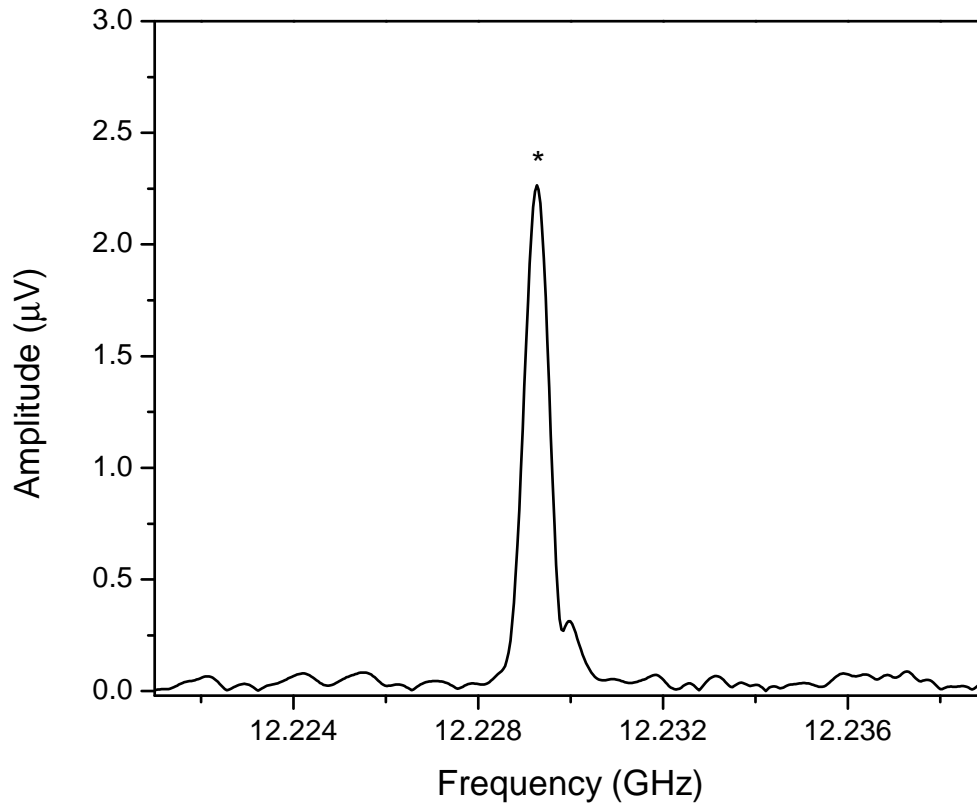
Fig. 4.5. Measured spectrum at -3 dBm input and with start detection time at zero μs. The asterisk mark indicates the 12.229 GHz spectral line of methanol.

4.4 Conclusion

In this chapter, we successfully demonstrated starting the detection range simultaneously with the end of the transmit pulse. In addition, the analytical equation shown in Eq. (4.13) provides a good basis to predict signal strength and SNR, and Figs. 4.4 and 4.6 show good agreement in prediction and measurement. The measurement results in Fig. 4.6 shows that a low input power of -3 dBm still provides an SNR of 35 dB. If our desired detection threshold is set to a 10 dB SNR, the input power can be as low as -28 dBm. These numbers are based on 1 million signal averages, and of course a lower input power can be expected with a tradeoff increase

of number of averages. A -34 dBm input power can be used to acquire the same SNR if we increase the number of averages to 4 million, and the detection time will be 80 seconds. The Guzik digitizer proves the path of a real-time portable microwave chemical sensor and the required input power can be reduced with with an increase of number of averages. Future ADC improvements will lead to a faster and wider bandwidth microwave chemical sensor that perform digital signal processing in the hardware level that will greatly increase the detection speed.
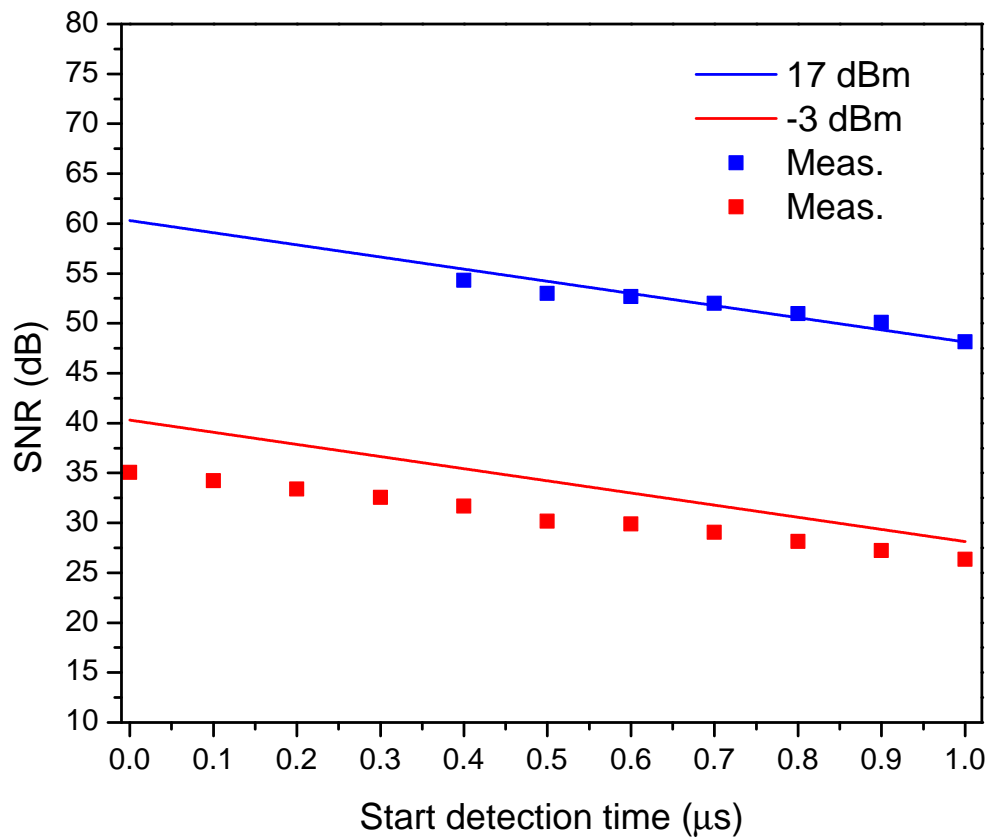
Fig. 4.6. Measured and predicted SNR of the 12.229 GHz signal. In this figure, results in Fig. 4.4 is used to calculate the SNR.

5. SIMULTANEOUS TRANSMIT AND RECEIVE WITH ABSORPTIVE BANDSTOP FILTERS

We have demonstrated detection of methanol in Chapter 4 by using a -3 dBm power input and showed that the SNR can be increased with an early detection time. In addition, with such a low input power we only detect one methanol resonance at a time. By using the experiment setup described in Chapter 4, each acquired FID segment is 10 μs long, the spectrometer has to wait for the digitizer to finish 1 million data acquisition, which takes about 20 seconds, before it uses the same low input power to excite and detect another methanol resonance.

The total detection speed of detecting multiple resonances for chemical identification can be increased if the the spectrometer utilizes the total 10 μs time during each data acquisition and continue to excite resonances at different frequencies while we are integrating data segments providing the excitation pulse can be properly isolated from the weak molecular signal and that the LNA is protected from saturation or damage. This simultaneous transmit and receive (STAR) mechanism is shown in Figs. 5.1 and 5.3 for ease of visualization.

STAR can be achieved by using a bank of bandstop filters in which one filter will be turned on and tuned to the same frequency as the transmitting pulse, as shown in Fig. 5.3. Specifically, absorptive bandstop filters (ABSF) will be useful in a spectrometer because they not only isolate transmit power but also reduce the transient response. As opposed to a reflective-type bandstop filter, an ABSF also has the advantages of achieving high isolation with relaxed resonator Q requirements [48]. Fig. 5.2 shows one tunable ABSF solution where the resonators are tuned by varactors. In this design, coupling between each resonator and the transmission line is fixed, which limits the tuning range of the ABSF. However, a wideband filter bank can be
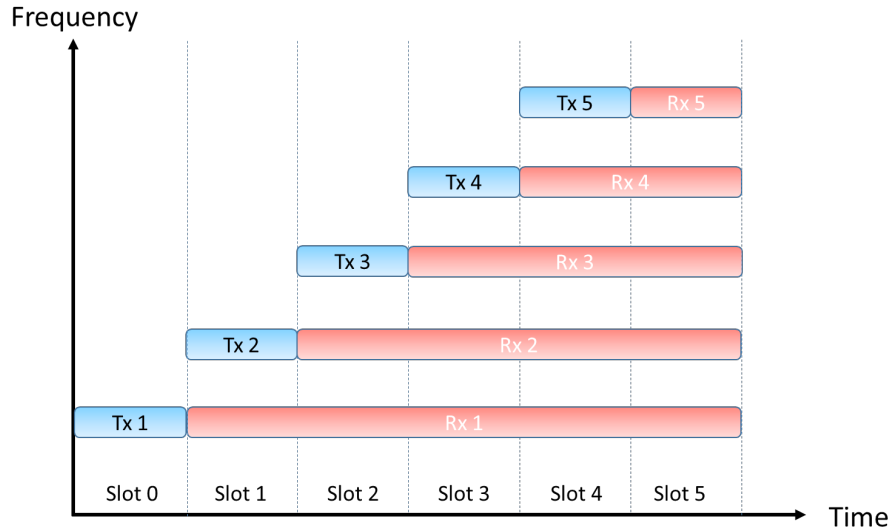
Fig. 5.1. Time-frequency representation of the Tx and Rx frequencies. The blue blocks in the figure represent the signals from the transmitter, and the red blocks represent the signals at the receiver. In time slots 1, 2, 3, and 4 the microwave spectroscopy system simultaneously transmit and receive signals at different frequencies.

achieved by cascading multiple tunable unit, where each unit, as shown in Fig. 5.2, can be tuned within a channelized bandwidth.
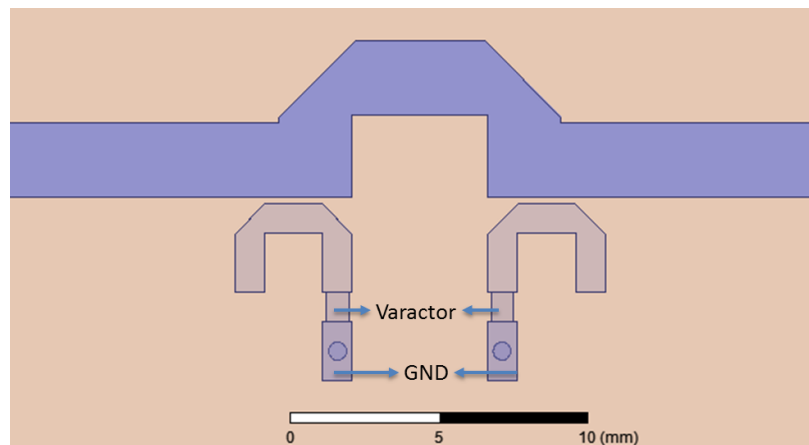
Fig. 5.2. A second-order hairpin tunable ABSF. In this design, each hairpin resonator is tuned by a varactor, and therefore the center frequency of the ABSF can be changed.
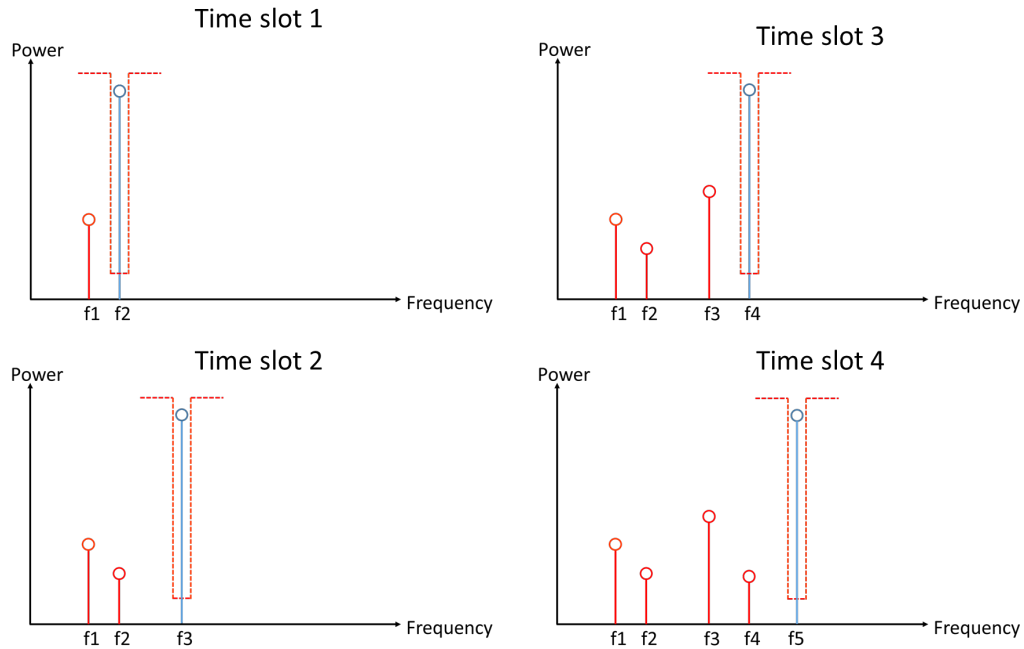
Fig. 5.3. Power-frequency representation of simultaneous transmit and receive in time slots 1,2,3, and 4 in Fig. 5.1. The red peaks in the figure represent the weak molecular signals, and the blue peaks represent the strong transmitted signals that are used to excite chemicals in the analysis cell. The red dashed line in each time slot represents a bandstop filter that is used to isolate the transmit signal in order to protect the LNA from being damaged or saturated.

In this chapter, we will first introduce the synthesis and design of a two-pole absorptive bandstop filter, and the implementation of the absorptive bandstop filter by using planar resonator structures will also be introduced. Finally in this chapter, we use the fabricated absorptive bandstop filter and set up an STAR demonstration of methanol detection.

5.1 Absorptive Bandstop Filter Design

A topology of a two-pole absorptive bandstop filter is shown in Fig. 5.4. In this topology, S (source) and L (load) denote the input and output ports, and 1 and 2

denotes resonator 1 and resonator 2. Coupling coefficients between each nodes are represented by k_{mn} and should follow the following equation [49], [48]

$$k_{01} = k_{23} = \pm\sqrt{\frac{2}{Q_u}}, \tag{5.1}$$

$$k_{12} = \pm\frac{1}{Q_u}, \tag{5.2}$$

$$k_{03} = \pm 1, \tag{5.3}$$

$$\text{sign}(k_{12}) = \text{sign}(k_{03}), \tag{5.4}$$

where Q_u is the unloaded Q-factor of the resonators. For a symmetrical filter structure, the coupling coefficients k_{01} and k_{23} are equal and can both be positive or both negative. These two coupling structure will result in 180 degrees phase shift. Furthermore, coupling coefficients k_{03} and k_{12} should be the same sign, as shown in Eq. (5.4), such that the phase changes by k_{03} and k_{12} are both +90 degrees or −90 degrees. As a result, the absorptive bandstop response will be created because the two signal paths, as shown in Fig. 5.5, will be 180 degrees out of phase and destructively interfere with each at the output port.

5.2   Filter Implementation

We implement our absorptive bandstop filter by using two planar hairpin resonators, as shown in Fig. 5.6, on a 0.7874 mm Rogers 5880 substrate (ϵ_r=2.2. Each hairpin resonator has a total length of 15 mm and unloaded-Q of 190. The coupling gap between the microstrip line to each resonator is 650 μm, and the gap between the two resonators is 5.8 mm. More details about the design and simulation procedure is provided in Appendix B. Simulated and measured results of this designed filter is shown in Fig. 5.7, and the 3% frequency shift between simulation and measurement is due to fabrication variability from the milling machine. In this figure, the sharp decrease in S11 indicates the absorptive response, and the maximum isolation
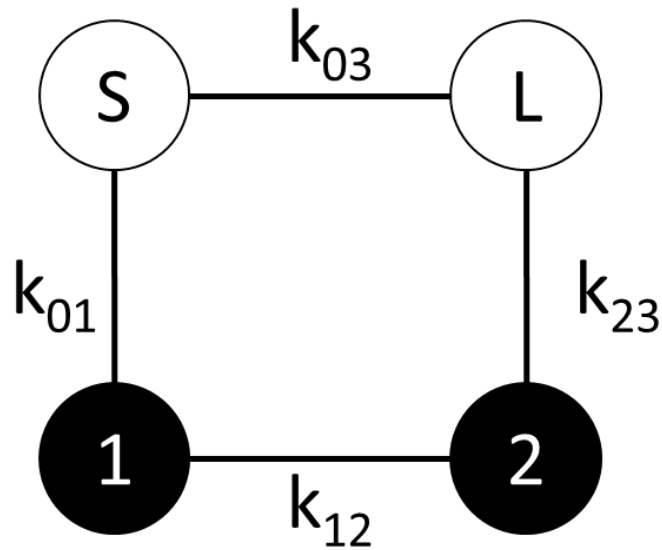
Fig. 5.4. A two-pole absorptive bandstop filter topology. S (source) and L (load) denote the input and output ports, and 1 and 2 denotes resonator 1 and resonator 2. Coupling coefficients between each nodes are represented by k_{mn} and should follow the following equation. As opposed to a reflective-type bandstop filter topology, the absorptive bandstop filter requires mutual coupling between resonator 1 and 2 to achieve the absorptive response.

at the center frequency is 29.7 dB. This figure also shows that this filter has a 3-dB bandwidth of 100 MHz and 10-dB bandwidth of 29 MHz.

5.3 Simultaneous Transmit and Receive

In section 5.2 we have demonstrated the implementation of a static 8.091 GHz absorptive bandstop filter, and in Chapter 4 we demonstrated starting the detection simultaneously with the end of the transmit pulse. A even faster detection can be achieved by using the time-frequency scheme as shown in Fig. 5.1. In this section, we will use this fabricated absorptive bandstop filter to set up a demonstration of
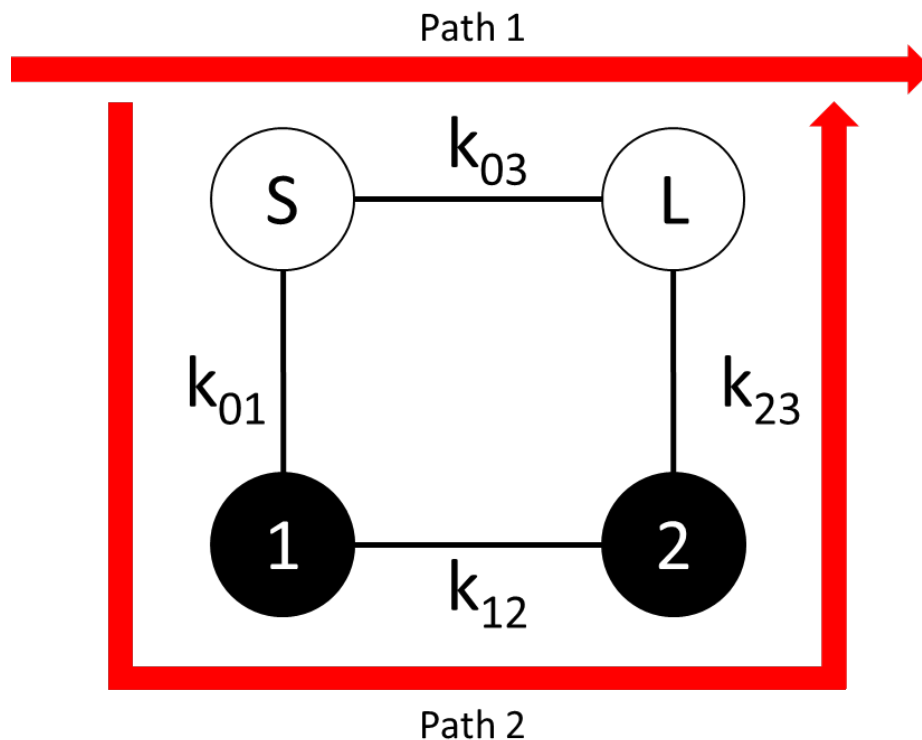
Fig. 5.5. Signal path diagram of the absorptive bandstop filter design shown in Fig. 5.4. The red arrows represent the two different paths that the input signal is routed. The split signals in path 1 and path 2 are 180 degrees out of phase and cancel each other at the output port. Switching off the filter can be done by zeroing k01 and k23 or by increasing k12, which is equivalent to strongly couple the two resonators to change the selective resonance.

simultaneously receiving one methanol resonance while transmitting another probing signal, which mimics time slot 1 in Fig. 5.1.

Fig. 5.8 shows the schematic of the experiment setup. An excitation pulse is generated by an arbitrary waveform generator (Tektronix AWG 7101). The output waveform of the arbitrary waveform generator is then upconverted to a higher frequency band by using a frequency multiplier. The excitation pulse is then amplified and sent into the analysis cell to excite the enclosed chemical species. In the receiver circuit, we use an LNA (Miteq AMF-6F-06001800-15-10P) to amplify the weak
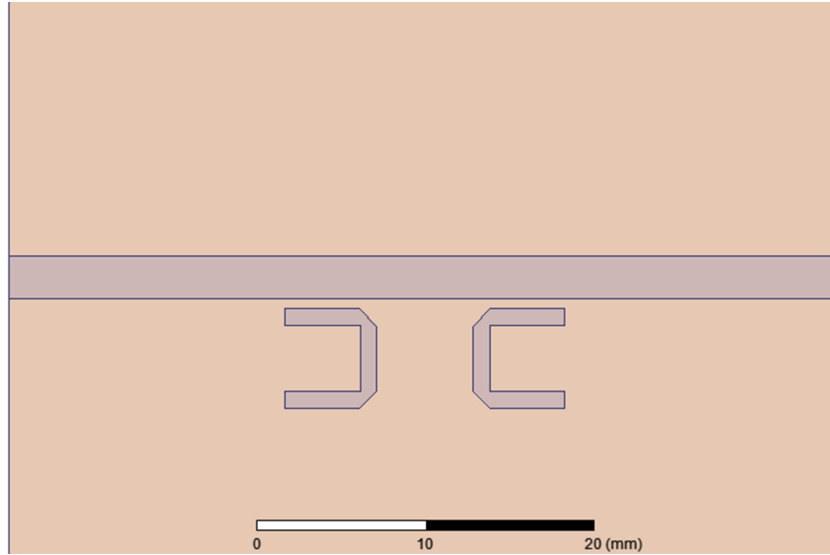
Fig. 5.6. Top view of the planar absorptive bandstop filter design in HFSS. As shown in the figure, two hairpin resonators are implemented on a 0.7874 mm thick Rogers 5880 substrate. The coupling gap between each filter to the microstrip line is 650 μm, and the mutual coupling distance between the two resonators is 5.8 mm.

molecular signal, and a PIN diode limiter (Advanced Control Components ACLM-4619FC361K) and a solid-state switch (ATM PNR S1517D) are used to protect the LNA when the transmitting signal is not isolated by a filter. The molecular signal is downconverted by mixing with a 18.9 GHz local oscillator to be digitized by the Guzik 6131 digitizer.

In this system, a 1 μs and 2 MHz bandwidth chirped pulse centered at 12.229 GHz pulse will be generated by the arbitrary waveform generator to excite methanol molecules in the large electrical volume coaxial cable. The receiver is protected by the solid-state switch, which is used to mimic the existence of a 12.229 GHz absorptive bandstop filter, to prevent the LNA from damage and saturation by the 12.229 GHz chirped pulse. We have used a power combiner and a second signal generator to input a second pulse at 8.091 GHz after the 12.229 GHz pulses ends to mimic the excitation of another methanol resonance while detecting the 12.229 GHz resonance simultaneously. The protection of LNA from damage and saturation by the 8.091
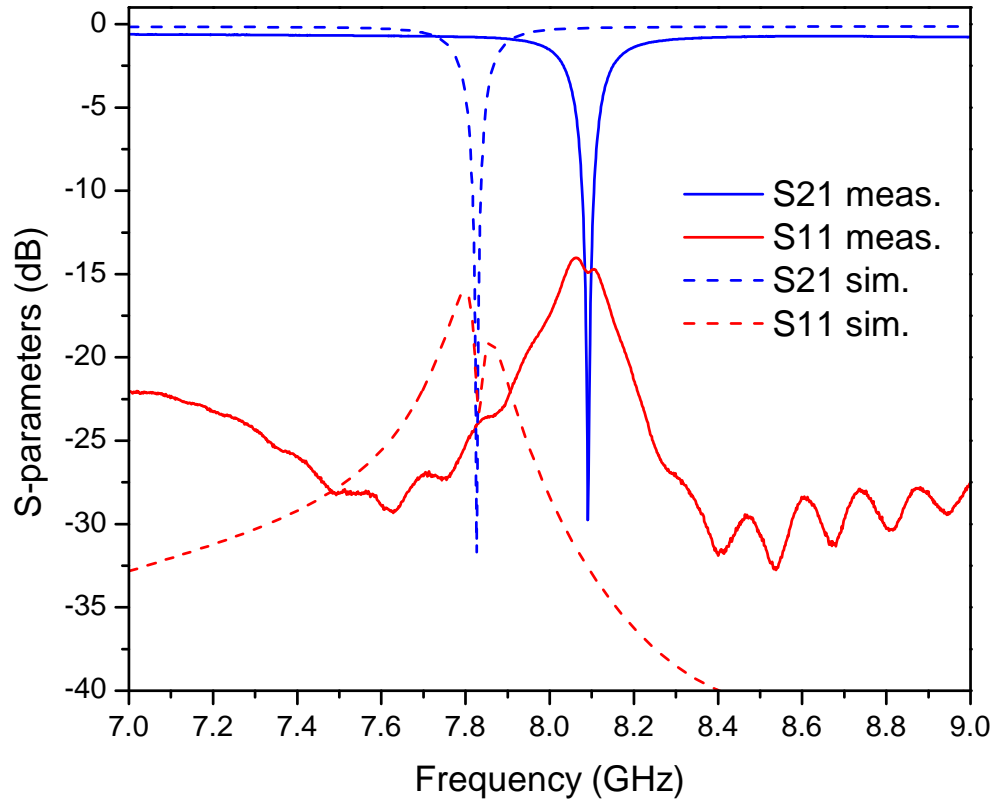
Fig. 5.7. Measured and simulated S-parameters of the designed absorptive bandstop filter. The measured S_{21} has isolation of 29.7 dB at the center frequency. 3-dB bandwidth and 10-dB bandwidth are 100 MHz and 29 MHz, respectively. The frequency offset between the simulation and measurement is due to variability of the total length of the resonators, which has been shown to be able to be corrected with varactors [50], [51].

GHz pulse is done by the static absorptive bandstop filter designed in Section 5.2. A timing unit (Stanford Research Systems DG535) is used to control the arbitrary waveform generator, solid-state switch, signal generator, and the real-time digitizer, and the whole system is synchronized by a 10 MHz rubidium frequency standard (Stanford Research Systems SF725) for coherent signal averaging.

Fig. 5.9 shows an recorded waveform as an example. A 12.229 GHz chirped pulse is transmitted from 0 to 1 μs and is covered by a solid-state switch at the receiver. After

this chirped pulse ends at 1 μs a 8.091 GHz signal is transmitted and is isolated by an absorptive bandstop filter at the receiver. Fig. 5.10 shows the measured spectrum at different input power of the 8.091 GHz tone. We can see from Fig. 5.10 that when the methanol resonance is embedded in a -4 dBm or -5 dBm transmit signal, the LNA still can amplify the weak molecular resonance. However, the isolated transmit tone is close to the P1dB of the LNA, and therefore LNA generate spurious tones in the background. A -30 dBm transmit tone is also shown in Fig. 5.10 as an example to show that the spurs in the background can be greatly reduced if the filter has more attenuation.

A future microwave spectrometer with ABSF implementation will allow for a more sophisticated operation where a low power broadband chirp can be used to probe large molecular resonances of a suspicious chemical class, and species confirmation can be done by exploring smaller resonances at multiple frequencies. These resonances will only be at certain frequencies for a certain chemical, and detection of these small resonances can be be enhanced by moving the filters to these frequency regions to excite the chemical with a higher power (30 dB more than the original signal) such that these small resonances can be extracted from the noise. By this method, the chemical can be explored by first using a broadband waveform to conduct a coarse scan for large dipoles and a narrow pulse for confirmatory peaks.
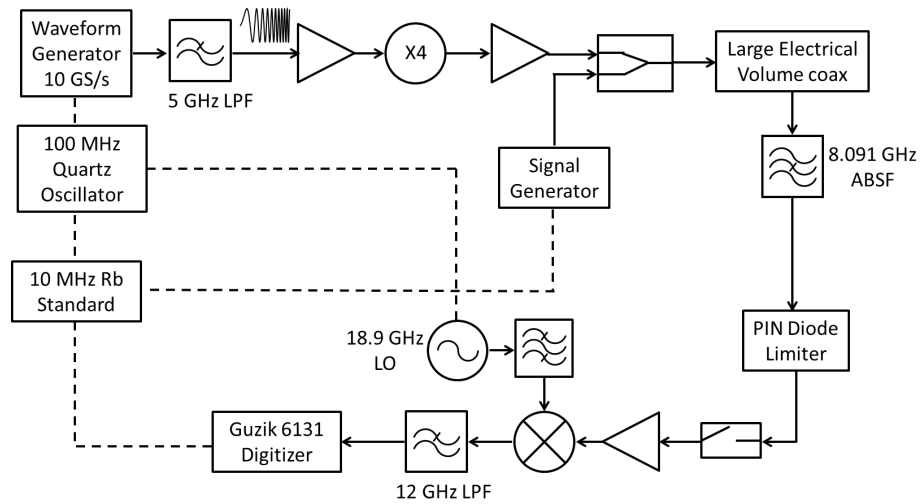
Fig. 5.8. Schematic of the experiment setup for simultaneous transmit and receive.
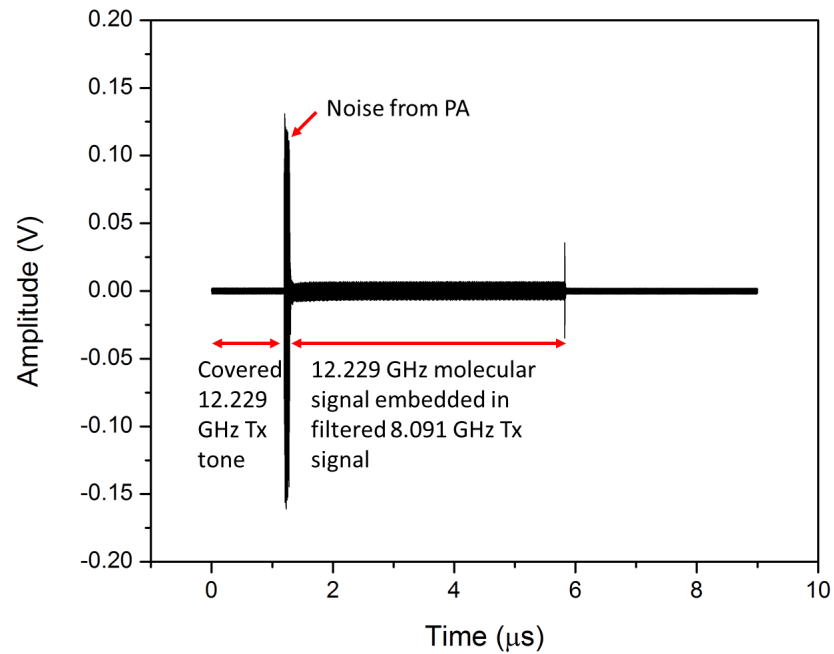
Fig. 5.9. Recorded waveform of the simultaneous transmit and receive experiment. From 0 to 1 μs a 12.229 GHz chirped is transmitted to excite methanol in the LEVC. A 8.091 GHz pulse generated by a signal generator follows the 12.229 GHz chirped pulse and is transmitted from 1 μs to 6 μs, and therefore the re-emitted methanol signal (~ -97 dBm) is buried in the 8.091 GHz tone (-3 dBm). The PA noise at the end of the 1 μs is the result of transient effect, when the PA is switched off, that contains a wide spectral content.
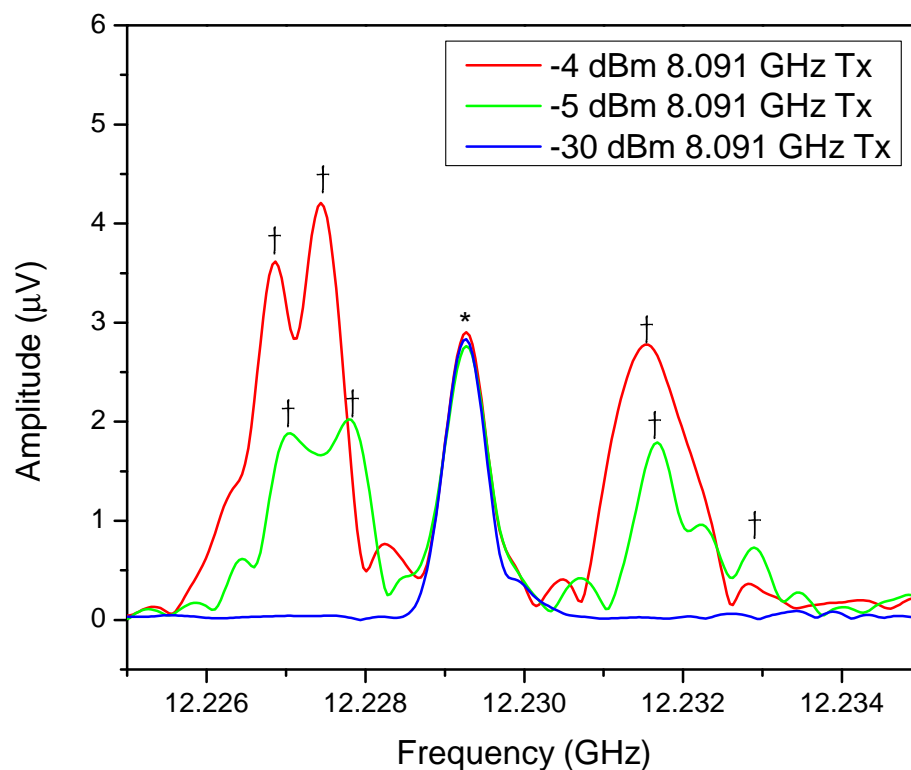
Fig. 5.10. Measured simultaneous transmit and receive spectrum at three different transmit power. The asterisk ($*$) indicates methanol resonance, and daggers ($\dagger$) indicate spurious modes. It can be seen from the figure that when the transmit power is -4 dBm and -5 dBm, although methanol spectral line can be measured, the LNA is still stressed and generates spurious tones. With a -30 dBm transmit power, spurs from the LNA are reduced, and the methanol spectral line stands out from a clean background.

6. SUMMARY AND FUTURE WORK

In this work, we have demonstrated practical methods to design overmoded waveguide and tapered coaxial transmission line that can be used as analysis cells in a microwave spectrometer. Mode coupling issues between the fundamental mode to higher order modes has been studied: coupling between the TM_{10} and TM_{12} modes can be reduced by using a bifurcation in an overmoded waveguide, and coupling between the TEM and TM_{01} modes in a coaxial transmission line can be avoided by a proper choice of inner and outer radius of a coaxial cable. For a more aggressive taper in a coaxial transmission line, e.g. our LEVC design, we have also demonstrated practical ways to build dielectric supports for the center conductor while eliminating coupling between the TEM mode and higher order modes to create a resonance free passband.

Geometry dependent molecular signal decay is also studied in both the LEVC and OMC transmission lines in Chapter 3. From the results of signal decay, it is found that the pressure-dependent molecular dephasing time is is about 0.12 mean collision time. The signal decay prediction shows good agreement with measurement in both LEVC and OMC. This result is further used to predict molecular signal strength with earlier start detection in Chapter 4. The prediction shows good agreement with measured results, and we also compare the signal strength at various input power level. With the fast signal integration advantage of Guzik real-time digitizer, we explored low input power and pushed the started detection time to increase the SNR. Our measurement shows that at 1 million averages a -3 dBm input gives an SNR of 35 dB. An even lower input power could be used with a tradeoff of SNR or total detection time. Furthermore, total signal processing time to acquire a spectrum can be reduced when application-specific integrated circuits replace FPGAs in the digitizer.

Finally, we successfully set up a demonstration of simultaneous transmit and receive by using an absorptive bandstop filter to isolate the Tx signal. This demonstra-

tion proves the concept that by dividing a Tx time frame into $2N$ blocks, we will be able to probe $2N - 1$ resonances in one Rx segment, as shown in Fig. 6.1. Although an alternative way can be done by switching the receiver chain on-and-off and probe one resonance at a time, as shown in Fig. 6.2, this detection mechanism will take almost twice as much time to probe through all resonances. A future low power and portable microwave chemical sensor can be expected with a tunable absorptive filter bank, as shown in Fig. 6.3, such that we can excite and detect signals simultaneously at any desired frequencies.

Recent advances in microwave components allow for the promise of a new role of microwave spectroscopy for chemical analysis. Designs of high power and high frequency power amplifier have progressed tremendously, particularly with III-V materials and even with silicon circuits, which was considered difficult in the past. Direct sampling wideband receivers greatly simplify the detection of signals, and the combination of wideband sampling and real-time averaging creates unprecedented sensitivity and speed. Together with the continuing advances in micropumps [52], [53], compact microwave spectrometers will continue to improve, and its future applications include small UAVs or ground robotics which can map out or search out specific chemicals, handheld systems for first responders, or real time forensics. The microwave spectrometer is poised to break out of the lab and into the world where it can be used for a wide variety of applications.
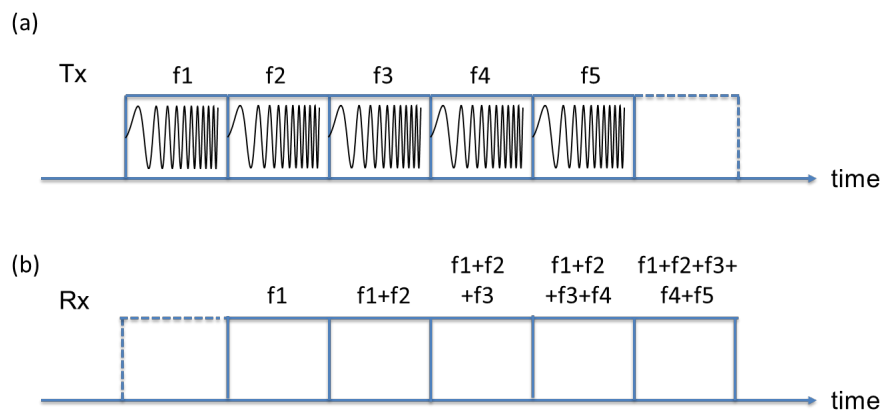
Fig. 6.1. (a) A Tx frame divided into $2N$ blocks, $N = 3$, is shown as an example of STAR. In this example, 5 pulses are transmitted to probe the molecular resonances in each block. (b) An Rx frame that shows detectable resonance frequency using the Tx signal in (a).
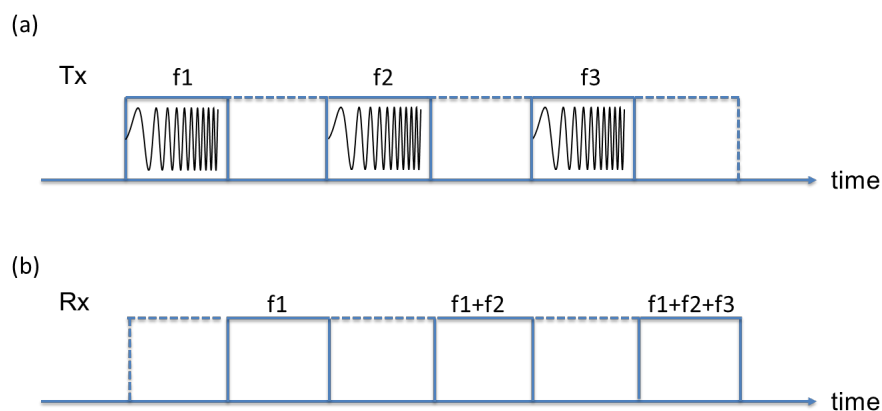
Fig. 6.2. An on-and-off detection scheme is illustrated. In (a), by dividing the Tx frame into 6 blocks, the transmitter can only transmit 3 pulses. Similarly, as shown in (b), only 3 resonances can be detected in one Rx segment.
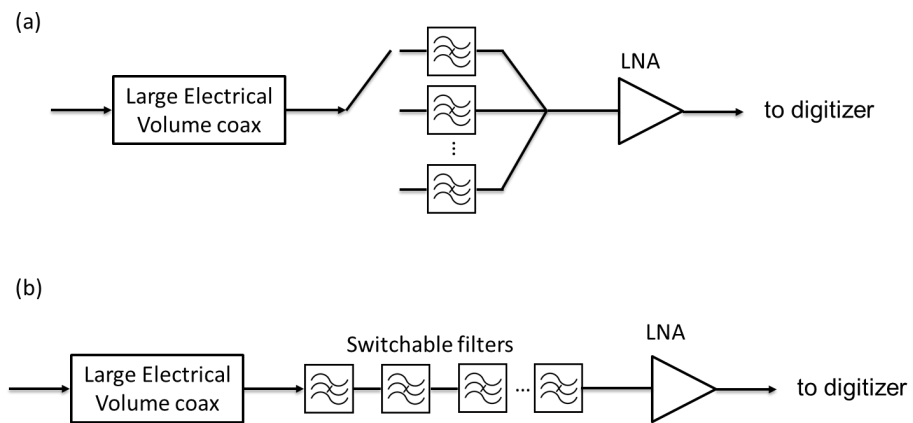
Fig. 6.3. Future spectrometer that contains (a) a parallel ABSF bank or (b) series ABSF bank.

REFERENCES

REFERENCES

[1] W. Gordy and C. R.L., *Microwave Molecular Spectra.* John Wiley & Sons, New York, 1984.

[2] C. Townes and A. Schawlow, *Microwave spectroscopy.* McGraw-Hill, New York, 1955.

[3] J. Woolrab, *Rotational Spectra and Molecular Structure.* Academic, New York, 1967.

[4] K. Demyk, H. Mäder, B. Tercero, J. Cemicharo, J. Demaison, L. Margulès, M. Wegner, S. Keipert, and M. Sheng, "Isotopic ethyl cyanide $^{13}CH_3CH_2CN$, $CH_3{}^{13}CH_2CN$, and $CH_3CH_2{}^{13}CN$: laboratory rotational spectrum and detection in Orion," *Astronomy and astrophysics*, vol. 466, no. 1, pp. 255–259, 2007.

[5] H. S. Müller, A. Belloche, K. M. Menten, C. Comito, and P. Schilke, "Rotational spectroscopy of isotopic vinyl cyanide, H_2CCHCN, in the laboratory and in space," *Journal of Molecular Spectroscopy*, vol. 251, no. 1, pp. 319–325, 2008.

[6] L. Margulès, R. Motiyenko, K. Demyk, B. Tercero, J. Cernicharo, M. Sheng, M. Weidmann, J. Gripp, H. Mäder, and J. Demaison, "Rotational spectrum of deuterated and ^{15}N ethyl cyanides: CH_3CHDCN and CH_2DCH_2CN and of $CH_3CH_2C^{15}N$," *arXiv preprint arXiv:0811.1096*, 2008.

[7] Z. Kisiel, L. Pszczółkowski, B. J. Drouin, C. S. Brauer, S. Yu, and J. C. Pearson, "The rotational spectrum of acrylonitrile up to 1.67 THz," *Journal of Molecular Spectroscopy*, vol. 258, no. 1, pp. 26–34, 2009.

[8] I. Kleiner, M. Carvajal Zaera, L. Margulès, B. Tercero, K. Demyk, J. Guillemin, V. Lattanzi, A. Walters, J. Demaison, G. Wlodarczak *et al.*, "Rotational spectrum of $^{13}C_2$-methyl formate ($HCOO^{13}CH_3$) and detection of the two ^{13}C-methyl formate in Orion," *Astronomy and Astrophysics*, vol. 500, no. 3, pp. 1109–1118, 2009.

[9] I. Medvedev, C. Neese, G. Plummer, and F. De Lucia, "Submillimeter spectroscopy for chemical analysis with absolute specificity," *Optics letters*, vol. 35, no. 10, pp. 1533–1535, 2010.

[10] M. D. Brickhouse, W. R. Creasy, B. R. Williams, K. M. Morrissey, R. J. OConnor, and H. Dupont Durst, "Multiple-technique analytical characterization of a mixture containing chemical-weapons simulant from a munition," *Journal of Chromatography A*, vol. 883, no. 1, pp. 185–198, 2000.

[11] R. Bousquet, P. Chu, R. DaBell, J. Grabow, and R. Suenram, "Trends in microwave spectroscopy for the detection of chemical agents," *Sensors Journal, IEEE*, vol. 5, no. 4, pp. 656–664, 2005.

[12] R. Romer and R. Dicke, "New technique for high-resolution microwave spectroscopy," *Physical Review*, vol. 99, no. 2, p. 532, 1955.

[13] T. Balle, E. Campbell, M. Keenan, and W. Flygare, "A new method for observing the rotational spectra of weak molecular complexes: KrHCl," *The Journal of Chemical Physics*, vol. 71, no. 6, pp. 2723–2724, 1979.

[14] ——, "A new method for observing the rotational spectra of weak molecular complexes: KrHCl," *The Journal of Chemical Physics*, vol. 72, no. 2, pp. 922–932, 1980.

[15] T. Balle and W. Flygare, "Fabry–Perot cavity pulsed Fourier transform microwave spectrometer with a pulsed nozzle particle source," *Review of Scientific Instruments*, vol. 52, no. 1, pp. 33–45, 1981.

[16] R. Suenram, J. U. Grabow, A. Zuban, and I. Leonov, "A portable, pulsed-molecular-beam, Fourier-transform microwave spectrometer designed for chemical analysis," *Review of scientific instruments*, vol. 70, no. 4, pp. 2127–2135, 1999.

[17] A. K. King and B. J. Howard, "A high-resolution microwave study of the conformations of butan-2-ol in a supersonic expansion," *Journal of molecular spectroscopy*, vol. 205, no. 1, pp. 38–42, 2001.

[18] J.-U. Grabow, W. Stahl, and H. Dreizler, "A multioctave coaxially oriented beam-resonator arrangement Fourier-transform microwave spectrometer," *Review of scientific instruments*, vol. 67, no. 12, pp. 4072–4084, 1996.

[19] E. Arunan, S. Dev, and P. K. Mandal, "Pulsed nozzle Fourier transform microwave spectrometer: Advances and applications," *Applied Spectroscopy Reviews*, vol. 39, no. 2, pp. 131–181, 2004.

[20] G. Brown, B. Dian, K. Douglass, S. Geyer, S. Shipman, and B. Pate, "A broadband Fourier transform microwave spectrometer based on chirped pulse excitation," *Review of Scientific Instruments*, vol. 79, p. 053103, 2008.

[21] S. Shipman, B. Kroncke, B. Pate, and P. Groner, "Waveguide Chirped-Pulse Fourier Transform Microwave Spectroscopy," in *63th International Symposium On Molecular Spectroscopy*, 2008.

[22] B. Reinhold, I. Finneran, and S. Shipman, "Room temperature chirped-pulse Fourier transform microwave spectroscopy of anisole," *Journal of Molecular Spectroscopy*, vol. 207, pp. 89–97, 2011.

[23] P. W. Atkins, *Physical Chemistry. 6th.* Oxford University Press, Oxford, Melbourne, Tokyo, 1998.

[24] G. Thirup, F. Benmakroha, A. Leontakianakos, and J. Alder, "Analytical microwave spectrometer employing a Gunn oscillator locked to the rotational absorption line," *Journal of Physics E: Scientific Instruments*, vol. 19, pp. 823–830, 1986.

[25] J. F. Alder and J. G. Baker, *Quantitative Millimetre Wavelength Spectrometry.* Royal Society of Chemistry (Great Britain), Cambridge, 2002.

[26] W. D. Hershberger, "Minimum detectable absorption in microwave spectroscopy and an analysis of the Stark modulation method," *Journal of Applied Physics*, vol. 19, no. 4, pp. 411–419, 1948.

[27] R. H. Hughes and E. B. Wilson Jr, "A microwave spectrograph," *Physical Review*, vol. 71, no. 8, p. 562, 1947.

[28] K. McAfee Jr, R. H. Hughes, and E. B. Wilson Jr, "A Stark-Effect Microwave Spectrograph of High Sensitivity," *Review of Scientific Instruments*, vol. 20, no. 11, pp. 821–826, 1949.

[29] R. Sanchez, W. Caminati, J. C. López, and J. L. Alonso, "The rotational spectra of conformers of biomolecules: Tryptophol," *Chemical physics letters*, vol. 414, no. 1, pp. 226–229, 2005.

[30] M. E. Sanz, A. Lesarri, M. I. Peña, V. Vaquero, V. Cortijo, J. C. López, and J. L. Alonso, "The Shape of β-Alanine," *Journal of the American Chemical Society*, vol. 128, no. 11, pp. 3812–3817, 2006.

[31] D. F. Plusquellic, I. Kleiner, J. Demaison, R. D. Suenram, R. J. Lavrich, F. J. Lovas, G. T. Fraser, and V. V. Ilyushin, "The microwave spectrum of a two-top peptide mimetic: The N-acetyl alanine methyl ester molecule," *The Journal of chemical physics*, vol. 125, no. 10, p. 104312, 2006.

[32] Z. Kisiel, A. Kraśnicki, L. Pszczółkowski, S. T. Shipman, L. Alvarez-Valtierra, and B. H. Pate, "Assignment and analysis of the rotational spectrum of bromoform enabled by broadband FTMW spectroscopy," *Journal of Molecular Spectroscopy*, vol. 257, no. 2, pp. 177–186, 2009.

[33] J. L. Alonso, M. E. Sanz, J. C. López, and V. Cortijo, "Conformational behavior of norephedrine, ephedrine, and pseudoephedrine," *Journal of the American Chemical Society*, vol. 131, no. 12, pp. 4320–4326, 2009.

[34] J. L. Neill, S. T. Shipman, L. Alvarez-Valtierra, A. Lesarri, Z. Kisiel, and B. H. Pate, "Rotational spectroscopy of iodobenzene and iodobenzene–neon with a direct digital 2–8 GHz chirped-pulse Fourier transform microwave spectrometer," *Journal of Molecular Spectroscopy*, vol. 269, no. 1, pp. 21–29, 2011.

[35] J. McGurk, T. Schmalz, and W. Flygare, "Fast passage in rotational spectroscopy: theory and experiment," *The Journal of Chemical Physics*, vol. 60, no. 11, pp. 4181–4188, 1974.

[36] J. McGurk, R. Hofmann, and W. Flygare, "Transient absorption and emission and the measurement of T_1 and T_2 in the J 0→1 rotational transition in OCS," *The Journal of Chemical Physics*, vol. 60, p. 2922, 1974.

[37] D. M. Pozar, *Microwave Engineering*. John Wiley&Son In, 2005.

[38] μWave Wizard 7.0. Mician GmbH, Bremen, Germany, 2009.

[39] C. Nantista, "Overmoded Waveguide Components for High-Power RF," in *AIP Conference Proceedings*. Iop Institute of Physics Publishing LTD, 2003, pp. 263–271.

[40] L. Xu and F. Lovas, "Microwave Spectra of Molecules of Astrophysical Interest. XXIV. Methanol," *Journal of Physical and Chemical Reference Data*, vol. 26, no. 1, pp. 17–156, 1997.

[41] Y. Wang, "New method for tapered transmission line design," *Electronics Letters*, vol. 27, no. 25, pp. 2396–2398, 1991.

[42] Y.-T. Huang, K. Hotopp, B. Dian, and W. J. Chappell, "Microwave Chemical Sensing Using a 3-18 GHz Wideband Overmoded Coaxial Cable," in *Microwave Symposium Digest (MTT), 2012 IEEE MTT-S International*, 2012, pp. 1–3.

[43] R. A. Serway and J. W. Jewett Jr, *Physics for scientists and engineers*. Brooks/Cole Publishing Company, 2009, vol. 1.

[44] D. A. McQuarrie and J. D. Simon, *Physical chemistry: a molecular approach*. Univ Science Books, Sausalito, California, 1997.

[45] R. G. Lyons, *Understanding digital signal processing*. Pearson Education, 2010.

[46] F. Wolf, "Fast sweep experiments in microwave spectroscopy," *Journal of Physics D: Applied Physics*, vol. 27, no. 8, p. 1774, 1994.

[47] J. W. Nilsson, *Electric circuits*. Pearson Education India, 2008.

[48] T. Snow, J. Lee, and W. Chappell, "Tunable high quality-factor absorptive bandstop filter design," in *Microwave Symposium Digest (MTT), 2012 IEEE MTT-S International*. IEEE, 2012, pp. 1–3.

[49] D. R. Jachowski, "Compact, frequency-agile, absorptive bandstop filters," in *Microwave Symposium Digest (MTT), 2005 IEEE MTT-S International*. IEEE, 2005, pp. 1–4.

[50] J. Lee, T. C. Lee, and W. J. Chappell, "Lumped-element realization of absorptive bandstop filter with anomalously high spectral isolation," *Microwave Theory and Techniques, IEEE Transactions on*, vol. 60, no. 8, pp. 2424–2430, 2012.

[51] T.-C. Lee, J. Lee, E. J. Naglich, and D. Peroulis, "Octave tunable lumped-element notch filter with resonator-Q-independent zero reflection coefficient," in *Microwave Symposium (IMS), 2014 IEEE MTT-S International*. IEEE, 2014, pp. 1–4.

[52] H. Kim, A. A. Astle, K. Najafi, L. P. Bernal, and P. D. Washabaugh, "An Integrated Electrostatic Peristaltic 18-Stage Gas Micropump With Active Microvalves," *Microelectromechanical Systems, Journal of*, vol. 24, pp. 192–206, 2014.

[53] A. Besharatian, K. Kumar, R. L. Peterson, L. P. Bernal, and K. Najafi, "A scalable, modular, multi-stage, peristaltic, electrostatic gas micro-pump," in *Micro Electro Mechanical Systems (MEMS), 2012 IEEE 25th International Conference on*. IEEE, 2012, pp. 1001–1004.

[54] A. E. Williams, "A four-cavity elliptic waveguide filter," *Microwave Theory and Techniques, IEEE Transactions on*, vol. 18, no. 12, pp. 1109–1114, 1970.

[55] A. E. Atia and A. E. Williams, "Narrow-bandpass waveguide filters," *Microwave Theory and Techniques, IEEE Transactions on*, vol. 20, no. 4, pp. 258–265, 1972.

[56] R. J. Cameron, C. M. Kudsia, and R. R. Mansour, *Microwave filters for communication systems: Fundamentals, Design, and Applications.* John Wiley & Sons, Inc, 2007.

[57] G. Matthaei, L. Young, and E. M. T. Jones, *Microwave Filters, Impedance Matching Networks and Coupling Structures.* Norwood, MA: Artech House, Inc., 1980.

APPENDICES

A. TM WAVES IN A COAXIAL CABLE

For a coaxial cable with inner conductor radius a and outer conductor radius b, TM (transverse magnetic) waves can be solved by solving the wave equation [37]

$$\nabla^2 E_z + k^2 E_z = 0. \tag{A.1}$$

In a cylindrical coordinate, the above equation can be expressed as

$$\left(\frac{\partial^2}{\partial \rho^2} + \frac{1}{\rho} \frac{\partial}{\partial \rho} + \frac{1}{\rho^2} \frac{\partial^2}{\partial \phi^2} + k_c^2 \right) e_z (\rho, \phi) = 0, \tag{A.2}$$

where $E_z = e_z (\rho, \phi) e^{-j\beta z}$, and $k_c^2 = k^2 - \beta^2$. By using separation of variables and define e_z as

$$e_z (\rho, \phi) = (A \sin m\phi + B \cos m\phi) (C J_m (k_c \rho) + D Y_m (k_c \rho)), \tag{A.3}$$

where J_m and Y_m are the Bessel functions of first and second kinds. The ϕ-component and ρ-component of the electric field can then be expressed as

$$
\begin{aligned}
E_\phi &= \frac{-j}{k_c^2} \left(\frac{\beta}{\rho} \frac{\partial E_z}{\partial \phi} - \omega\mu \frac{\partial H_z}{\partial \rho} \right) \\
&= \frac{-j}{k_c^2} \left(\frac{\beta}{\rho} (mA \cos m\phi - mB \sin m\phi) \right) (C J_m (k_c \rho) + D Y_m (k_c \rho)), \\
E_\rho &= \frac{-j}{k_c^2} \left(\beta \frac{\partial E_z}{\partial \rho} + \frac{\omega\mu}{\rho} \frac{\partial H_z}{\phi} \right) \\
&= \frac{-j\beta}{k_c^2} (A \sin m\phi + B \cos m\phi) \left(C J_m' (k_c \rho) + D Y_m' (k_c \rho) \right).
\end{aligned}
\tag{A.4}
$$

The boundary condition $e_z = 0$ must be satisfied at $\rho = a$ and $\rho = b$ because tangential electric field cannot exist at metal surface, and therefore we have the following equations

$$CJ_m\left(k_ca\right) + DY_m\left(k_ca\right) = 0$$
$$CJ_m\left(k_cb\right) + DY_m\left(k_cb\right) = 0$$

(A.5)

For non-trivial solutions, the determinant of the system equations in Eq. (A.5) must be zero.

$$\det \begin{vmatrix} J_m\left(k_ca\right) & Y_m\left(k_ca\right) \\ J_m\left(k_cb\right) & Y_m\left(k_cb\right) \end{vmatrix} = 0$$

(A.6)

Finally, we have

$$J_m\left(k_ca\right) Y_m\left(k_cb\right) = J_m\left(k_cb\right) Y_m\left(k_ca\right),$$

(A.7)

and for given a and b, cutoff wavenumber of the TM_{mn} modes of can be found by solving Eq. (A.7) numerically, where m indicates the order of the Bessel functions, and n represents the n-th solution of Eq. (A.7).

B. ABSORPTIVE BANDSTOP FILTER IMPLEMENTATION PROCEDURE

In this section we will describe the detailed steps about the two-pole absorptive bandstop filter implementation using hairpin resonators. We will use the normalized coupling coefficients in this chapter to illustrate the S-parameters response in the implementation procedure.

A N-pole filter network can be described by using a normalized coupling-matrix to describe the coupling between each node [54], [55], [56], as described in Eq. (B.6).

$$\mathbf{M} = \begin{bmatrix} 0 & M_{01} & M_{02} & \cdots & M_{0,N-1} & M_{0,N} & M_{0,N+1} \\ M_{01} & 0 & M_{12} & \cdots & M_{1,N-1} & M_{1,N} & M_{1,N+1} \\ M_{02} & M_{12} & 0 & \cdots & M_{2,N-1} & M_{2,N} & M_{2,N+1} \\ \vdots & \vdots & \vdots & \ddots & \vdots & \vdots & \vdots \\ M_{0,N-1} & M_{1,N-1} & M_{2,N-1} & \cdots & 0 & M_{N-1,N} & M_{N-1,N+1} \\ M_{0,N} & M_{1,N} & M_{2,N} & \cdots & M_{N-1,N} & 0 & M_{N,N+1} \\ M_{0,N+1} & M_{1,N+1} & M_{2,N+1} & \cdots & M_{N-1,N+1} & M_{N,N+1} & 0 \end{bmatrix} \quad \text{(B.1)}$$

The transfer function of this network can then expressed $S_{21}(S) = 2(\mathbf{R} + S\mathbf{U} + j\mathbf{M})^{-1}_{N+2,1}$ [57], where

$$\mathbf{R} = \begin{bmatrix} 1 & 0 & 0 & \cdots & 0 & 0 & 0 \\ 0 & 0 & 0 & \cdots & 0 & 0 & 0 \\ 0 & 0 & 0 & \cdots & 0 & 0 & 0 \\ \vdots & \vdots & \vdots & \ddots & \vdots & \vdots & \vdots \\ 0 & 0 & 0 & \cdots & 0 & 0 & 0 \\ 0 & 0 & 0 & \cdots & 0 & 0 & 0 \\ 0 & 0 & 0 & \cdots & 0 & 0 & 1 \end{bmatrix}, \quad \text{(B.2)}$$

$$\mathbf{U} = \begin{bmatrix} 0 & 0 & 0 & \cdots & 0 & 0 & 0 \\ 0 & 1 & 0 & \cdots & 0 & 0 & 0 \\ 0 & 0 & 1 & \cdots & 0 & 0 & 0 \\ \vdots & \vdots & \vdots & \ddots & \vdots & \vdots & \vdots \\ 0 & 0 & 0 & \cdots & 1 & 0 & 0 \\ 0 & 0 & 0 & \cdots & 0 & 1 & 0 \\ 0 & 0 & 0 & \cdots & 0 & 0 & 0 \end{bmatrix}, \tag{B.3}$$

$$S = j\Omega, \tag{B.4}$$

$$\Omega = \text{normalized frequency.} \tag{B.5}$$

Fig. B.1 shows the absorptive bandstop filter with normalized coupling coefficients between each node, and the coupling matrix can be represented as Eq. (B.6). For implementation using symmetrical coupling structures and identical resonators, Eq. (B.7) is used, and the coupling matrix is redefined as Eq. (B.8).

$$\begin{bmatrix} 0 & M_{01} & 0 & M_{03} \\ M_{01} & -jM_{11} & M_{12} & 0 \\ 0 & M_{12} & -jM_{22} & M_{23} \\ M_{03} & 0 & M_{23} & 0 \end{bmatrix} \tag{B.6}$$

$$\begin{aligned} M_{01} &= M_{23} = \sqrt{2M_{11}} \\ M_{12} &= M_{11} \\ M_{22} &= M_{11} = \frac{f_0}{BW \; Q_u} \end{aligned} \tag{B.7}$$

$$\begin{bmatrix} 0 & M_{01} & 0 & M_{03} \\ M_{01} & -jM_{11} & M_{12} & 0 \\ 0 & M_{12} & -jM_{11} & M_{01} \\ M_{03} & 0 & M_{01} & 0 \end{bmatrix} \tag{B.8}$$
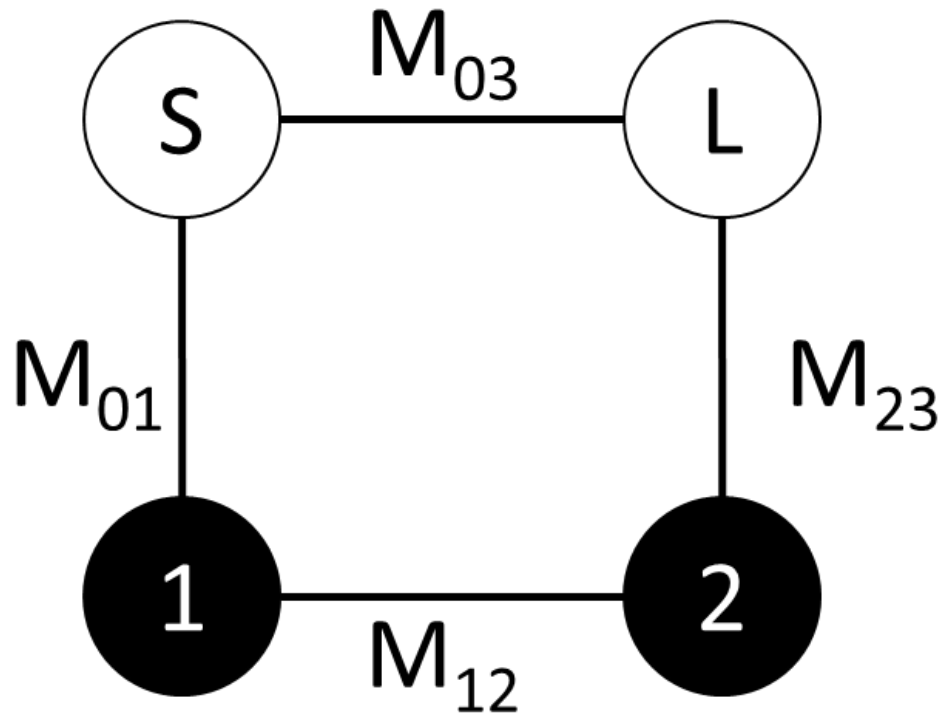
Fig. B.1. A two-pole absorptive bandstop filter topology. S (source) and L (load) denote the input and output ports, and 1 and 2 denotes resonator 1 and resonator 2. Coupling coefficients between each nodes are represented by M_{mn}.

Our first step is find the external coupling for each resonator. This can be done by excluding the second resonator and only use one resonator. The associate coupling matrix becomes

$$
\begin{bmatrix}
0 & M_{01} & 0 & M_{03} \\
M_{01} & -jM_{11} & 0 & 0 \\
0 & 0 & 0 & 0 \\
M_{03} & 0 & 0 & 0
\end{bmatrix}.
\tag{B.9}
$$

The acquired using transfer function using Eq. (B.9) is

$$S_{21}(S) = \frac{2\left(M_{03}M_{11}S + jM_{03}S^2\right)}{3jM_{11}S + jM_{03}^2M_{11}S - S^2 - M_{03}^2S^2}. \tag{B.10}$$

S_{21} in Eq. (B.10) will have a -6.02 dB dip in the center frequency. Therefore, we can use this criteria as a guideline to tune the external coupling gap between each single resonator to the microstrip line, as shown in Fig. B.2. The next step is decide the internal coupling between the two resonators. This can be done by eliminating the source and load coupling, as shown in Fig. B.3, which will make the associate coupling matrix becomes

$$\begin{bmatrix} 0 & M_{01} & 0 & 0 \\ M_{01} & -jM_{11} & M_{12} & 0 \\ 0 & M_{12} & -jM_{11} & M_{01} \\ 0 & 0 & M_{01} & 0 \end{bmatrix}, \tag{B.11}$$

and the transfer function is

$$S_{21}(S) = \frac{4jM_{11}^2}{10M_{11}^2 + 6jM_{11}S - S^2}. \tag{B.12}$$

The acquired S_{21} using Eq. (B.12) will exhibit a -7.96 dB at the center frequency. Finally, the last step in our implementation procedure is decide the transmission line length between source and load such that the insertion phase of the source-load coupling is 180 degrees out of phase with respect to the insertion phase in the previous step, which in our case is 5.8 mm, and the final design is shown in Fig. B.4.
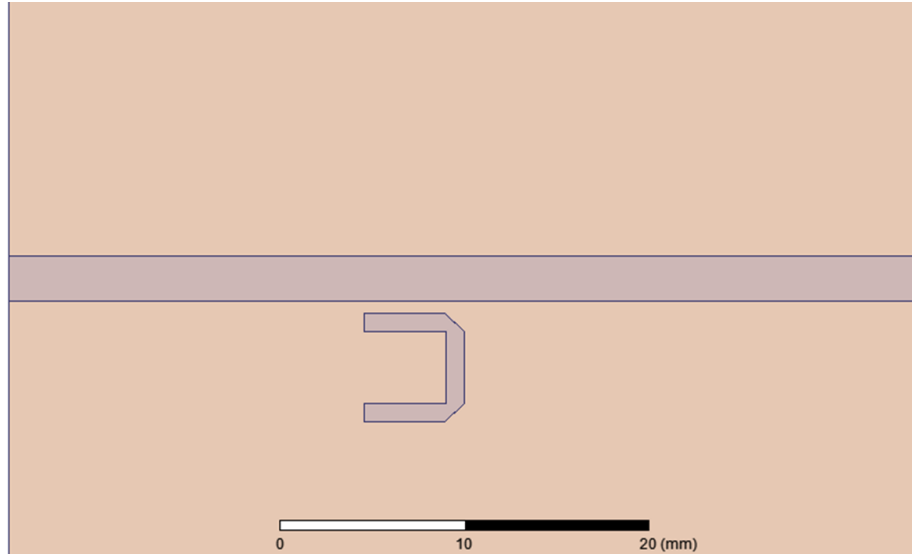
Fig. B.2. Simulation setup in HFSS for external coupling tuning. The goal in this step is to tune the external coupling between the microstrip line and the resonator until we meet the -6.02 dB criteria in S_{21} at the center frequency.
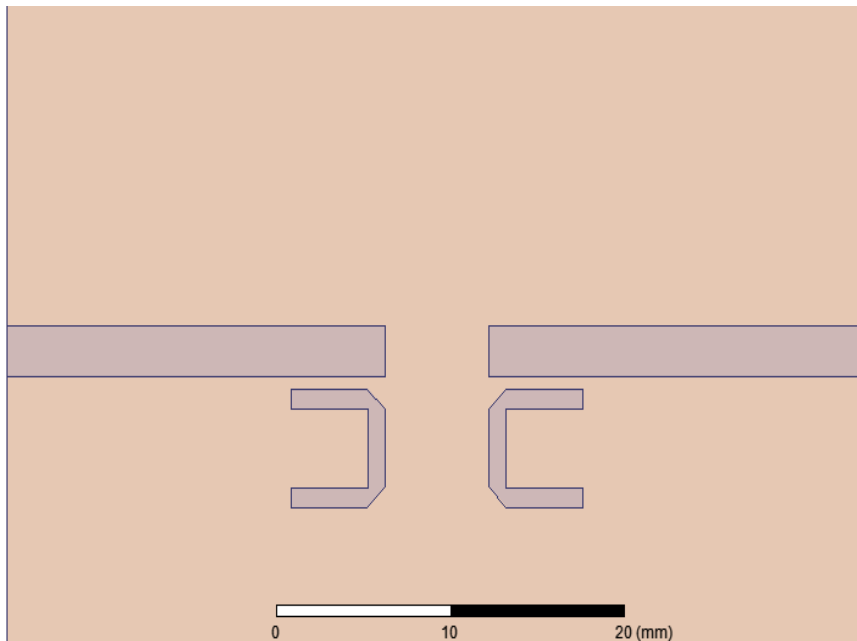

Fig. B.3. Simulation setup in HFSS for internal coupling tuning. The goal in this step is to tune the external coupling between the microstrip line and the resonator until we meet the -7.96 dB criteria in S_{21} at the center frequency.
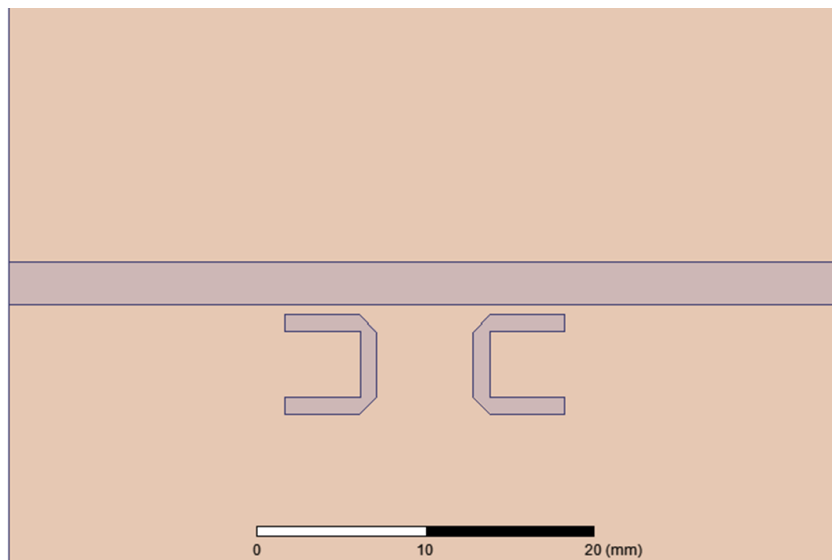
Fig. B.4. Simulation setup in HFSS for direct coupling between input and output nodes. In this step, a 90 degrees transmission line is added between the input and output nodes.

VITA

VITA

Yu-Ting Huang was born in Taoyuan, Taiwan in 1981. He received the B.S. and M.E. degrees in electrophysics from National Chiao Tung University, Hsinchu, Taiwan in 2003 and 2005, respectively. He is currently pursuing his Ph.D. degree in electrical and computer engineering at Purdue University in the IDEAS Lab. His research interests include microwave spectroscopy and microwave filter theory and synthesis. He is a treasurer of Purdue University's MTT-S Student Chapter. His paper was a finalist in the 2012 IEEE MTT-S IMS Student Paper Competition.